Wideband Compact Antenna Design and Validation for Communication and Sensing Applications

Master's Thesis submitted to

Department of Microwave Electronics

Faculty of Electrical Engineering and Computer Science

University of Kassel, Germany

In partial fulfillment of the requirements for the degree of

MASTER OF SCIENCE IN ELECTRICAL COMMUNICATION ENGINEERING

Thesis work carried out at

Barkhausen Institut

Dresden, Saxony

Author

Mohammad Rabiul Hossen

Matriculation No. 35183813

First Examiner	Prof. Dr.-Ing. Axel Bangert
Second Examiner	Prof. Dr. sc. techn. Dirk Dahlhaus
Supervisor	Dr. Padmanava Sen (Barkhausen Institut)

August 2022

Author's Declaration of Originality

To the best of my knowledge, I do hereby declare that this master thesis work report is my own work. It has not been submitted in any form to any other university or other institution of education. Information derived from the published or unpublished work of others has been acknowledged in the text, and a list of references is given.

Student's signature
Mohammad Rabiul Hossen

Kassel, 31.08.2022

Acknowledgments

First and foremost, I would like to express my sincere gratitude to Prof. Dr.-Ing Axel Bangert and Prof. Dr. sc. techn. Dirk Dahlhaus for agreeing to be my supervisor and encouraging me to complete this thesis work. Completing this undertaking would have not been possible without their meaningful support. I am eternally grateful to Dr. Padmanava Sen for giving me the opportunity to undertake this attractive project at Barkhausen Institut and for his continuous support with his team of RF Design Enablement. My sincere gratitude to Mehrab Ramzan for his guidance and support throughout the project and to Merve Tascioglu for insightful discussions. I would like to thank my beloved parents and my wife for their encouragement and loving support for this work and in my daily life. Finally, my brothers-in-law who motivated me since my school life for higher education in abroad and helped me to achieve my goal.

Abstract

Wideband antenna design for communication and sensing applications is becoming an important research area for the advancement of 5G and IoT applications as well as for future 6G research. These two application segments may be seen together as future technology (e.g. IEEE 802.11bf Wi-Fi sensing, UWB localization/identification, joint communication and sensing in 6G networks) with increasing demand of bandwidth to enable different applications. In addition to that, space constraints in battery-driven mobile devices also needs to be addressed as most of the handheld devices becoming slimmer. Wideband antenna can certainly reduce the number of antennas needed for such devices. To achieve larger fractional bandwidth and compactness of the wideband antennas, the challenges include the performance parameter trade-offs such as impedance matching bandwidth, stable gain over the frequency span and omnidirectional radiation pattern (when needed). This thesis project aims to design, fabricate and measure compact planar wideband antennas for UWB applications and Wi-Fi sensing applications (5.9-7.1 GHz targeting IEEE 802.11bf). A narrowband patch antenna is taken as a reference, and steps are shown to design a UWB antenna from the same narrowband antenna dimension using defected ground structure method. For the WB antenna (5.9-7.1 GHz), the experience from the UWB design and the slot-loading technique is used to develop a 0.3 λ_0 compact design. Furthermore, the UWB antenna is used to validate the thesis work. An equivalent circuit model is designed for the UWB antenna. Additionally, communication and range measurements are performed to show the application scenarios of the developed UWB antenna.

List of Abbreviations and Terms

IoT	Internet of Things
PAN	Personal Area Network
WUSB	Wireless USB
FCC	Federal Communication Commission
SNR	Signal to Noise Ratio
EIRP	Effective Isotropically Radiated Power
Radar	Radio Detection and Ranging
LoS	Line of Sight
NLoS	Non Line of Sight
AoA	Angle of Arrival
JC&S	Joint communication and sensing
MAC	Media Access Control
CSI	Channel State Information
ML	Machine Learning
DGS	Defected Ground Structure
HFSS	High Frequency Structure Simulator
FEM	Finite Element Method
BW	Bandwidth
UWB	Ultra Wideband
WB	Wideband
Tx	Transmitter
Rx	Receiver
PCB	Print Circuit Board
PNA	Programmable Network Analyzer
AWG	Arbitary Waveform Generator
DAMS	Diamond Automated Measurement System
EVM	Error Vector Magnitude
rms	root mean square
QPSK	Quadrature Phase-Shift keying
QAM	Quadrature Amplitude Modulation
LNA	Low Noise Amplifier
OTA	Over The Air
PSD	Power Spectral Density

List of Symbols

Q	Quality Factor
λ	Wavelength
c_0	Speed of light in vacuum
Ω	Ohm
ε	Permittivity of a dielectric medium
μ	Permeability of a material
Z_0	Characteristic Impedance
Z_i	Input Impedance
R	Resistance
L	Inductance
C	Capacitance
ϵ_{eff}	Effective Dielectric Constant
ϵ_r	Dielectric Constant
f_r	Resonance Frequency
ΔL	Extension of Length
SubW	Width of the substrate
Wp	Width of the Patch antenna
SubL	Length of the substrate
Lp	Length of the Patch antenna
h	Height of the substrate
Lf_50	Feed Length
Wf_50	Feed Width
QW	Quarter Wave
Lf_qw	QW Feed Length
Wf_qw	QW Feed Width
Rg	Finite Ground Length
S1_L	Bottom Slot Length
S1_W	Bottom Slot Width
S2,3_L	Top Slot Length
S2,3_W	Top Slot Width
S4_L	Middle Slot Length
S4_W	Middle Slot Width

Table of Contents

List of Figures

List of Tables

1. Introduction

1.1 Motivation and Objectives

The concept of bandwidth is closely related to the system's ability to send information. In order to transmit data, the signal must change in some way, and the rate at which these changes occur affects the rate at which information can be transmitted. The signal can change faster if the signal has a wide bandwidth (contains higher frequencies or is compatible). Therefore, the wider the signal bandwidth, the higher the maximum data transfer rate. However, there is a limit to keep increasing the signal bandwidth infinitely due to the channel bandwidth, noise characteristics and receiver capability. According to Shannon's channel capacity for the noisy channel [1].

$$C = B * log_2(1 + S/N)[bits/s] \tag{1.1}$$

Where C is channel capacity in bits/second, B is the channel's bandwidth in Hertz and S/N is the Signal to Noise ratio (SNR). According to the equation, the only way to increase the channel capacity is to either increase the bandwidth or increase the SNR.

On the other hand, large bandwidth also significantly improves radar range resolution to get more targets more accurately and map complex environments [2].

$$d_{res} = c/2B \tag{1.2}$$

Therefore, the fast growth in wireless communication systems created enormous demands for wideband antennas to satisfy high data rates and range resolution. The term wideband applies to any signal, technology or system where the BW is over 500 MHz or the fractional BW exceeds 20%. Fractional BW of greater than 50% is referred to as ultra-wideband (UWB). In 2002, FCC approved the UWB technology in the frequency range of 3.1–10.6 GHz with a maximum radiated power of -41.3 dBm/MHz and data rate between 110–200 Mbps within a 10 m distance [3]. There are many fundamentally different applications such as data communication, localization and identification, and radar and sensing that use wideband antennas and customized antennas are needed depending on the desired radiation characteristics and BW.

Due to the vast BW in UWB communications, these antennas used in the mobile handheld devices in Personal Area Network (PAN) communications preferably have omnidirectional patterns with compact size and planar designs [4, 5]. Wireless USB (WUSB) is one popular commercial application designed to achieve 480 Mbit/s at distances up to 3 m and 110

Mbit/s at up to 10 m [6]. Antennas working in the UWB frequency range share the same spectrum with several other narrowband wireless systems, primarily in the UWB band of 3.1–10.6 GHz. These narrowband systems such as 3.6 GHz IEEE 802.11y wireless local area networks (3.6575–3.69 GHz), 4.9 GHz public safety WLAN (4.94–4.99 GHz), and 5 GHz IEEE 802.11a/h/j/n WLAN (5.15–5.35, 5.25–5.35, 5.47–5.725, 5.725–5.825 GHz) can create strong interference to the UWB systems [7]. To avoid interference and to improve the associated SNR, UWB antennas are sometimes designed with band notches that effectively filter out the unwanted signals at the frequencies used from a narrowband system. On the other hand, UWB signals are considered white noise for narrowband systems. However, the FCC mask limits the UWB effective isotropically radiated power (EIRP) to -41.3 dBm/MHz for 3.1–10.6 GHz. Therefore, UWB signals are relatively low in radiated power to significantly degrade the performance of the narrowband systems. Hence, they also have short range. In addition, UWB antennas eliminate the need for multi-narrow band antennas, as a single UWB antenna can meet different frequencies and operating bands, reducing multi-antenna interference and saving spaces in the device.

On the other hand, sensing here refers to retrieving information from the received radio signals other than the communication data modulated to the signal at the transmitter. Due to the large fractional BW of UWB antennas, there are many sensing applications such as short-range UWB Radar [8], cognitive radio spectrum sensing [9, 10] and microwave imaging [11, 12] etc. With the increasing BW, the range resolution becomes better. The sensing parameters for the measurement related to location and moving speed are time delay, angle-of-arrival (AoA), angle-of-departure (AoD), Doppler frequency and physical feature parameters of the objects or activities.

However, with the rapid growth of the wireless communication industry, consumer devices and services, the frequency spectrum is becoming increasingly congested. New technologies like Wi-Fi sensing, Joint communication and sensing in 6G networks are emerging as an attractive solution for integrating two individually deployed systems (communication and sensing) into one system to tackle the BW scarcity and reduce the use of different devices for individual communication and sensing applications [13]. As an example, UWB impulse radio system (IEEE802.15.4z), as shown in figure 1.1 can be considered for joint communication and sensing (JC&S) applications. Mobile companies, automotive and semiconductor manufacturers have come together under the Car Connectivity Consortium umbrella, to standardise this UWB impulse radio system for distance measurement as a vehicle access system within the Digital Key 3.0 specification [14].

In UWB impulse radio system (IEEE802.15.4z), a sequence of pulses is used for the data transmission of IEEE 802.15.4z. Various configuration options in the MAC layer enable repeated distance measurement of several other devices at a fixed repetition frequency. During the distance measurement, check and control signals are transmitted in data pack-

Figure 1.1. NXP Trimension™ - Use of UWB radio technology as a distance and direction sensor in a smartphone, a vehicle and the Internet of Things. [15]

ages [17]. Therefore, UWB is already introducing data transfer, distance measurement, 3D incident angle measurement with two or more parallel receivers and presence detection over short distances. The goal now is to turn this joint communication and sensing into a foundation block of the new 6G standard [17].

Another technology, IEEE 802.11bf (Wi-Fi sensing), will be finalized and introduced as an IEEE standard in September 2024, making Wi-Fi cease to be a communication-only standard and legitimately become a full-fledged sensing paradigm [18]. The presence of Wi-Fi devices in public and private spaces will continuously map the surrounding environment using Wi-Fi signals as sounding waveforms and open the door for wireless sensings such as detecting the human presence activity recognition and object tracking. The idea behind

(a)   (b)
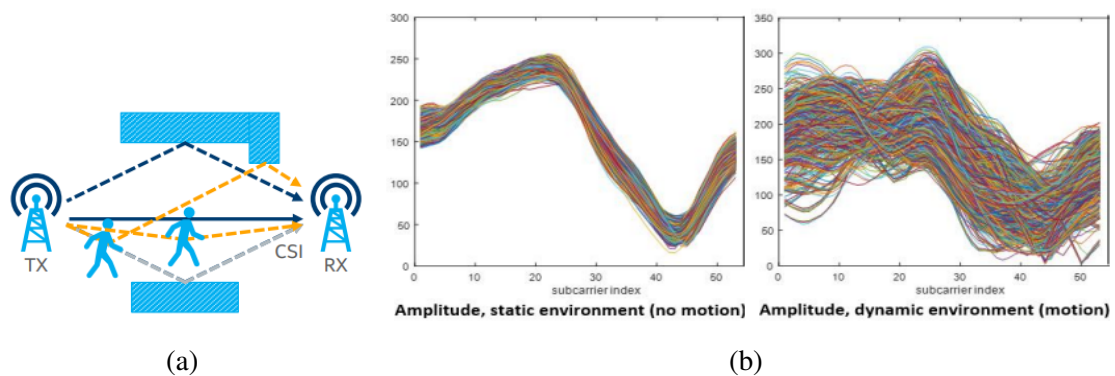
Figure 1.2. (a) Wi-Fi sensing scenario (b) CSI amplitude variation for static and dynamic motion.[16]

3

Wi-Fi sensing is to exploit the Channel State Information (CSI) to measure the changes in the amplitude or phase. CSI varies as the changes in the environment alter the paths. Figure 1.2 shows the Wi-Fi sensing scenario and CSI amplitude variation of different environments. Using ML/digital signal processing algorithm on CSI measurement data, human activity recognition and object tracking will be possible. The wideband compact antenna in the frequency range 5.9-7.1 GHz targeting IEEE 802.11bf (Wi-Fi sensing) applications can undoubtedly meet the initial requirements for developing such a system. Therefore, the goal of this thesis is to design wideband antennas targeting UWB and IEEE 802.11 bf (5.9-7.1 GHz) applications considering the below parameters-

- Wide bandwidth
- Compactness

1.2   Organization of the Thesis

The thesis consists of five chapters. The chapters cover the literature review, theory, design procedure, experimental investigation and numeric results.

Chapter 1 contains a brief literature review of the importance of the wideband antenna design for communication and sensing applications and the organization details of the whole thesis.

Chapter 2 contains the antenna key parameters, theoretical background of narrowband microstrip patch antenna and techniques to increase the bandwidth.

Chapter 3 provides the step-wise design procedures of the proposed antennas.

Chapter 4 contains the experimental results of the fabricated antennas along with a description of the experimental setup. Comparison of the measured and simulated results are also provided in this section.

Chapter 5 contains a brief summary of the completed work.

2. Theoretical Analysis

2.1 Narrowband Microstrip Patch Antenna

Microstrip antennas became popular in the 1970s primarily for space-borne applications [19]. Today, they are used for many government and commercial applications. These antennas have a metallic patch on top of a grounded substrate. Here, the permittivity of the dielectric layer (should be kept between 2.2 and 12) and the substrate thickness (should not be smaller than 1/40th and larger than 1/20th wavelength of operation) are critical parameters for the performance of the antenna [19]. A standing wave is generated by the complex impedance structure of the antenna when a current flow energizes the conductive structure, creating an electric field from the edge of the antenna. The electric field becomes a propagating electromagnetic wave. In this way, the core functionality of an antenna is achieved. The metallic patch of the antenna can take many different configurations. However, the rectangular and circular patches are the most popular because of their ease of analysis, fabrication and attractive radiation characteristics. Various shapes of the metallic patch of antennas are illustrated in the figure 2.1 [19].

Square   Rectangular   Dipole   Circular

Triangular   Eliptical   Circular ring
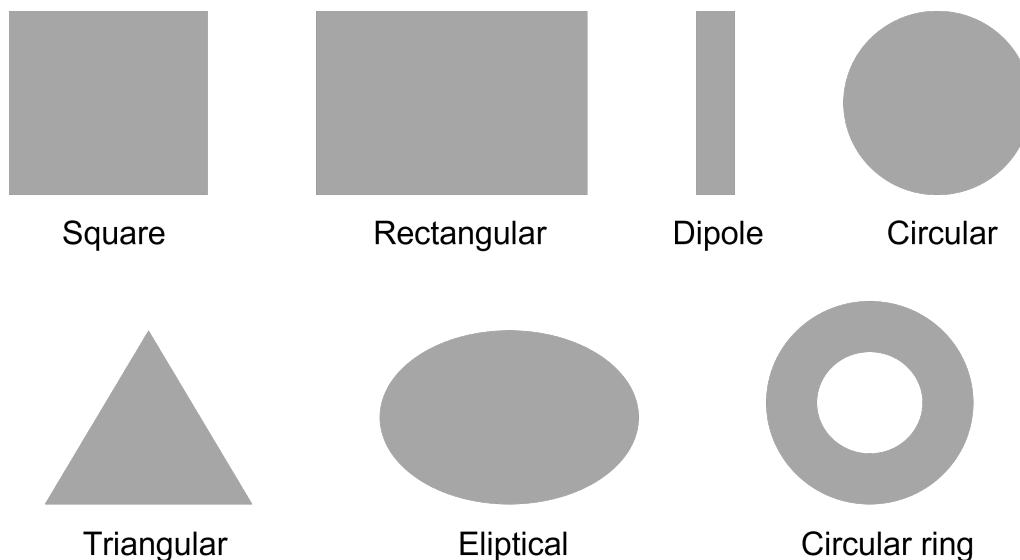
Figure 2.1. Different shapes of patch.

The microstrip antennas are low-profile, comfortable on planar and non-planar surfaces, inexpensive and easy to fabricate using modern printed circuit technology, mechanically robust when mounted on rigid surfaces, compatible with MMIC designs, and versatile in resonant frequency and polarization pattern [19]. Due to their robustness and planar

Advantages	Disadvantages
Low weight and volume due to thin profile.	Narrow bandwidth.
Low cost of fabrication and easy integration.	Low efficiency due to dielectric and conductor loss.
Multiple frequency operations.	Spurious radiation and lower gain due to excitation of surface waves.
Linear and circular polarizations.	Temperature and humidity sensitive.

Table 2.1. Advantages and disadvantages of the narrowband microstrip patch antennas.

structure, these antennas can be mounted on the surface of aircraft, spacecraft, satellites, missiles, cars and even handheld mobile telephones. However, some significant disadvantages are their low efficiency, high Q, poor polarization purity, poor scan performance, spurious feed radiation, and very narrow frequency bandwidth, typically only a fraction of a percent or a few percent as provided in table 2.1 [20].

2.1.1   Mathematical Modeling of Rectangular MPA: Transmission Line Model

The most popular methods of analysis for microstrip patch antennas are the transmission-line [21], cavity [22] and full-wave [23] (which include integral equations, Moment of Method). The transmission-line model is the simplest of all, which gives good physical insight but is less accurate, including an inability to account for radiating edge field variance. In fact, it is only suitable for rectangular patch antennas [24]. Rectangular patch antennas are very easy to analyze by using both the transmission line and cavity models. Here, only transmission line model is discussed. According to the transmission line model, a rectangular microstrip patch antenna is characterized by two simple slots, each with width W and height h, separated by a transmission line length L and a low impedance Z_c [19, 25]. At the edges of the patch, EM fields undergo fringing due to the finite length and width of the patch, as shown in figure 2.2. The amount of fringing depends on the patch's dimensions and the substrate's height. For the E-plane (XY plane), the dielectric constant ϵ_r of the substrate and the ratio of the patch length to the substrate's height (L/h) is the function of fringing. The fringing field is reduced since the microstrip antennas are mostly L/h » 1. However, it must be considered as it influences the antenna's resonant frequency. The effective dielectric constant of the patch substrate is reduced as Eq. 2.1 due to fringing fields. The effective dielectric constant is essentially constant for low frequencies. At higher frequencies, its value increases monotonically and eventually approaches the values
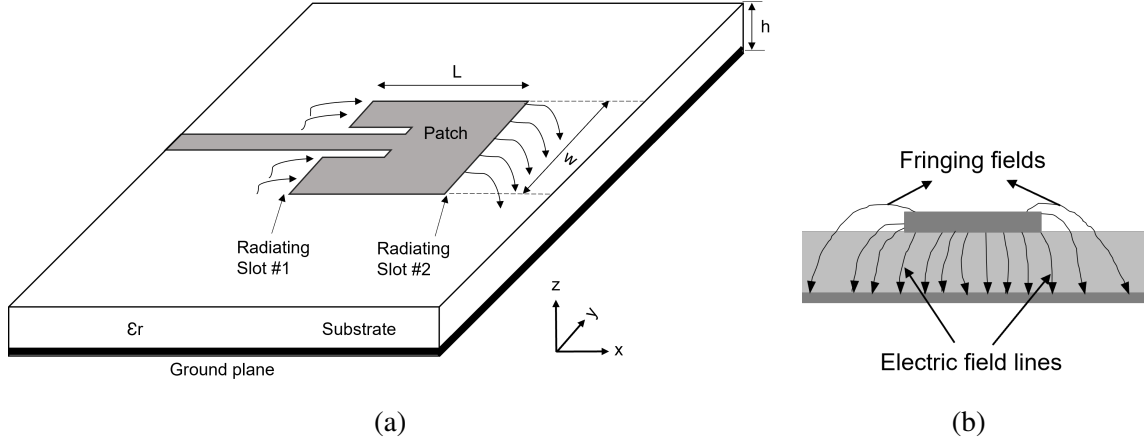
Figure 2.2. (a) Transmission line model of the microstrip patch antenna (b) E field properties. [19]

of the dielectric constant of the substrate described in Eq. 2.1 [19].

$$\epsilon_{eff} = \frac{(\epsilon_r + 1)}{2} + \frac{(\epsilon_r - 1)}{2} + [1 + 12\frac{h}{W}]^{\frac{-1}{2}}, when \frac{W_f}{h} > 1 \qquad (2.1)$$

The fringing fields makes the patch length looks electrically larger than its real physical length. A very popular and approximate relation for the normalized extension of the length is given by Eq. 2.2 [19].

$$\frac{\Delta L}{h} = 0.412 \frac{((\epsilon_{eff} + 0.3)(\frac{W}{h} + 0.264))}{((\epsilon_{eff} - 0.258)(\frac{W}{h} + 0.8))} \qquad (2.2)$$

Since the length of the patch has been extended by ΔL on each side, the effective length of the patch becomes as Eq. 2.3 [19].

$$L_{eff} = L + 2\Delta L \qquad (2.3)$$

For designing a rectangular microstrip patch antenna, we need to specify the dielectric constant (ϵ_r), resonant frequency (f_r) and thickness of the substrate (h). After that, we need to determine the width (W) and length (L) of the patch by Eq. 2.4 and 2.5 [19].

$$W = \frac{1}{(2f_r\sqrt{(\mu_0\epsilon_0)}}\sqrt{\frac{2}{(\epsilon_r + 1)}} \qquad (2.4)$$

$$L = \frac{1}{2f_r\sqrt{(\mu_0\epsilon_0)}\sqrt{\epsilon_{eff}}} - 2\Delta L \qquad (2.5)$$

7

ϵ_{eff} and ΔL are calculated from Eq. 2.1 and 2.2. Then, the resonance frequency of the patch antenna for the mode TM_{mn} is calculated as [26]

$$f_r = \frac{1}{2 f_r \sqrt{(\mu_0 \epsilon_0)}} [(\frac{m}{L})^2 + (\frac{n}{W})^2]^{\frac{1}{2}}$$ (2.6)

Where, m, n: operating modes along with the L and W

2.1.2 Feeding Method

The feed technique is an important parameter that significantly affects antenna characteristics such as VSWR, Bandwidth, and return loss. The four most popular feeding techniques are the microstrip line, coaxial probe, aperture coupling, and proximity coupling [27]. Microstrip line and coaxial probe are popular techniques for feeding the patch antenna. The energy is fed directly to the radiating patch via the connecting line in the microstrip line and coaxial probe. In contrast, proximity coupling and aperture coupling are used to transfer power between the connecting part and the radiating patch. Below, the microstrip line feeding technique is discussed in detail as it is used in this thesis work.

Microstrip Line Feed:

The microstrip feed line is a conducting strip, usually of a much smaller width than the patch. It is easy to fabricate, simple to match by controlling the position, and easy to model. However, surface waves and spurious feed radiation increase as the substrate thickness increases, limiting the bandwidth for practical designs (typically 2–5%). Direct connection to the patch's edge and inset cutting are two fundamental methods for implementing this method. This type of feed provides a planar structure since the feed is etched on the same substrate material. An additional quarter wavelength transformer is needed for the edge feeding impedance matching of the narrowband patch antenna. In contrast, in inset feeding, making the inset depth closer to the middle of the patch matches the impedance. The width of the microstrip line, which is associated with the characteristic impedance, can be calculated via the Eq. 2.7 and 2.8 [28]

$$Z_0 = \frac{60}{\sqrt{\epsilon_{eff}}} \ln[\frac{8h}{W_f} + \frac{W_f}{4h}][\Omega], when \frac{W_f}{h} \leq 1$$ (2.7)

$$Z_0 = \frac{120\pi}{\sqrt{\epsilon_{eff}}[\frac{W_f}{h} + 1.393 + 0.667 \ln (\frac{W_f}{h} + 1.444)]}[\Omega], when \frac{W_f}{h} > 1$$ (2.8)

where W_f is the width of the microstrip line. Equation 2.9 gives the calculation of the feed length [26]

$$L_f = \frac{\frac{\lambda_0}{\sqrt{\epsilon_r}}}{4}$$ (2.9)
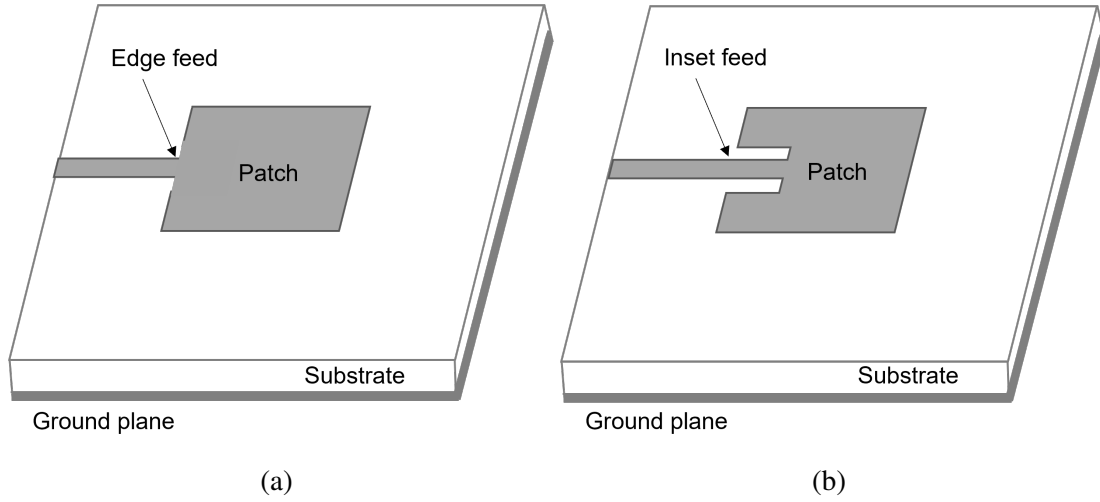
Figure 2.3. Microstrip line feeding (a) Edge feeding (b) Inset feeding.[19]

2.2   Wideband Microstrip Patch Antenna

As mentioned in the previous section, the most severe limitation of the MPA is its narrow bandwidth. The bandwidth can be defined in terms of its VSWR or input impedance variation with frequency. The VSWR or impedance BW of the MPA is the frequency range over which it is matched with that of the feed line within specified limits [20]. The BW of the MPA is inversely proportional to its quality factor, where the Q factor is defined as the ratio of energy stored to the power radiated. However, there is no complete freedom to achieve optimum antenna performance as the BW, Q factor and efficiency are interrelated. Degrading the Q factor increases the BW but lowers the radiation efficiency. Therefore, there is always a trade-off between them. The relation between BW with respect to the Q factor and VSWR is given below. [19].

$$BW = \frac{VSWR - 1}{Q\sqrt{VSWR}}$$ (2.10)

where VSWR is defined in terms of the input reflection coefficient Γ as:

$$VSWR = \frac{1 + |\Gamma|}{1 - |\Gamma|}$$ (2.11)

The Γ is a measure of reflected signal at the feeding point of the antenna where it is defined in terms of input impedance Z_{in} of the antenna and the characteristic impedance Z_0 of the feed line as given below [20]:

$$\Gamma = \frac{Z_{in} - Z_0}{Z_{in} + Z_0}$$ (2.12)

The BW is usually specified as the frequency range over which VSWR is less than 2 (corresponds to a return loss of 10 dB). The expression for approximately calculating

9

the percentage BW of the rectangular MPA in terms of patch dimensions and substrate parameters is given by [20]

$$BW = \frac{\epsilon_r - 1}{\epsilon_r^2} \frac{W}{L} h \tag{2.13}$$

where W and L are the width and length of the rectangular MPA. With an increase in W, BW increases. However, W should be less than the resonant wavelength to avoid the excitation of higher-order modes. Additionally, by changing the substrate parameters, such as decreasing the dielectric constant or increasing the substrate height, the stored energy decreases and the radiated power increases. Hence the Q factor decreases and BW increases. But, the disadvantage of using thick substrate is the increased surface wave power resulting in poor radiation efficiency [29]. In addition, other techniques enhance the BW of a narrowband MPA, which are discussed in detail below.

2.2.1 Planar Multi Resonator Configurations

Placing multiple resonators side by side with a small gap between them with different combinations widened the BW, similar to the case of multistage tuned circuits. Using this method, BW of 5–25% are possible to achieve [30, 31, 32]. Various patches like narrow strips, shorted QW rectangular patches, and rectangular resonator patches have been coupled with a gap to the main fed rectangular patch. In this method, the main patch is excited by the feed, and parasitic patches get excited by the coupling effect. If the resonant frequencies from the patches are close to each other, then the wide BW is achieved. The overall impedance BW will be the superposition of the response of the resonators resulting in wide BW. Three different combinations of gap-coupled rectangular patches are shown in figure 2.4 These planar multi resonator arrangements yield broad BW. Still, they have the disadvantages of large size for array configuration and variation in the radiation pattern over the impedance BW [20]

2.2.2 Multilayer Configurations

In the multilayer method, different dielectric substrate layers are stacked on each other and patches are placed on top of each dielectric layer. These arrangements are categorized as electromagnetically coupled or aperture-coupled MPAs based on the coupling mechanism. Here, electromagnetically coupled structure is discussed.

Electromagnetically Coupled MPAs:
In the electromagnetically coupled MPA, the bottom or top dielectric layer patch is fed by a coaxial probe, and the other patches on the different dielectric layers are electromagneti-
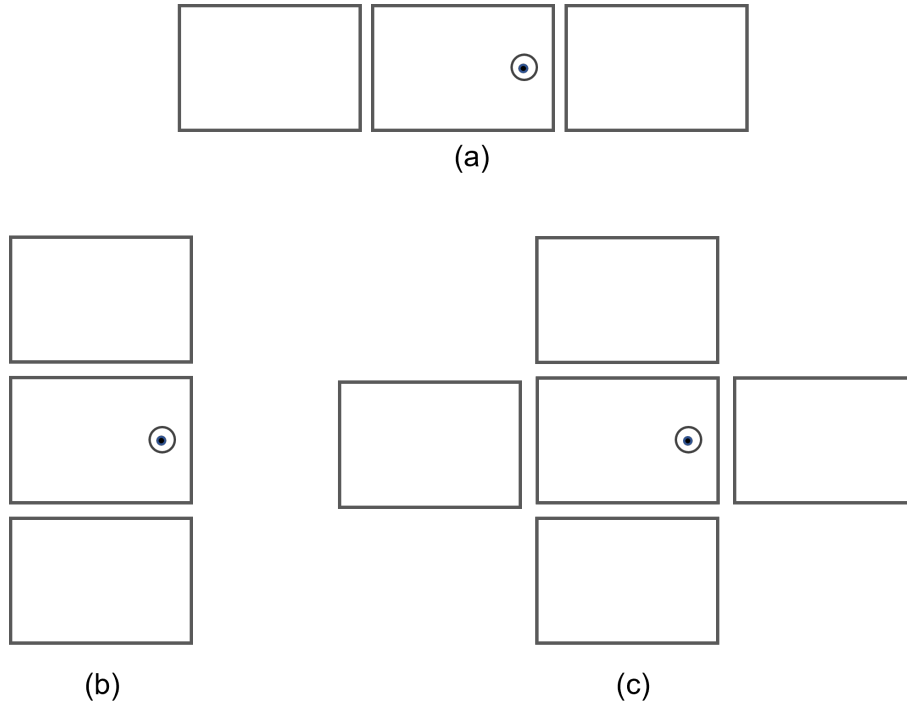
Figure 2.4. Various gap-coupled multi resonator RMPA configurations: (a) three RMPAs gap-coupled along radiating edges, (b) three RMPAs gap-coupled along non-radiating edges, and (c) five gap-coupled RMPAs[20].

cally coupled. The patches can be fabricated on various substrates. The patch dimensions, which are fabricated on different substrates, are optimized based on the respective dielectric parameter value so that the resonance frequencies of the patches are close to each other to yield broad BW [20]. The techniques mentioned above improve the BW, but the
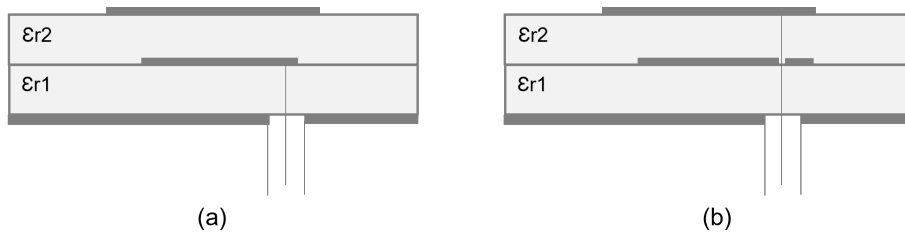
Figure 2.5. An electromagnetically coupled MSA, in which (a) the bottom patch is fed and (b) the top patch is fed [20].

improvement is insignificant. Also, these techniques are not compact, which is one of the goals of this thesis. In the below sections, the compact wideband methods are discussed.

2.2.3   Shorted Patch Technique

Introducing shorting pins (from the patch to the ground plane) at various locations can reduce the patch antenna size by 50% [33]. These positions depend on the resonant modes.

11

In this case, the introduction of shorting walls or pins does not load the antenna. In another situation, pins can be located at positions where higher-order modes (0, n), n = 2, 4, 6... are present to suppress these modes' excitation. For a QW patch shorted at the far end, the current at the end of the patch is not zero anymore. As a result, this QW patch antenna has the same current-voltage distribution as a half-wave patch antenna. However, the fringing fields responsible for radiation are shorted on the far end, so only the fields nearest the transmission line radiate [34]. Consequently, the antenna gain is reduced. This type of antenna is known as Planar Inverted F Antenna (PIFA). The feed is connected between the open and shorted end, and the distance between the feed to the shorting pin (L_b) controls the input impedance. The impedance will decrease by placing the feed closer to the shorting pin. The top plate of the PIFA is at a height h from the ground plane. The PIFA sits on top of a dielectric with permittivity as the patch antenna. However, a conventional PIFA has an
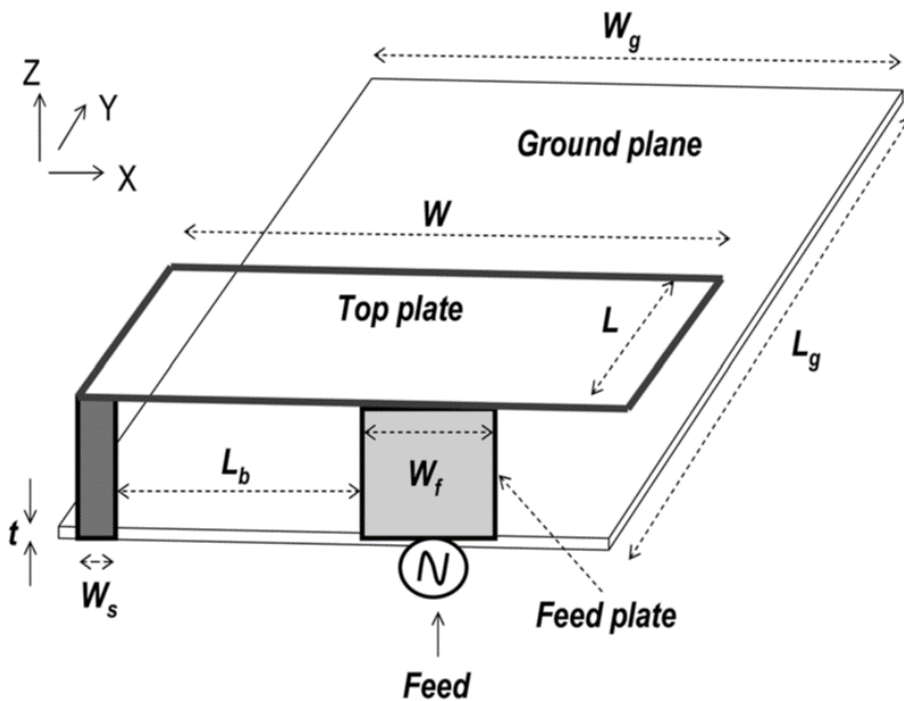
Figure 2.6. UWB Planar Inverted F Antenna (PIFA)[35].

inherent narrowband that must be enhanced to fulfil the wideband requirements.

Techniques to increase the BW of PIFA:

- Thick air substrate lowers the Q and increases the bandwidth of the PIFA.
- Using parasitic patches with resonant lengths close to the primary resonant frequency.
- Adjust the location and the spacing between two shorting posts.
- Changes in the widths of feed plate and shorting plate [35].
- Using Stacked elements will increase the bandwidth [36].
- Reducing the ground plane by inserting several slots at the ground plane edges can effectively broaden the antenna bandwidth. This way antenna structure's quality

12

factor is minimised and increases the bandwidth [37].

By following the above techniques, the BW of the PIFA can be increased to UWB. But, this type of antenna has air between the substrate and ground, making it challenging to fabricate.

2.2.4 Slotted Ground Plane Technique

When the proper slots are inserted in the microstrip antenna's ground plane, the antenna's fundamental resonant frequency can be lowered [38]. Also, increased impedance band-width can be obtained by increasing the length of the inserted slots. A pair of narrow slots
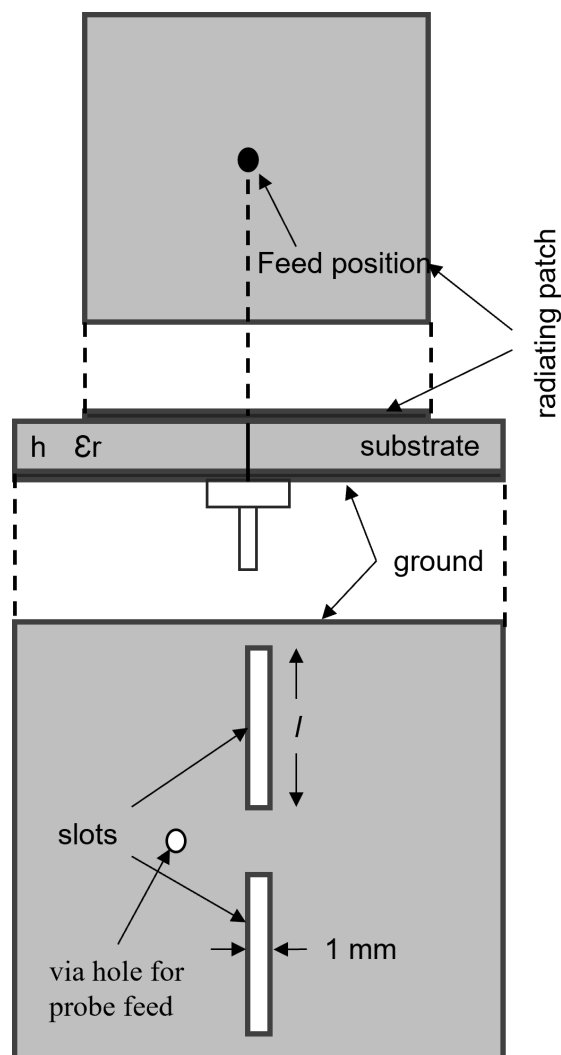
Figure 2.7. Geometry of a compact microstrip antenna with a slotted ground plane[35].

(Length l width 1 mm) is inserted in a finite ground plane in design [38]. Two narrow slots are positioned along the centerline of the ground plane perpendicular to the antenna's resonant direction to effectively meander the excited surface current paths in the ground

13

plane. Size reduction about 39% is achieved using this technique compared to the regular microstrip antenna. The impedance bandwidth (BW) for the case with l = 20 mm is 3.1%, more significant than that (2.7%) of the corresponding regular microstrip antenna. This behaviour is mainly due to the inserted slots in the ground plane, which effectively lower the quality factor of the microstrip antenna. This technique is used for designing the UWB antenna in this thesis.

2.2.5 Slot-Loading Technique

In this method, suitable slots are cut on the radiating patch, which changes the current distribution in the patch [20]. Depending on the slot position and size, the current takes a longer path than the patch without a slot. This way, antenna size can be reduced with the enhanced bandwidth. The current distribution has to be analysed first to find the suitable position for the slots to be placed. The slot must be placed in a position that affects the current distribution most to force the current to take the longer path. The disadvantage of cutting a slot in the radiating patch is the reduced gain. This thesis uses this technique to design the wideband antenna for IEEE 802.11 bf.

2.3 Antenna Key Parameters

Reflection Coefficient: The reflection coefficient is an electrical parameter representing the amount of a wave reflected back due to the impedance mismatch in a transmission line. It is the complex amplitude ratio of the reflected voltage wave to the incident voltage wave, and the symbol of this coefficient is Γ, mathmatically [39].

$$\Gamma(l) = \frac{V_0^-}{V_0^+} = \frac{Z_L - Z_0}{Z_L + Z_0} e^{-2\gamma l} \tag{2.14}$$

where Γ: Reflection Coefficient, V_0^-: Amplitude of the reflected voltage wave, V_0^+: Amplitude of the incident voltage wave, Z_L: Load impedance, Z_0: Characteristic impedance, γ: Propagation coefficient, l: Transmission line length. For an ideal system there is no impedance mismatch between the transmission line and load. Thus, the reflection coefficient will be 0 in that case.

Return Loss: Return loss is the ratio of incident power to reflected power. It is always positive, and the higher the return loss, the better the antenna's characteristic since it indicates the difference between forward radiated power and backward reflected power [39]. Moreover, the scattering parameter S_{11}, which is used to measure the high-frequency

component behaviour, also enables the calculation of the return loss.

$$RL_{dB} = 20 \log |\Gamma| = -20 \log |S_{11}| \quad (2.15)$$

Input Impedance: Input impedance is needed to determine the antenna's feed point. Mathematically, the voltage-to-current ratio at the antenna's input terminal is the way of calculating it [39].

$$Z_A = \frac{V_A}{I_A} = R_A + jX_A \quad (2.16)$$

Where, X_A: the power stored in the near-field region. R_A: represents the real part of input impedance, which is the summation of radiation resistance and loss resistance ($R_A = R_r + R_L$) [40]. The loss resistance is associated with the material properties such as dielectric loss, conductor loss, etc. The location of feed, antenna type and size, and radiated power are critical parameters for the radiation resistance.

Radiation Pattern: The 3D polar plot of radiated fields distribution of the antenna as a function of ϕ (azimuth angle) and θ (elevation angle) in space is called the radiation pattern. The three major types of radiation patterns are omnidirectional, isotropic and directional.
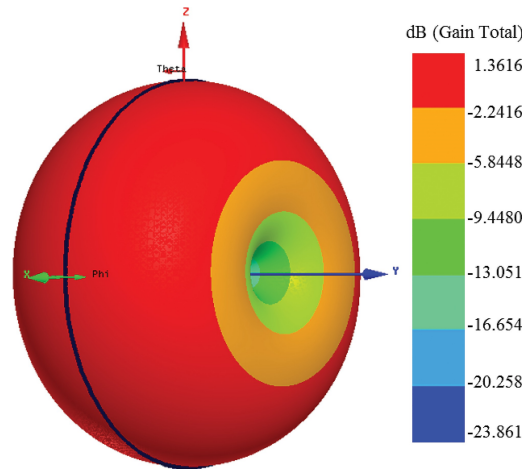
Figure 2.8. 3D far field radiation pattern of the antenna[40].

The omnidirectional pattern is isotropic in a single plane, as shown in figure 2.8 where the maximum radiation exists in the XZ plane. The isotropic pattern is only theoretical because it requires the same radiation in all directions. A directional pattern radiates in a single direction. In addition, the elevation plane (E-plane) and the azimuth plane (H-plane) patterns give the most significant observation about the direction of maximum radiation power. The E-plane is defined as the plane where the electric field E lies, and the H-plane is the plane where the magnetic field H lies [19]. Instead of a 3D pattern, another familiar plot is 2D pattern, which is the slice of the 3D plane. These plots help visualize the direction in which the antenna radiates.

Radiation Intensity: It is a far-field parameter and defined as the power radiated from an antenna per unit solid angle in a given direction. The radiation intensity is calculated mathematically [19],

$$U = r^2 W_{rad} \tag{2.17}$$

where, U: radiation intensity ($W/unit\ solid\ angle$); r: distance; W_{rad}: radiation density (W/m^2)

Directivity: The ability of an antenna to radiate energy in a single desired direction is measured by the term Directivity. It is the ratio of the antenna's radiation intensity $U(\theta, \phi)$ to the radiation intensity averaged over all directions [19].

$$D = \frac{4\pi U(\theta, \phi)}{P_{rad}} \tag{2.18}$$

Antenna Efficiency: An antenna does not transform all electromagnetic energy into radiation because of several losses, such as reflection which causes the dissipation of input power as heat and material losses (i.e. dielectric loss, conductor loss). Therefore, efficiency is necessary for measuring the association of the input and radiated power. It is mathematically the ratio of the power delivered to the antenna input port to the power radiated from the antenna [19].

$$\eta = \frac{P_{rad}}{P_{in}} \tag{2.19}$$

where; η: Efficiency, P_{rad}: radiated power, P_{in}: input power

Gain: Gain (G) is a parameter that considers the efficiency and directivity of an antenna's radiation pattern ($G = \eta D$). It determines how much power the antenna radiates in a specific direction. The other term is known as the absolute gain, which is the ratio of radiation intensity in a given direction to the radiation intensity that would be produced if the accepted input power radiated isotropically [19].

$$G = \frac{U(\theta, \phi)}{P_{in}(accepted\ power)} 4\pi \tag{2.20}$$

where G: Gain, $U(\theta, \phi)$: radiation intensity, P_{in}: accepted input power. Generally, this ratio is expressed in decibels with respect to an isotropic radiator (dBi).

$$G_{dBi} = 10 \log_{10}(G) \tag{2.21}$$

In most cases we deal with the relative gain, which is the ratio of the power gain in a given direction to the power gain of a referenced antenna (lossless isotropic source, e.g. Horn

antenna) in its reference direction [19]. The input power is same for both the antennas.

$$G = \frac{U(\theta, \phi)}{P_{in}(lossless\ isotropic\ source)} 4\pi \qquad (2.22)$$

Bandwidth: The energy radiated or received at a specific frequency interval defines the operating frequency range of the antenna, which is measured by Bandwidth (BW). It is the difference between higher and lower frequencies. The application becomes wideband if the ratio of the upper operating frequency (f_h)to the lower operating frequency (f_l) is equal to or greater than 2 [19].

$$BW = f_h - f_l \qquad (2.23)$$

$\frac{f_h}{f_l} \geq 2$ wideband application

Another term known as fractional BW (FBW), linked to the center frequency mathematically expressed as,

$$FBW(\%) = \frac{f_h - f_l}{f_c} \qquad (2.24)$$

where f_c: Center frequency of the antenna, f_h: Higher frequency of the antenna, f_l: Lower frequency of the antenna range.

In addition to the terms mentioned above, impedance bandwidth which depends on several parameters such as dielectric thickness, size of the ground plane and feed technique, refers to return loss bandwidth [41]. It is frequently measured via return loss plot at -10 dB.

2.4   Equivalent Circuit Model

An antenna can be represented by an equivalent circuit of lumped elements. The equivalent circuit model has both theoretical and practical importance. It provides valuable insights into the design and performance of the antenna. In [42], author uses Foster's canonical forms and SPICE-compatible vector fitting technique and makes a comparison of the antenna equivalent circuits. In [43], degenerated Foster canonical forms for electric and magnetic antenna models are introduced. A non-linear curve-fitting optimization technique is used in [44] for a rectangular microstrip patch antenna to determine the values of the equivalent circuit parameters. This work uses Foster canonical form to model the antenna equivalent circuit as it lacks complexity. In general, an antenna is a linear passive element, and its input impedance can be expressed by Foster's canonical form, assuming no resistance loss, as shown in figure 2.9. Foster first canonical form (figure 2.9a) is suitable for modeling "electric antennas" that operate as open circuits with DC input signals. The second Foster canonical form (figure 2.9b) is used to model a "magnetic antenna" that is electrically shorted to a DC input signal. An example of electrical antennas are dipole and monopole, where loop antennas are magnetic antennas [43]. The input impedance $Z_{in}(\omega)$
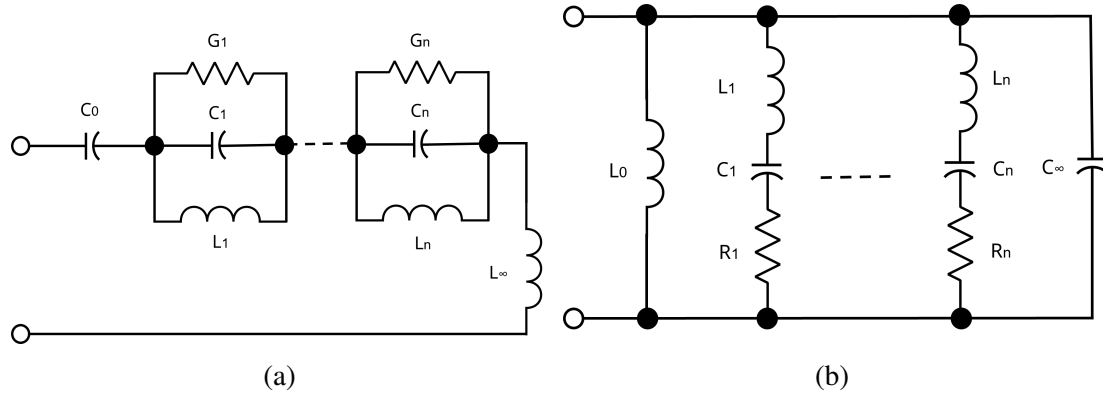
Figure 2.9. Foster canonical forms for (a) electric antennas and (b) magnetic antennas [43]

of the equivalent circuit is calculated using Eq. 2.25 [45]

$$Z_{in}(\omega) \cong j\omega L_0 + \frac{1}{j\omega C_0} + \sum_{n=1}^{N_{max}} \frac{R_n}{1 + jQ_n\frac{\omega}{\omega_n}\frac{\omega_n}{\omega}} \tag{2.25}$$

Where $Q_n = \omega_n R_n C_n$ and $\omega_n = (L_n C_n)^{-}0.5$. N_{max} is the number of modes needed to properly describe the antenna input impedance's frequency behaviour. ω is the operating radian frequency, and ωn is the radian frequency of the nth resonant mode. C_0 is the input capacitance, and L_0 is an inductance that takes account the higher-order modes and feeding effects. At the same time, R_n, C_n, L_n and Q_n are the resistance, capacitance, inductance and quality factor, respectively, describing the lumped resonance behavior in the antenna structure [45]. According to Foster's first canonical form, an equivalent circuit derived from the input impedance examines the impedance vs frequency curve. Based on the resonance and anti-resonance points, series or parallel RLC circuits model the equivalent circuit. Around resonance frequency, the antenna behaves as series RLC circuits where the derivative of the antenna reactance with respect to frequency is positive. At near anti-resonance ranges, the antenna acts as parallel RLC circuits, and the frequency derivative of the antenna reactance is negative [42]. In a finite frequency range, When the antenna reactance changes from negative (capacitive) to positive (inductive), the frequency derivative of the antenna reactance is positive. If the reactance of the antenna changes from a positive (inductive) to a negative (capacitive), the frequency derivative of the antenna reactance is negative.

2.5   Power Delay Profile

A transmitted signal can travel many different paths before reaching a receiver which causes the received signal strength to be degraded. The power delay profile gives the power strength of a signal received through a multipath channel as a function of propagation delay. It has many uses, specially for characterizing a multipath channel and channel estimation.
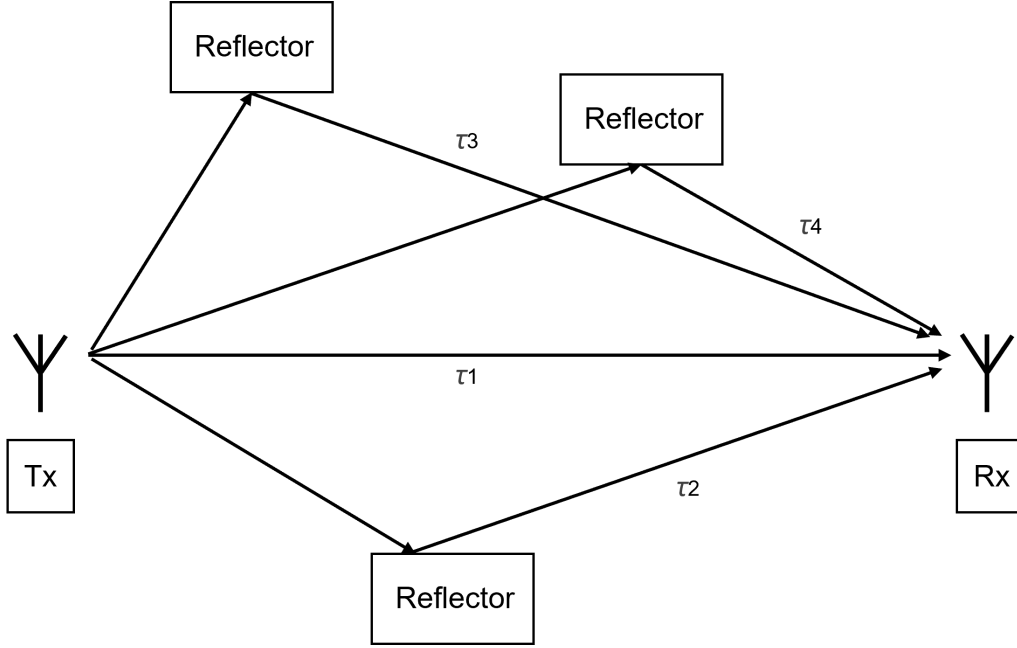
Figure 2.10. Multipath propagation scenario.

One can calculate the mean excess delay, RMS delay spread, maximum delay spread and coherence bandwidth from the power delay profile. The trade-off between the symbol rate and the complexity of the receiver system design can be determined from the delay spread analysis. Also, the cyclic prefix in an OFDM system is typically determined by the maximum excess delay or by the RMS delay spread of that environment [46]. Figure 2.10 shows the multipath propagation of the transmitted signal.

The other use of power delay profile is range estimation in various motion or location-based applications. Many localization techniques use range-based analysis to compute positions based on the received signal strength indicator (RSSI), representing the receiver's received power level [47, 48]. The received power strength measured from each signal path can estimate the path length between a pair of transmitters [49, 48]. In this thesis work, the power delay profile is used to measure the range between the transmitter and receiver, and range of a metal object as a sensing point of view. Power delay profile is a function of a channel impulse response. The following equation 2.26 calculates it.

$$P(\tau) = E[|h(t, \tau)|^2] \tag{2.26}$$

There are two categories to measure the channel impulse response: time-domain and frequency-domain measurements. However, the measurement setup is different in each case. Frequency domain measurement utilizes Vector Network Analyzer (VNA) to measure the complex channel impulse response, which is transmissivity $S_{21}(\omega)$ data over the sweep frequency range. This complex channel impulse response is converted to the time-domain bandlimited impulse response using Inverse Fourier Transform (IFT). After that,
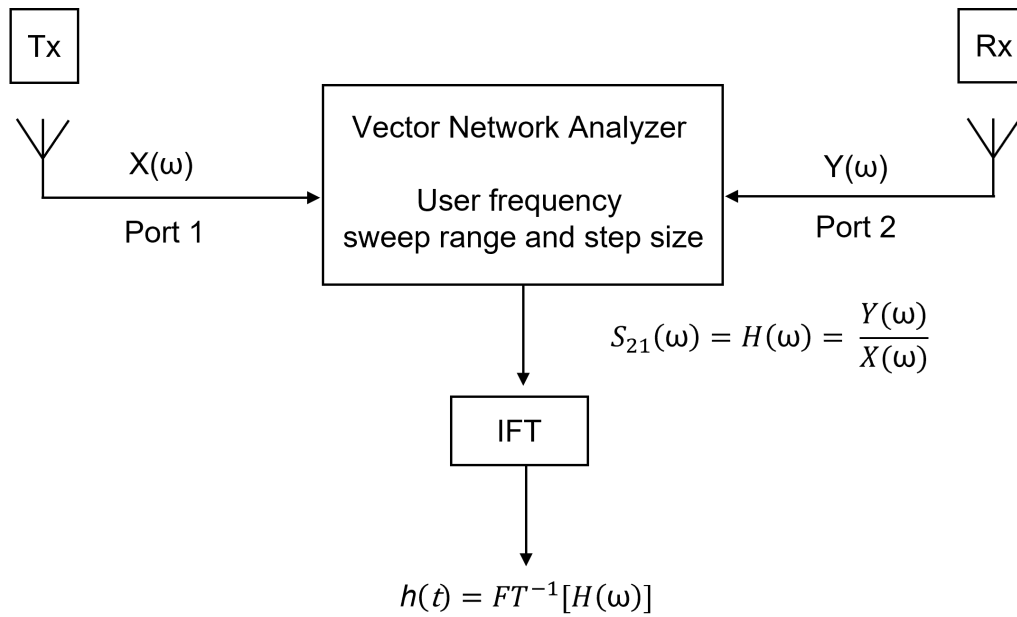
Figure 2.11. Frequency domain channel impulse response measurement. [50]

a Hamming window is applied to reduce the delay-domain side lobe level. Finally, PDP is calculated using the above equation 2.26, which is the delay vs PDP plot. Finally, the horizontal axis of the plot is converted from delay to distance to find the range. Figure 2.11 shows the frequency domain channel impulse response measurement in the block diagram.

3.   Wideband Antennas Design

In this thesis work, slotted ground plane and slot-loading in the radiator techniques are used to design UWB and wideband antenna (5.9-7.1 GHz), respectively. To achieve that, first, a planar narrowband microstrip patch antenna is designed at 5.8 GHz. Later, the slotted ground (Defected Ground Structure) technique with the partial ground is used to design the UWB antenna. For designing the wideband compact antenna (5.9-7.1 GHz), slots are introduced in the patch along with the partial ground. ANSYS High-Frequency Structural Simulator (HFSS) is used to model and analyse the design. The software utilizes the finite elements method (FEM) to compute numerical analysis of complex geometries and inhomogeneous mediums [51]. There are four main steps in creating and solving an accurate HFSS simulation:

1. Creation of the Model
2. Assigning the Boundaries
3. Assigning the Excitation
4. Solving and Simulating the Results

3.1   Narrowband Planar Microstrip Patch Antenna

Resonance frequency plays an essential role in antenna design for calculating the dimension. The dimension of the antenna is inversely proportional to the resonance frequency. The resonance frequency of the narrowband MPA is targeted at 5.8 GHz to compare the dimension of the designed antennas at a later part. RO4003 having a thickness of 0.508 mm and a dielectric constant of 3.55, is chosen as a substrate due to its low cost and low losses at high frequencies compared to other cheaper options like FR4. In addition to that, antenna bandwidth increases with the thicker substrate. Therefore, we wanted to achieve wide bandwidth without the help of a thick substrate. For designing the antenna, the microstrip line feeding-based technique is considered than the inset feeding technique. This causes the antenna to resonate at multiple resonant frequencies in a wideband design. The antenna patch length, width and feed length are 13.6 mm, 17.1 mm and 6.9 mm respectively at 5.8 GHz according to the equations 2.4-2.6 and 2.9 mentioned in chapter 2. Later, these values are optimized from simulation to match the antenna at 5.8 GHz. The impedance of the antenna is 205.21 Ω for the optimized antenna dimension. Therefore, a quarter-wavelength impedance transformer is needed to match the antenna impedance with the 50 Ω input impedance. The characteristic impedance of the quarter-wavelength

impedance transformer is calculated 101.29 Ω using equation $Z_o = \sqrt{Z_L Z_{in}}$. Here, Z_L is antenna impedance and Z_{in} is the 50 Ω input impedance. The below table 3.1 summarizes the optimized parameters of the narrowband MPA designed at 5.8 GHz. Figure 3.2 shows the antenna is matched to 5.8 GHz and has a fractional BW of 1.03%.

	Antenna parameters	Optimized	Theoretical
	Substrate Length, SubL	31.5 mm	28.65 mm
	Substrate Width, SubW	33.5 mm	20.15 mm
Substrate Material RO 4003	Patch Length, Lp	13.5 mm	13.6 mm
Dielectric Constant 3.55	Patch Width, Wp	17 mm	17.1 mm
Substrate Thickness 0.508 mm	Feed Length, Lf_50	4 mm	6.9 mm
Operating Frequency 5.8 GHz	Feed Width, Wf_50	1.14 mm	1.14 mm
	QW Feed Length, Lf_qw	8 mm	8.1 mm
	QW Feed Width, Wf_qw	0.28 mm	0.28 mm
	Antenna Impedance	205.2 [Ω]	204.7 [Ω]

Table 3.1. Narrowband microstrip patch antenna parameters.
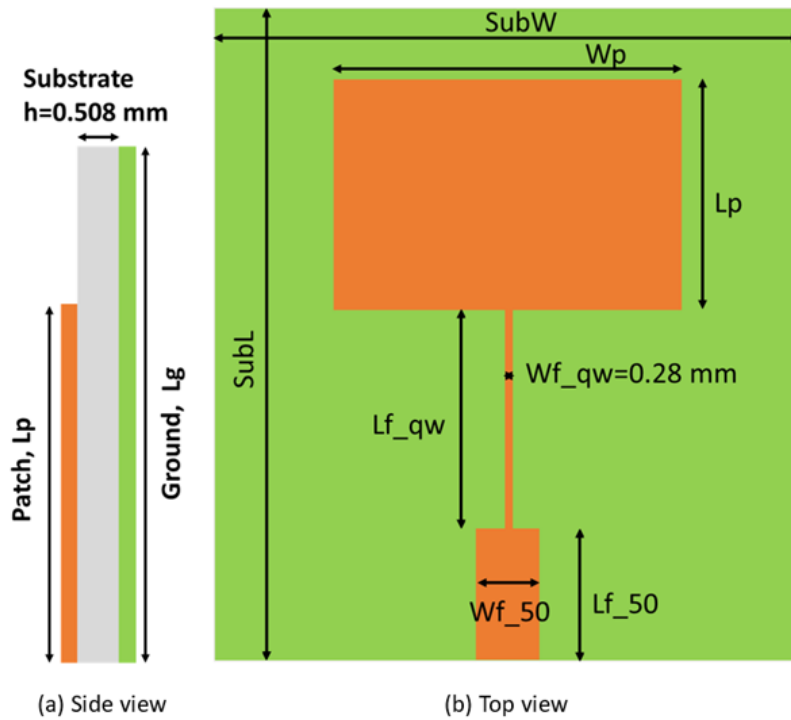
Figure 3.1. Narrowband patch antenna at 5.8 GHz (a) Side view (b) Top view.
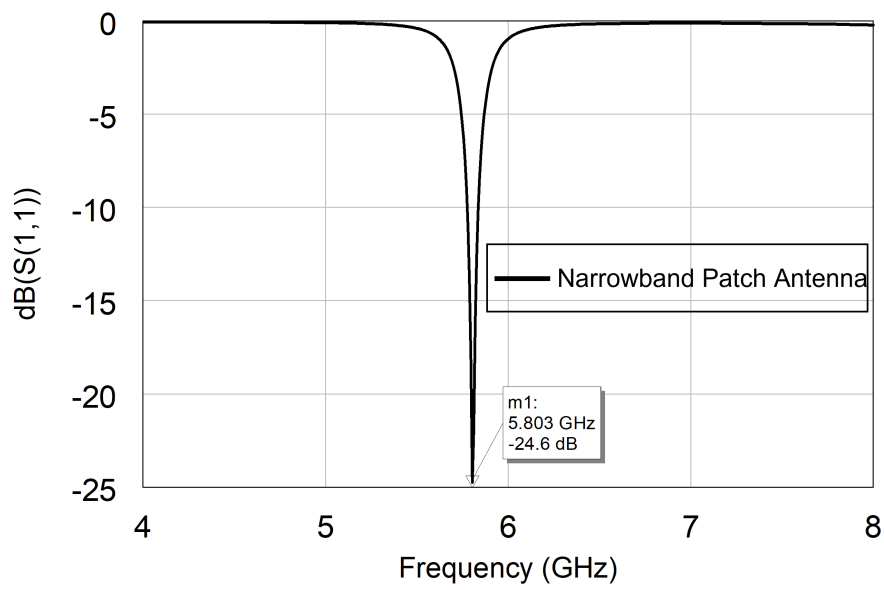
Figure 3.2. S_{11} parameter of narrowband patch antenna.
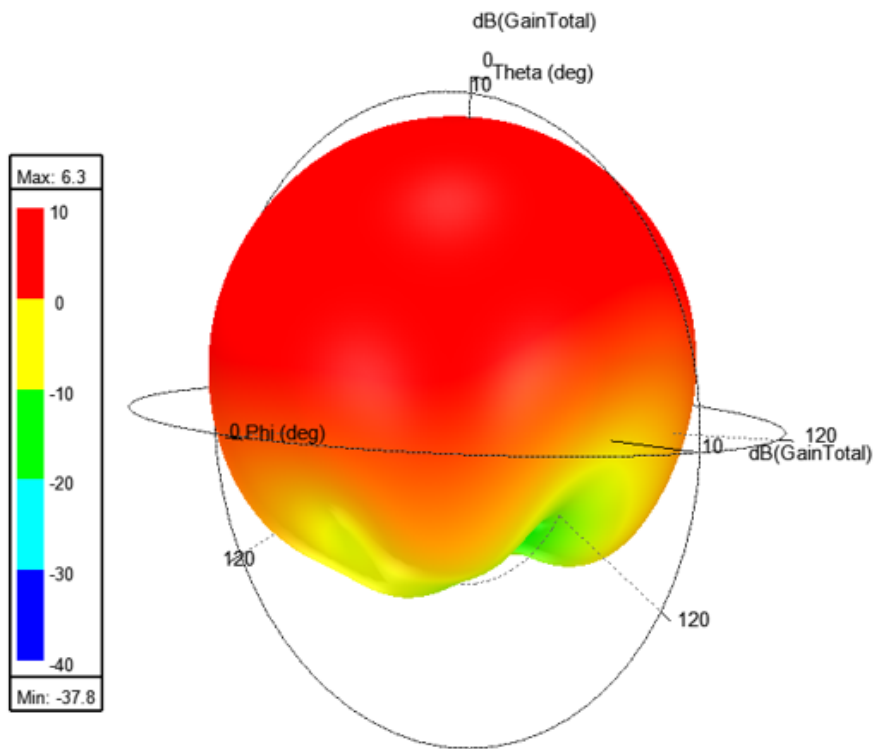
Figure 3.3. 3D gain of narrowband microstrip patch antenna.

3.2 Compact UWB Antenna Design

The narrowband antenna designed in the previous section is matched to a single frequency. However, for wideband operation, the matching network has to be a multisection transformer which will increase the overall dimension of the antenna. But, there are several other methods to improve the matching and increase the BW of the narrowband patch antenna. As mentioned in the chapter 2, methods like thick substrate, stacked patches, shorting pins, and defected ground structure (DGS) are used to improve the bandwidth of microstrip antennas and impedance matching. Therefore, this section uses defected ground structure (DGS) with partial ground to design the UWB antenna. Usually, a complete ground plane for the entire substrate below the patch causes the antenna to radiate in the broadside region. A finite ground plane helps to obtain an omnidirectional radiation pattern for the UWB antenna. Also, finite ground planes are capable of supporting multiple resonant modes. Overlapping closely spaced multiple resonant modes (f1, f2, f3,...fn) as shown in 3.4 can achieve wide bandwidth, and this is the idea of obtaining the UWB bandwidth. Methods like cutting steps at the bottom of the patch increase the distance
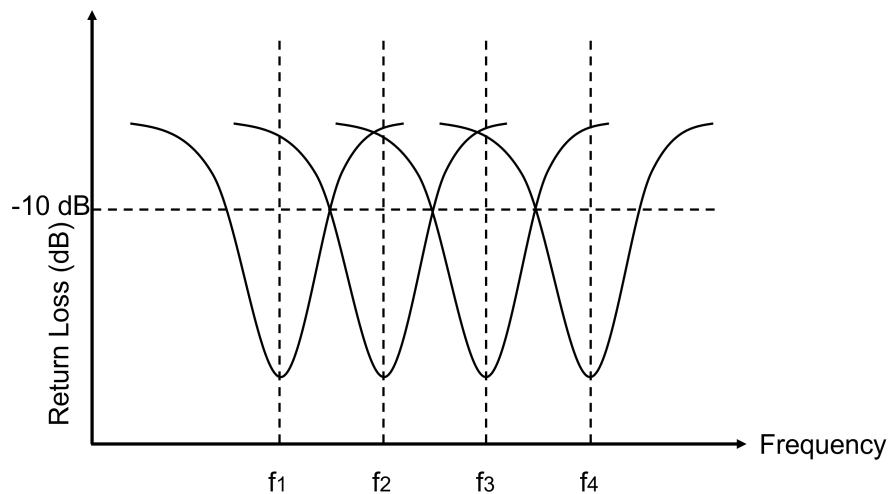
Figure 3.4. The concept of overlapping closely-spaced multiple resonance modes creating wideband.[52]

between the patch and the ground plane, which tunes the capacitive coupling between them [53], while the ground slot neutralizes the capacitive effects through the inductive nature of the patch to get nearly pure resistive input impedance [54]. Therefore, techniques like cutting the slot in the ground (DGS) and increasing the distance between the partial ground and patch are implemented to improve the matching and impedance BW.

24

3.2.1 Effect of Partial Ground and Bending

For designing a rectangular bending shape UWB patch antenna with partial ground as shown in figure 3.5, substrate and patch dimensions are kept similar to the previous narrowband design. Quarter-wavelength impedance transformer is removed, and a direct edge feeding microstrip line of 14 mm is used for feeding the antenna. The gap from the top edge of the ground plane to the bottom edge of the patch plays a significant role in matching the impedance and widening of the antenna BW. To find the required gap
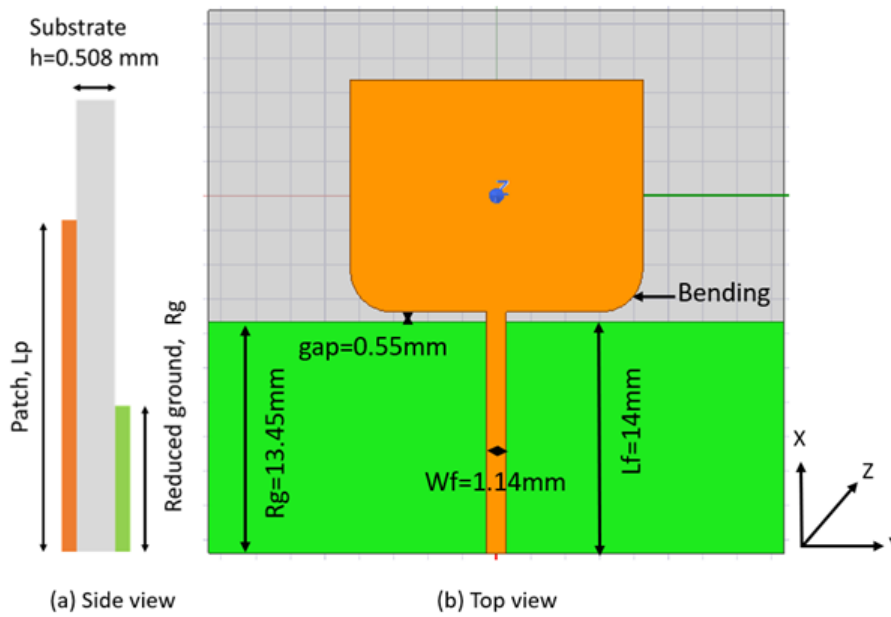
Figure 3.5. Antenna-1 W/O slot (a) Side view (b) Top view.
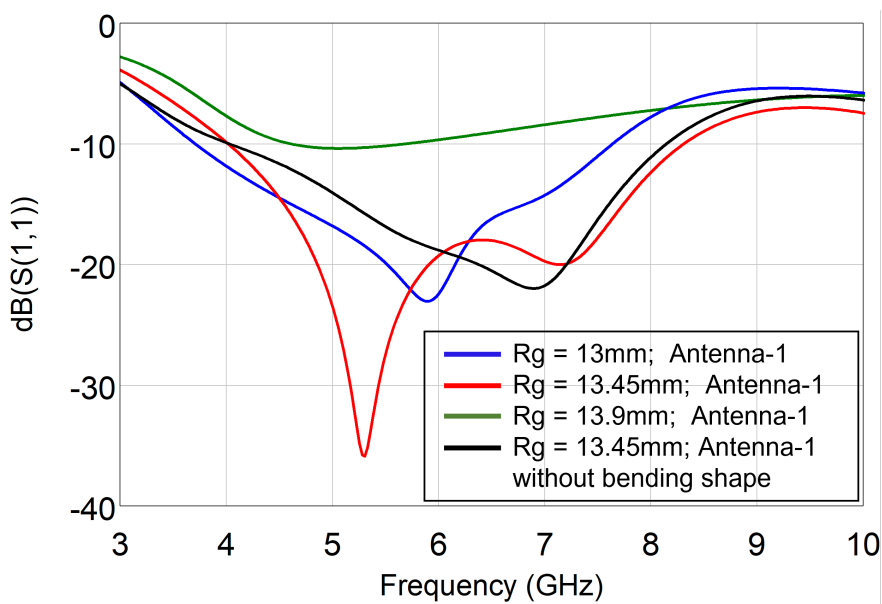
Figure 3.6. Parametric analysis of finite ground of the antenna-1 (W/O slot).

between the top edge of the ground and bottom edge of the patch, parametric analysis is performed in the HFSS. After parametric analysis, the gap of 0.55 mm for the finite ground (Rg=13.45mm) is selected. In figure 3.6, Rg=13.45mm shows better wideband and impedance matching. Also, the two resonance frequencies are below -10 dB. A gap smaller than 0.55 mm starts degrading the bandwidth and impedance matching. The bending shape in the patch tunes the capacitive coupling by increasing the distance between the bottom edge of the patch and the top edge of the ground, improving the impedance matching at 5.3 GHz and 7.1 GHz. The width of the tx line is kept constant at 1.14 mm for 50 Ω. SMA connector with wave port excitation is used to model the simulation as close as to the practical environment.

3.2.2 Effect of Slots in the Ground

Adding a slot in the ground plane changes the current distribution, creates additional resonance frequency at a higher frequency and improves the impedance matching [55]. Figure 3.7 shows the different antenna types discussed below for further BW improvement and impedance matching. The simulated antenna-1 has resonances at 5.6 and 7.1 GHz. To
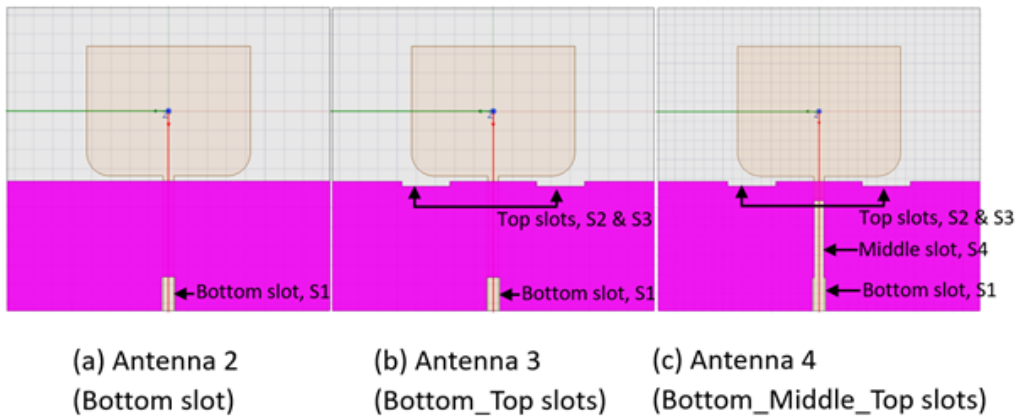
Figure 3.7. Different antenna types.

add another resonance at a higher frequency current distribution (magnitude) in the ground plane of antenna-1 is studied. Figure 3.8 shows the current distribution on the ground plane of antenna-1 around the two resonances as well as at 10.3 GHz. The bottom centre edge of the ground plane has high current distribution at 10.3 GHz, 7.1 GHz and 5.6 GHz. Therefore, adding a slot at the bottom centre edge of the ground will add a resonance at 10.3 GHz, as shown in figure 3.9. The resonance frequencies at 7.1 GHz and 5.3 GHz are shifted towards the lower frequency due to the high current distribution at the bottom center edge around these resonances. Table 3.2 provides all the physical dimensions of the necessary slots in the ground plane. Parametric analysis is used to find the proper size of slots used in the ground plane. In a similar way, the current distribution (magnitude)

Parameters	Value (mm)
S1_L	3.45
S1_W	1.4
S2,3_L	8
S2,3_W	1
S4_L	0.5
S4_W	5

Table 3.2. Ground slots dimension.
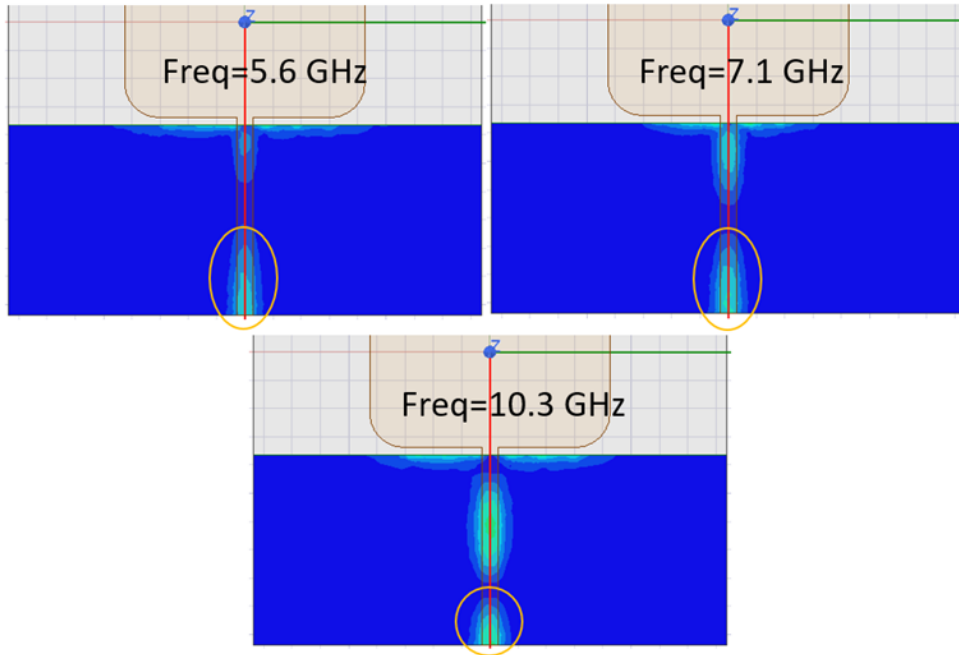
Figure 3.8. Current distribution (Magnitude) analysis on the ground plane of antenna-1 (W/O slot).
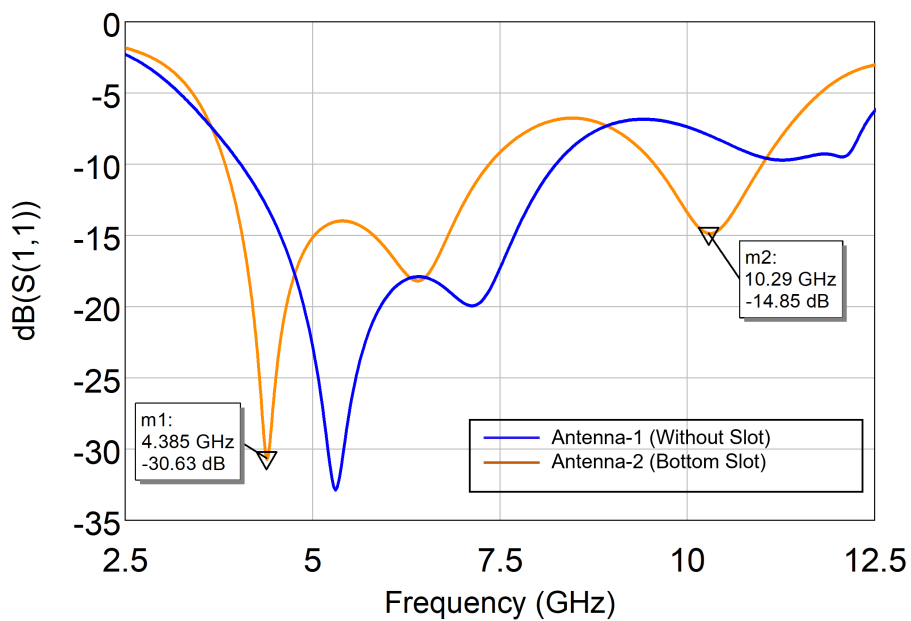
Figure 3.9. S_{11} parameter comparison between antenna-1 and antenna-2.
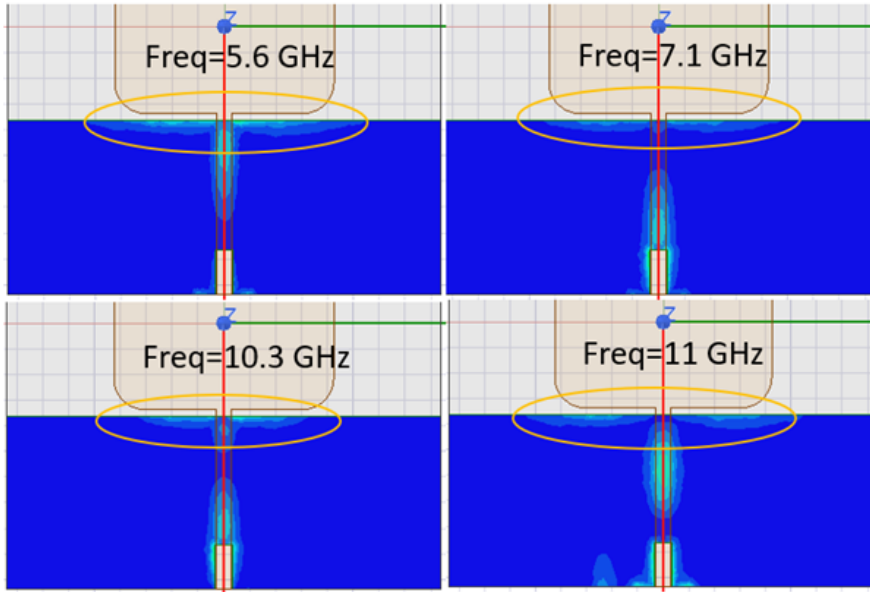
Figure 3.10. Current distribution (Magnitude) analysis on the ground plane of antenna-2 (Bottom slot).

is analysed for the antenna-2 to improve the impedance matching from 7.5 GHz to 9.5 GHz, where there is a band notch. Figure 3.10 shows that the top edge of the antenna-2 ground plane has high current distribution near the bending. Therefore, cutting two slots at the top edge of the ground plane of antenna-2 tunes the capacitive reactance. Figure
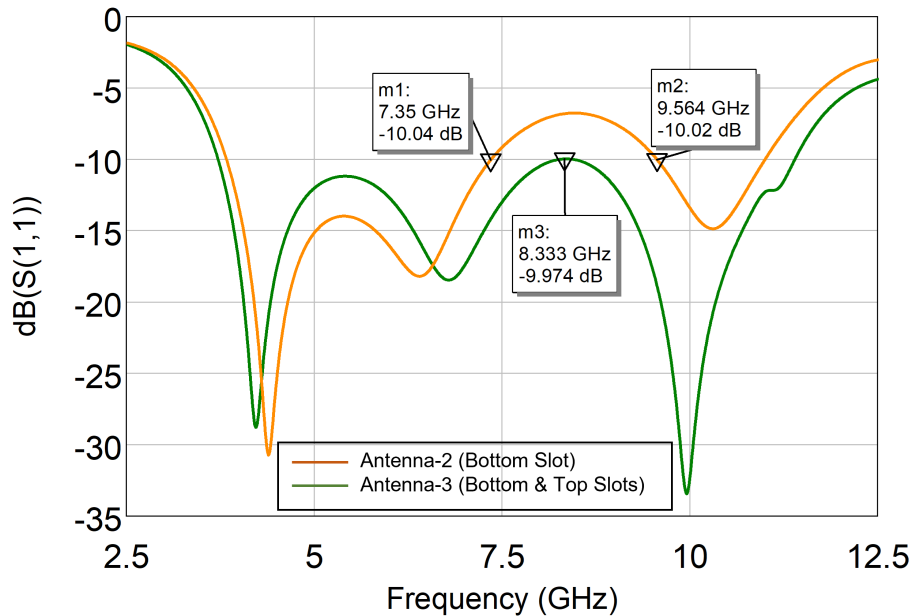
Figure 3.11. S_{11} parameter comparison between antenna-2 and antenna-3.

3.11 shows that band notch disappears for antenna-3 from 7.5 GHz to 11.4 GHz. Since the reflection coefficient of antenna-3 is still very close to -10 dB, current distribution is analysed again for antenna-2. Figure 3.10 shows that current distribution is high in the middle of the ground plane too. Therefore, placing a slot in the middle of the ground plane

brings down the S_{11} significantly below -10 dB. The total simulated BW for antenna-4 is observed from 3.8 GHz to 11.7 GHz as shown in figure 3.12. The fractional BW has increased to 101.9 % from the 1.03 % of the narrowband design. Figure 3.13 shows the simulated gain is 4.6 dBi at 8.75 GHz. The fabrication and measurement results will be presented in chapter 4 more in detail.
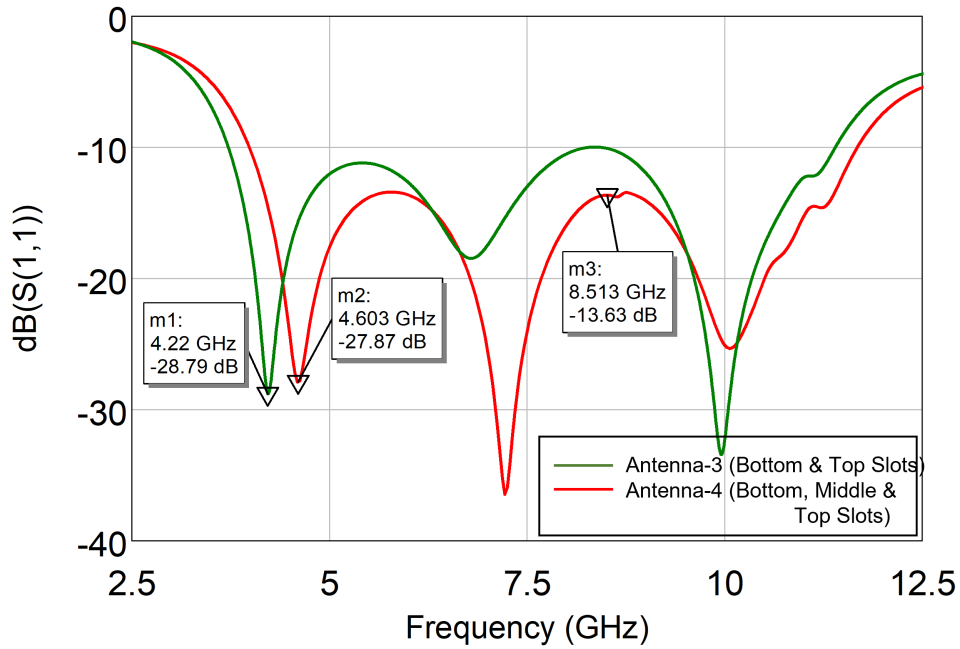
Figure 3.12. S_{11} parameter comparison between antenna-3 and antenna-4.
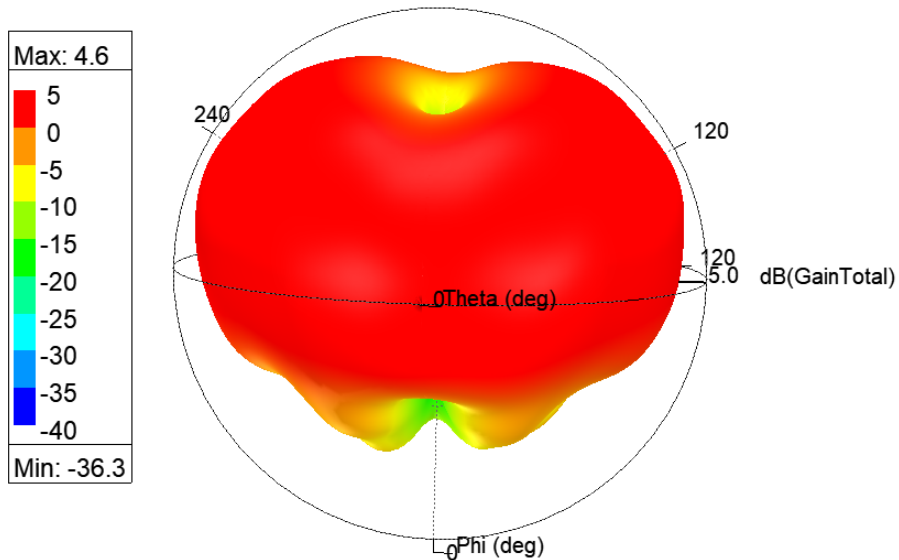
Figure 3.13. 3D gain of UWB antenna-4 at 8.75 GHz.

29

3.2.3 Equivalent Circuit Model

The Cadence AWR Design Environment platform is used in this section to develop the equivalent circuit. It is a electronic design automation software for developing RF/microwave products [56]. To get the circuit elements value for simulating the equivalent circuit in AWR, first, the input impedance of the antenna is obtained from HFSS simulations, as shown in figure 3.14. As shown in figure 3.14, the input impedance goes through 4 anti resonances at 4.81 GHz, 7.15 GHz, 9.5 GHz and 13.1 GHz. At each anti-resonance, the imaginary part almost crosses the zero line and has a negative derivative. At the same time, the real part of the input impedance has a local maximum. Therefore, in AWR, the input impedance is represented by four parallel RLC cells connected in series. The first parallel RLC cell represents the first band which resonates at 4.81 GHz. The second parallel RLC cell represents the resonance frequency at 7.15 GHz. The third and fourth parallel RLC cells represent the resonances at frequencies 9.5 and 13.1 GHz, respectively. The parallel LC cell at the end of the circuit is responsible for representing the bending effect of the antenna at low frequency. The proposed equivalent circuit model of the antenna-4 and element values of the designed UWB antenna-4 are shown in figure 3.15 and table 3.3, respectively. The final comparison of the real and imaginary parts of the input impedance obtained in HFSS and AWR are shown in figures 3.16 and 3.17, respectively. The HFSS results agree with the AWR with slight differences. The reason for this is that the structure simulator in the HFSS software accounts for all the coupling effects in the simulated antenna structure. In contrast, only the individual lumped elements are taken into account in the equivalent circuit model without accounting for their coupling.

	Z_n	Z_0	Z_1	Z_2	Z_3	Z_4	Z_5
In AWR	R_n (Ω)		39	42	49	190	
	C_n(pF)	1.3	3	2.246	1.93	3.5	2.24
	L_n(nH)	0.65	0.352	0.226	0.146	0.0425	1.425
	f_n(GHz)		4.81	7.15	9.5	13.1	
In HFSS	R_n (Ω)		50.82	51.7	63	185.3	
	C_n(pF)	1.425	3.9	11.21	2.63	2.066	
	L_n(nH)	0.65	0.281	0.045	0.107	0.0715	
	f_n(GHz)		4.81	7.15	9.5	13.1	

Table 3.3. Element values of the equivalent circuit model of the designed UWB antenna-4.
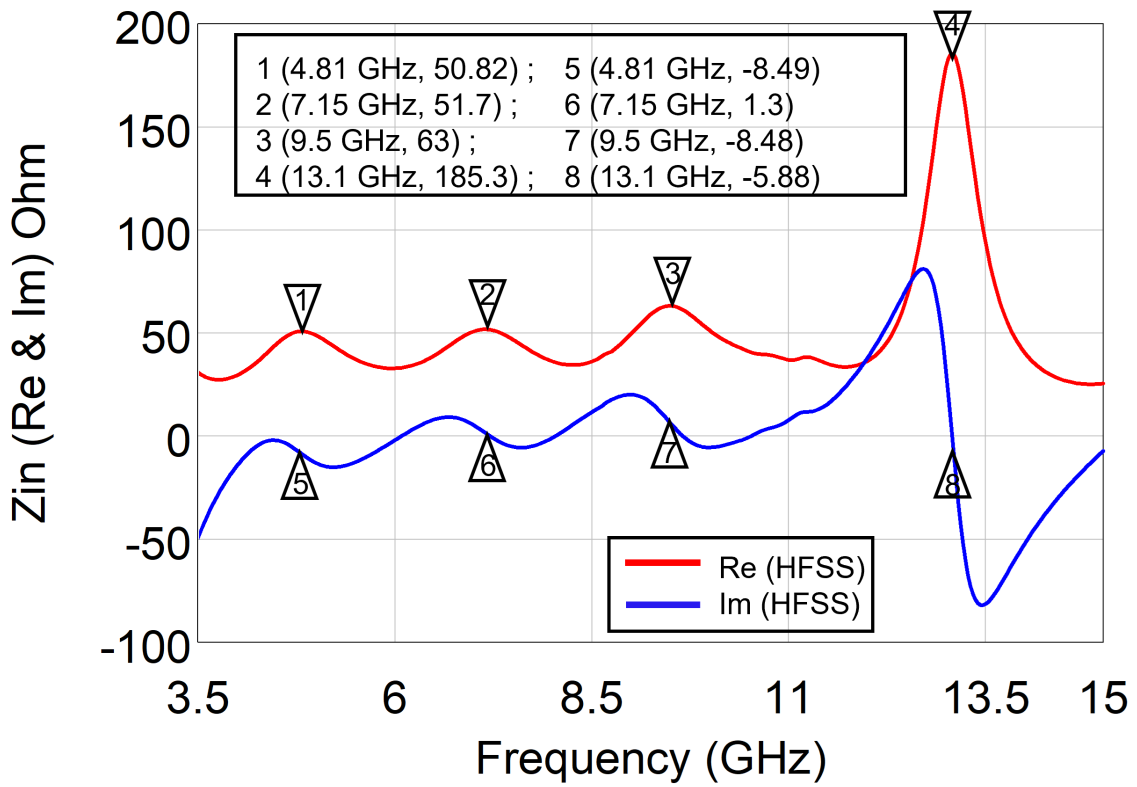
Figure 3.14. Input impedance of designed UWB antenna-4 in HFSS.
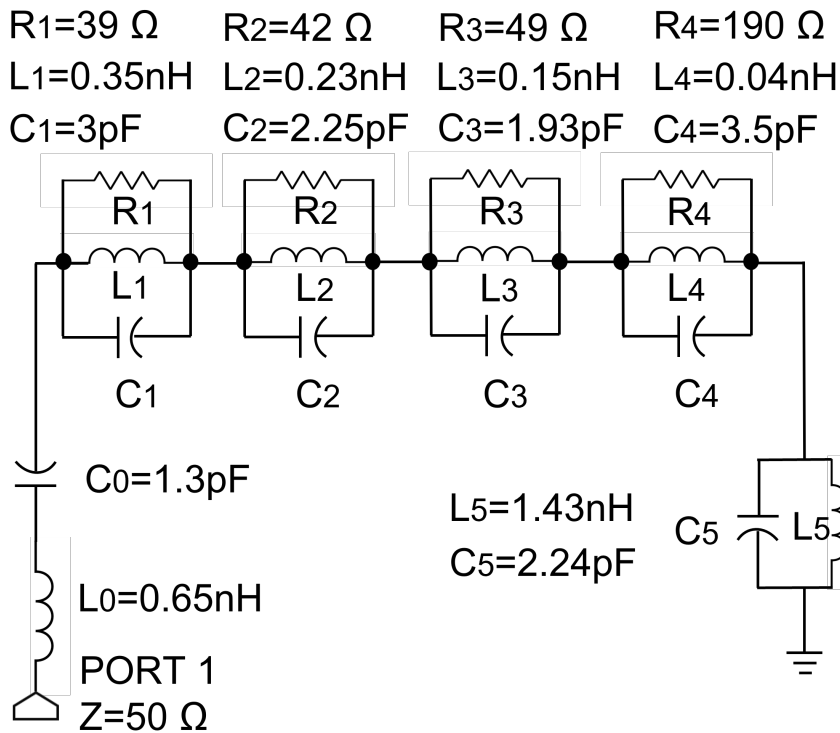
Figure 3.15. Equivalent circuit model of the designed UWB antenna-4 in AWR.
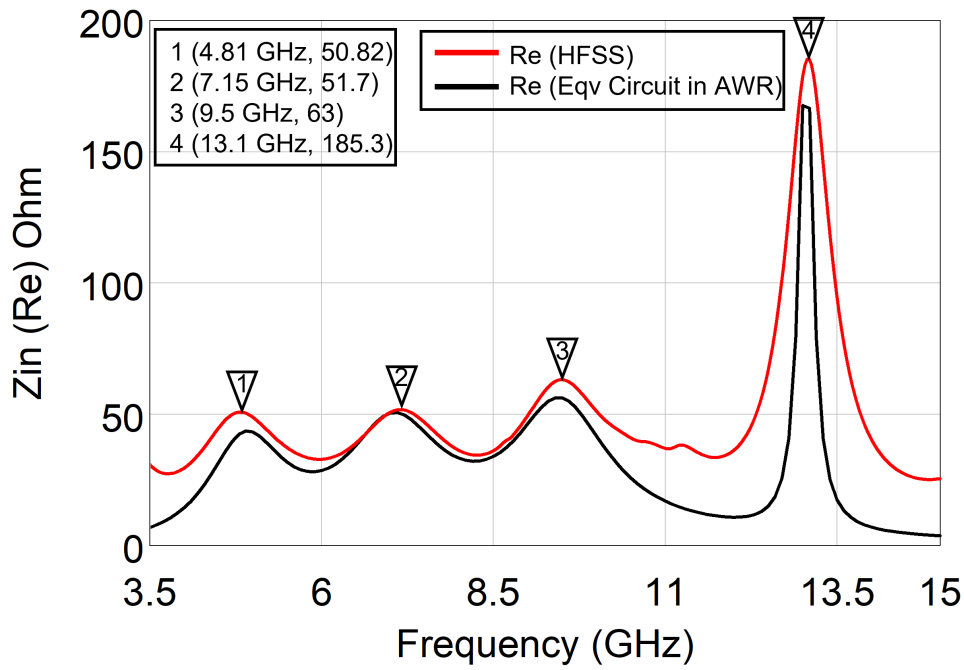
Figure 3.16. Input impedance (Real) comparison of UWB antenna-4 in HFSS vs AWR.
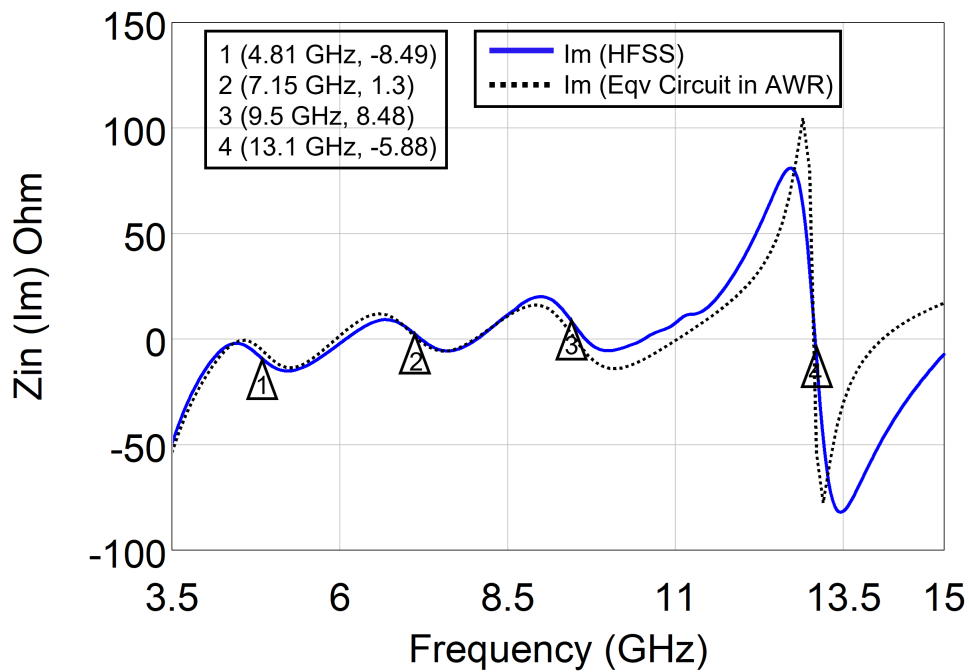
Figure 3.17. Input impedance (Imaginary) comparison of UWB antenna-4 in HFSS vs AWR.

3.3 Compact Wideband Antenna Design (5.9-7.1) GHz

According to the Functional Requirement Document (FRD) [57] published by the IEEE 802.11bf Task Group (TGbf), Wi-Fi sensing will use the license-exempt frequency bands between 1 GHz and 7.125 GHz and above 45 GHz. From IEEE 802.11ax (Wi-Fi 6) onward, Wi-Fi technology is ready to utilize the additional 1.2 GHz band between 5.925 and 7.125 GHz. For IEEE 802.11bf, this new spectrum band will allow the usage of large bandwidths – up to 320 MHz [58]. In Wi-Fi 6, there are 20, 40, 80 and 160 MHz channels. These channels are subdivided into subcarriers which are grouped into smaller frequency allocations called resource units (RUs). The subcarrier spacing is 78.125 kHz, and a single RU consists of a minimum of 26 tones and a maximum of 996 tones in Wi-Fi 6. Therefore, for a bandwidth of 320 MHz (IEEE 802.11bf), the subcarriers will increase to 996x2, making the CSI measurement finer-grained and severely improving the performance of Wi-Fi sensing. Hence, a compact wideband antenna working from 5.9 GHz to 7.1 GHz is designed in this thesis work. Step by step techniques are discussed in the below.

Effect of Partial Ground and Slots in the Patch:

This section uses the Slot-loading technique in the patch to design the compact wideband antenna (5.9-7.1 GHz). The same substrate with 0.508 mm height is used for this design as it was for UWB antenna. Partial ground method is followed for widened the BW and improving the impedance matching. The insertion of slots in the patch element highly affected the current distribution. Therefore, a very small antenna size (6mm x 8mm) is considered for the initial design and impedance matching is done using the partial ground. Later, slots are introduced in the patch element based on the current distribution to shift the resonance frequency in the lower side and band notch the frequency above 7.1 GHz so that the antenna radiates only from 5.9 to 7.1 GHz. Figure 3.18 shows the small size antenna with partial ground for initial stage. From figure 3.19, the S_{11} is below -10 dB from 8 GHz to 14.5 GHz which is outside the desired frequency range. Although, the BW is widened as expected for partial ground. Now, to shift the resonance frequency towards the lower side, current distribution (vector) analysis is computed on the patch element of WB antenna-1. From figure 3.20, there are mainly vertical currents in the patch. Therefore, placing slots in the patch normal to the current path will force the current to take a longer path. Hence, the patch length will become long for the current, resonating from the lower frequency. Figure 3.21 shows two slots are cut from the patch's top corners, which partially block the direct vertical current flow. Parametric analysis is done to select the proper slot length of $S1\_L$. Figure 3.22 shows the parametric study of the influence of slot lengths (step size of 0.5 mm) with their respective S_{11} parameters. Increasing the slot length forces the current to take a longer path and lowers the resonance frequency, as shown in figure
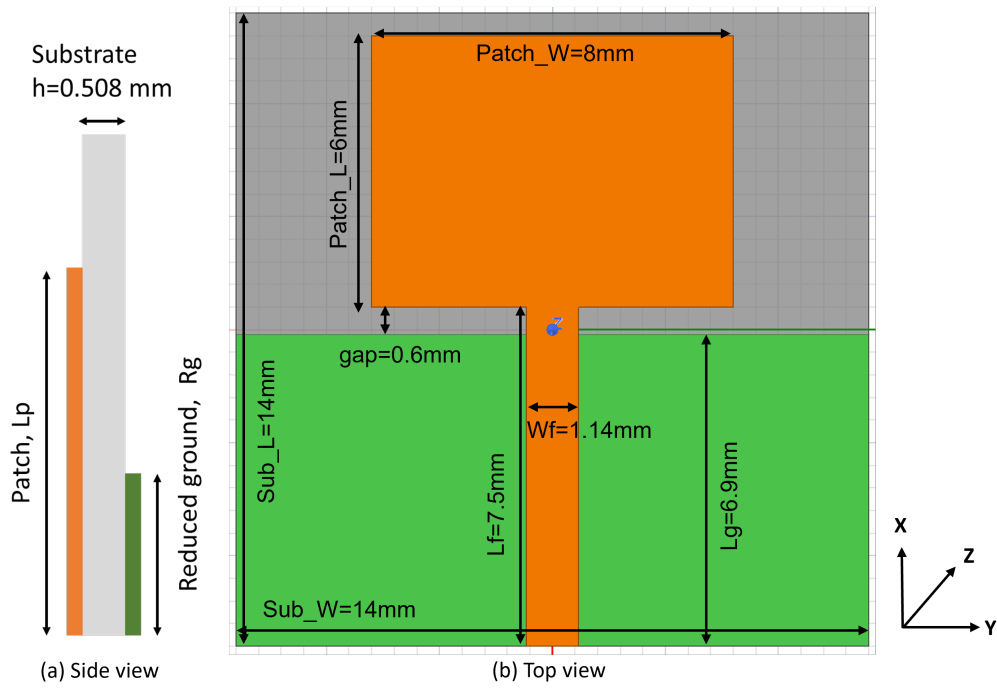
Figure 3.18. Wideband antenna-1 without slot (a) Side view (b) Top view.
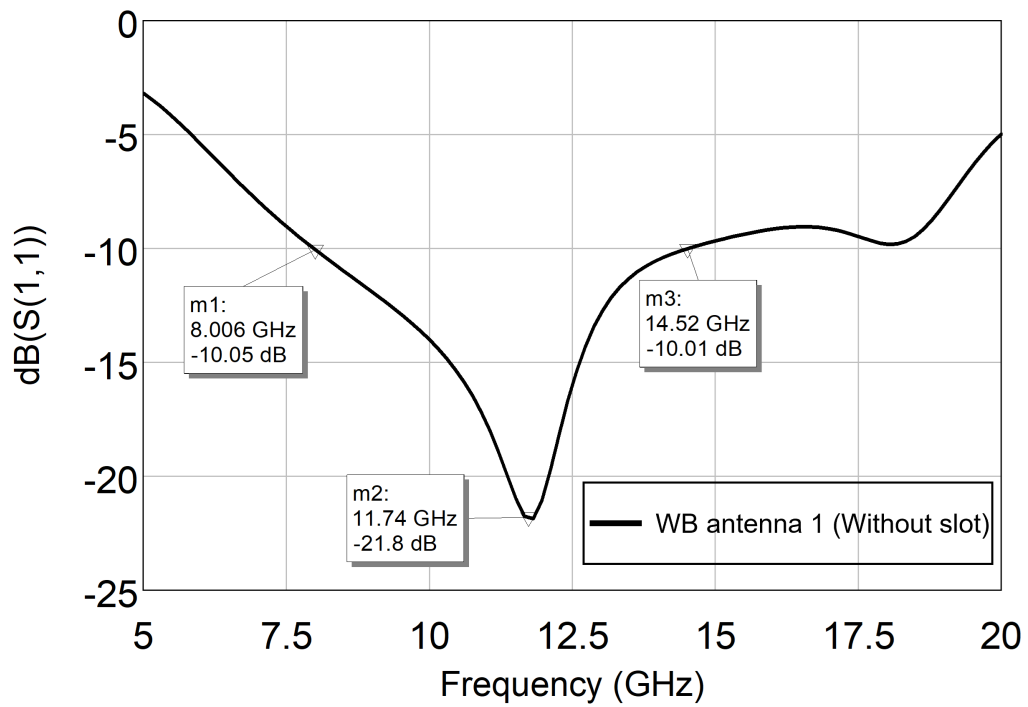
Figure 3.19. S_{11} parameter of wideband antenna-1 (Without slot).
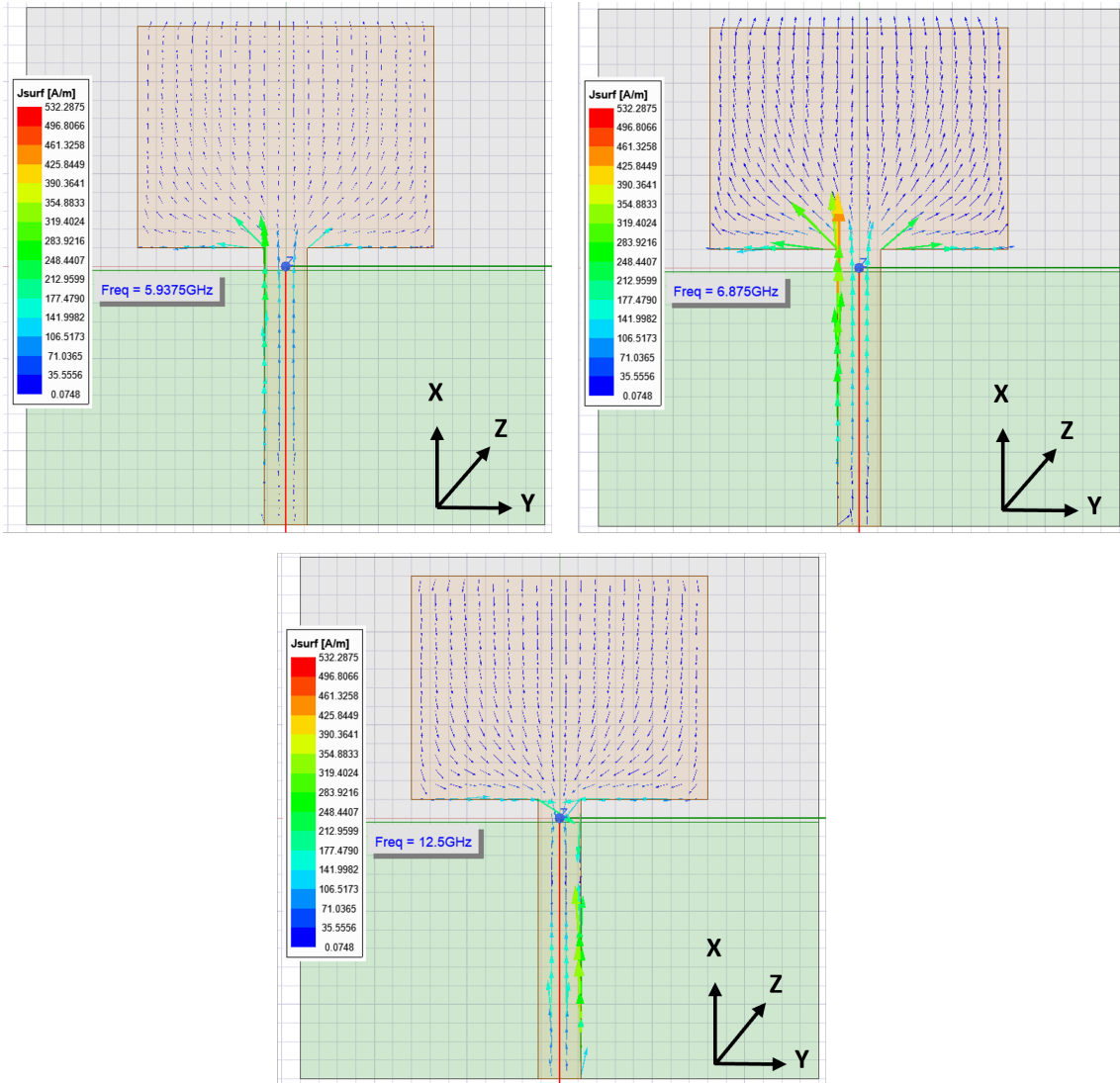
Figure 3.20. Current distribution (Vector) analysis on the patch of wideband antenna-1 (Without slot).
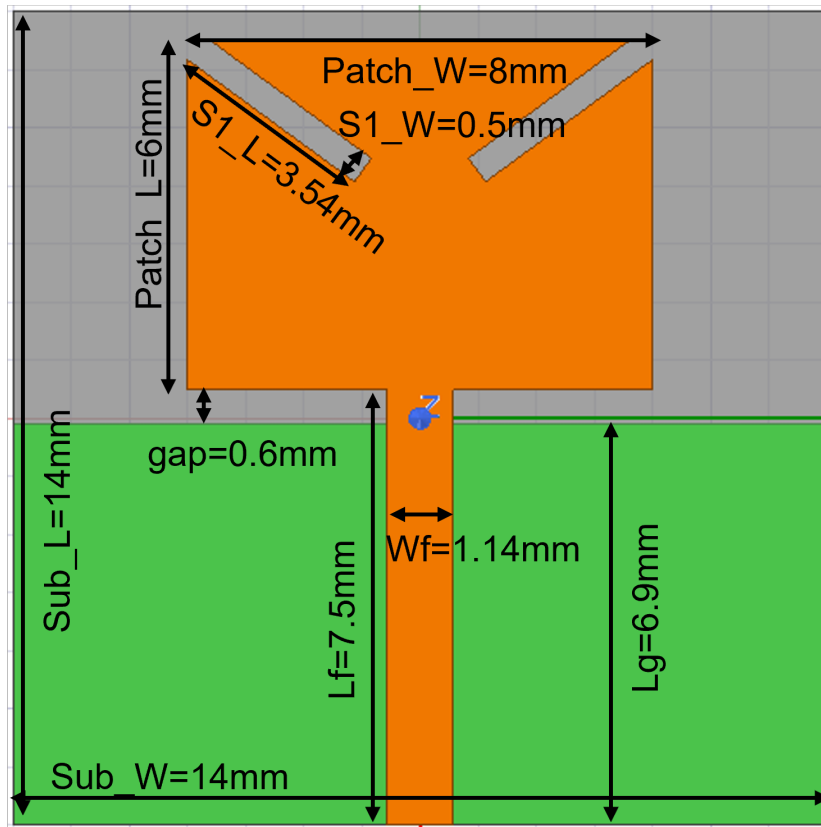
Figure 3.21. Wideband antenna-2 with top corners slots.
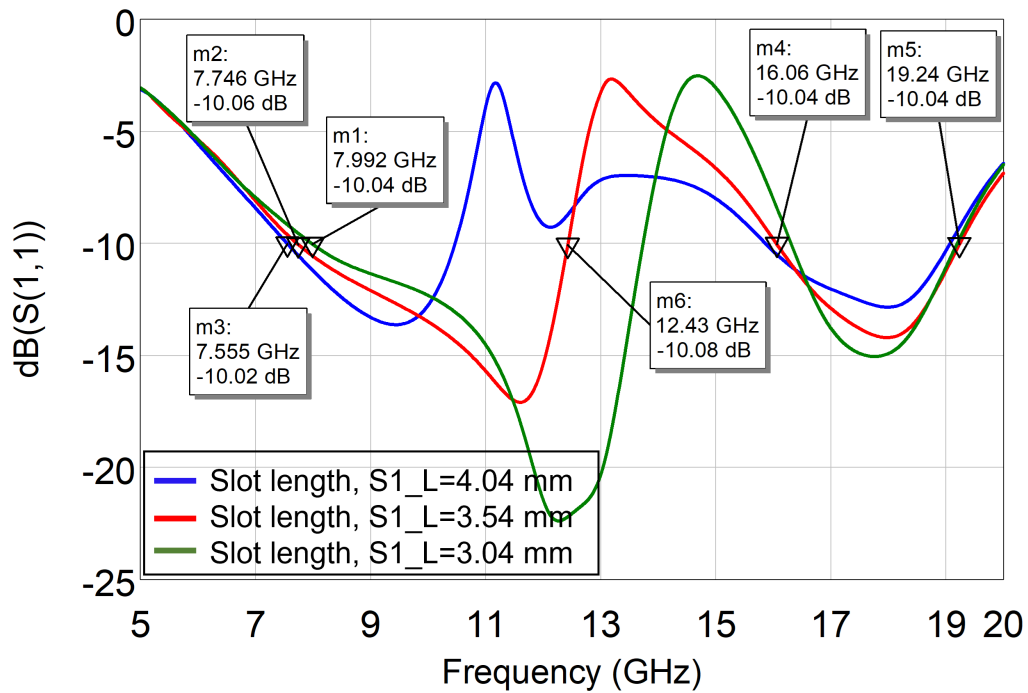
Figure 3.22. Parametric analysis of WB antenna-2 with top corners slots.

36

3.22. With the increasing length of the slot, the impedance matching and BW are also becoming poor. Therefore, the slot length of $S1\_L$= 3.54 mm is chosen for the next stage of compact WB antenna design. The WB antenna-2 (slot length of 3.54 mm) has a 2nd
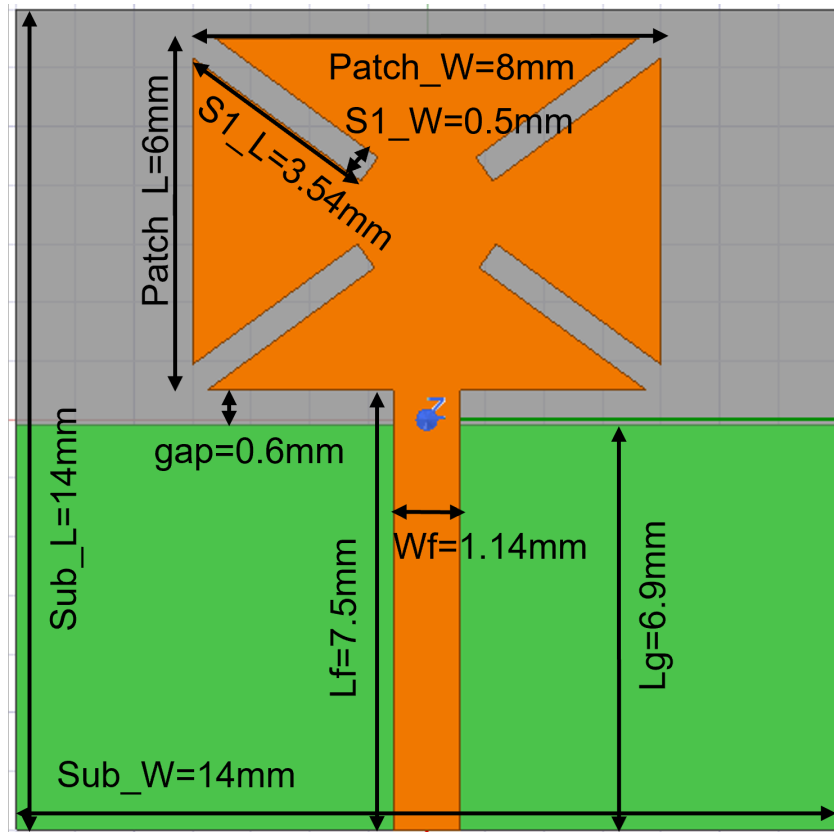
Figure 3.23. Wideband antenna-3 with top and bottom corners slots.

resonance from 16 GHz to 19.2 GHz, and the 1st resonance is still outside the desired range, as shown in figure 3.22. Therefore, two additional bottom corner slots are cut in the patch to band notch the 2nd resonance and lower the 1st resonance further. Figure 3.23 shows the WB antenna-3 having the bottom corner slots of the same dimension as the WB antenna-2. Figure 3.24 shows the S_{11} comparison of the WB antenna-2 and antenna-3. The additional bottom corner slots further force the current to take the longer path. Hence, the WB antenna-3 resonates from the lower frequency and notch the high-frequency band. In order to further lower the resonance frequency, horizontal slots are introduced in the bottom part of the antenna-4, as shown in figure 3.25. The new slot dimension is chosen after the parametric analysis. The desired frequency range is achieved with the slots length of 2.42 mm. The parametric study of figure 3.26 shows that the BW can be further increased or reduced by changing the horizontal slot length. The proposed wideband antenna-4 parameters are given in the table 3.4. Figure 3.27 shows the antenna has gain of 2.2 dBi at 6.8 GHz.
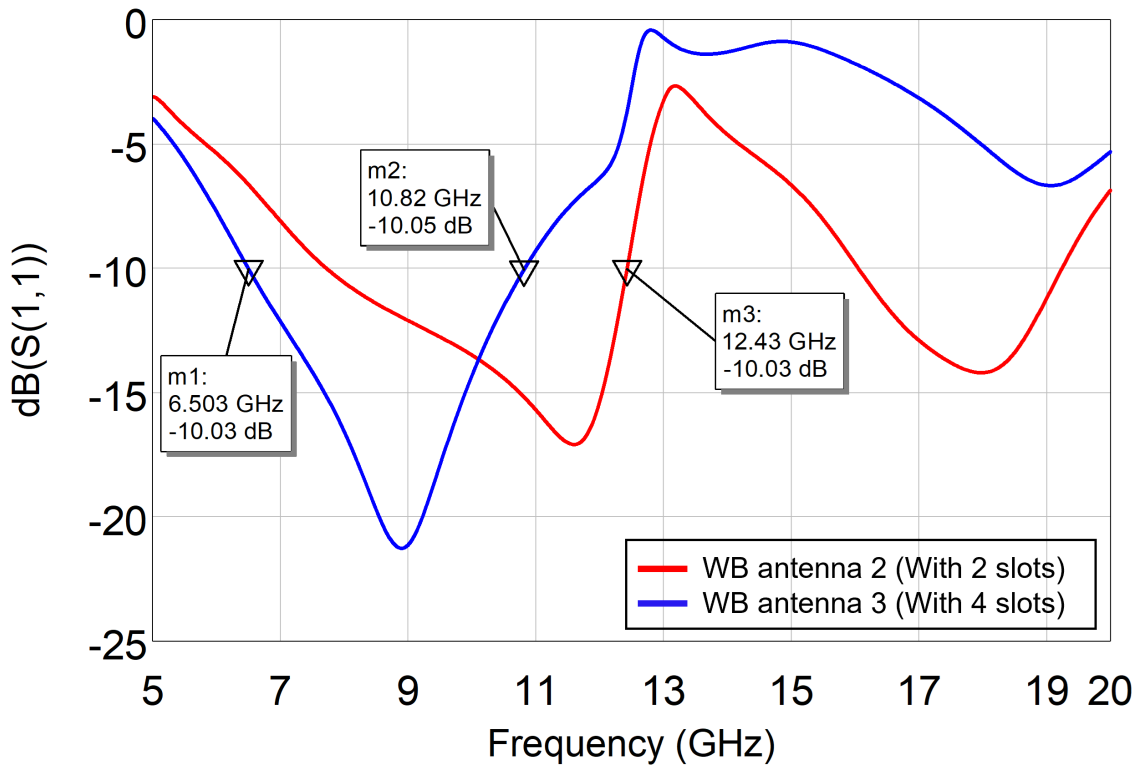
Figure 3.24. S_{11} comparison of WB Antenna-2 (2 slots) and antenna-3 (4 slots).
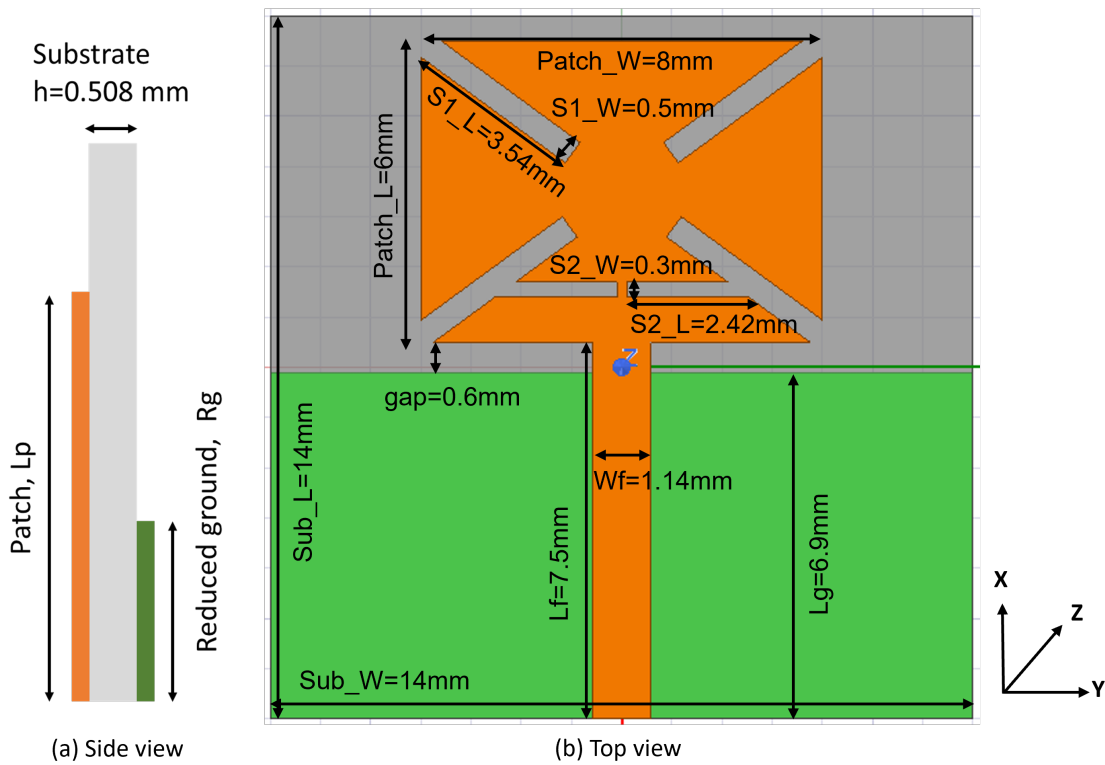
Figure 3.25. Proposed wideband antenna-4 for Wi-Fi sensing application (a) Side view (b) Top view.
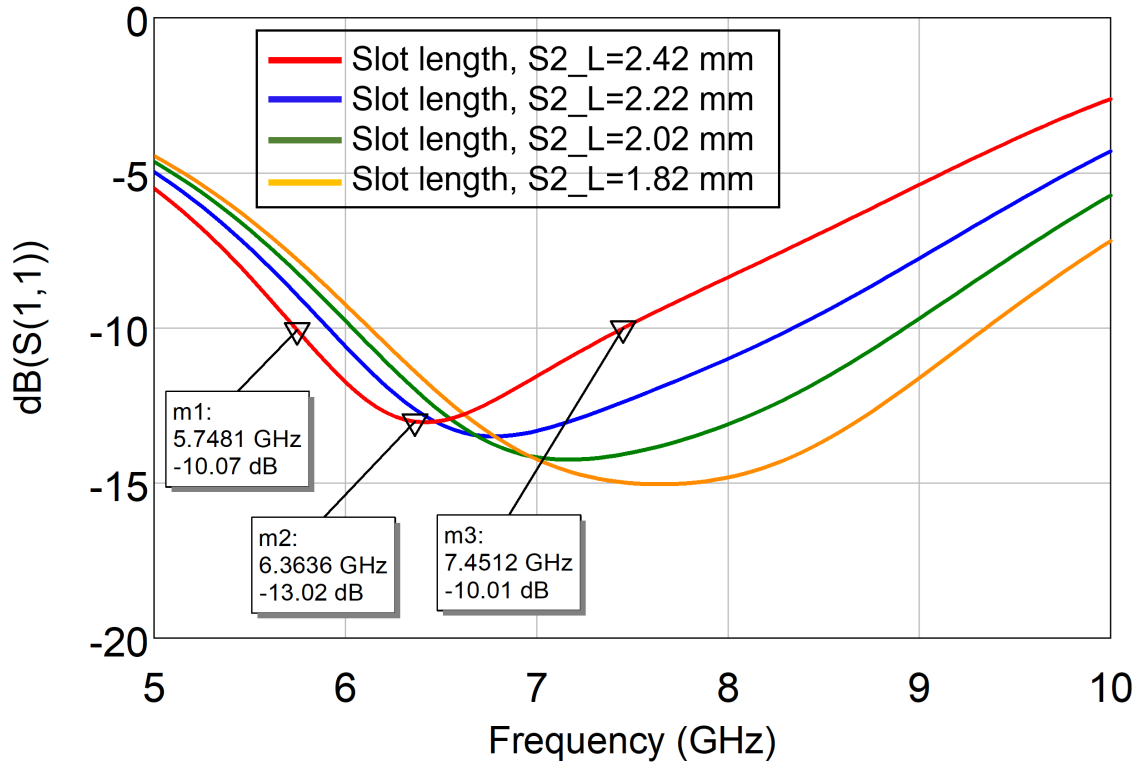
Figure 3.26. Parametric analysis of horizontal slot length of the antenna-4.

Substrate Material	RO 4003
Dielectric Constant	3.55
Substrate Thickness [mm]	0.508
Center Frequency [GHz]	6.5
Substrate Length, SubL [mm]	14
Substrate Width, SubW [mm]	14
Patch Length, Lp [mm]	6
Patch Width, Wp [mm]	8
Feed Length, Lf_50 [mm]	7.5
Feed Width, Wf_50 [mm]	1.14
Partial Ground Length, Lg [mm]	6.9
Gap, [mm]	0.6
Slot 1 Length S1_L [mm]	3.54
Slot 1 Width S1_W [mm]	0.5
Slot 2 Length S2_L [mm]	2.42
Slot 2 Width S2_W [mm]	0.3

Table 3.4. Proposed wideband antenna-4 parameters.
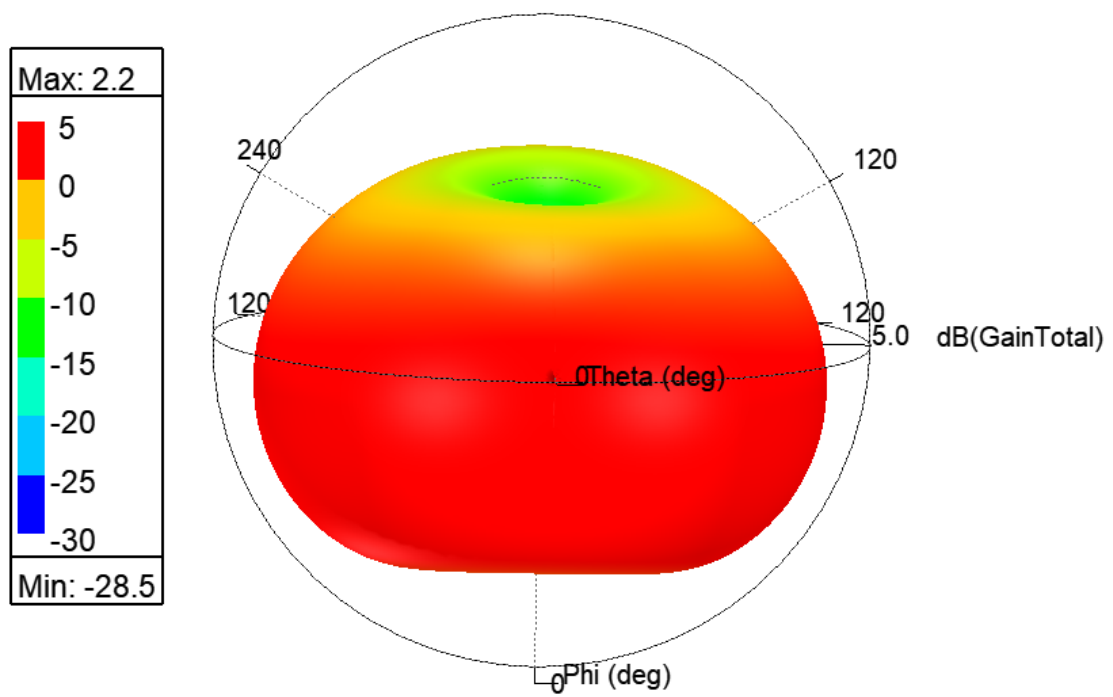
Figure 3.27. 3D gain of the proposed wideband antenna-4 at 6.8 GHz.

4. Fabrication and Measurement Results

The measurement results of the proposed UWB and wideband antenna (5.9-7.1 GHz) from chapter 3 are presented in this chapter. Therefore, this chapter is subdivided into two sections- UWB antenna and wideband antenna (5.9-7.1 GHz). Each section consists of return loss, gain, radiation efficiency and radiation pattern measurements. The communication and sensing experiment is performed for the UWB antenna and presented in the UWB section. Normal laboratory environment is used for measuring the S_{11}, whereas an anechoic chamber (under construction) is used to measure the radiation pattern. The fabrication and measurement equipment and processes used in this thesis work are also described here.

4.1 UWB Antenna

The UWB and Wideband antennas are fabricated via 3D printing technology and the standard PCB manufacturing process [59]. The equipment used to fabricate is LPKF ProtoMat, as shown in figure 4.1. The fabrication method involves converting the HFSS design files into Gerber files via the AWR software program. These files are required to work on the LPKF machine, which allows the printing designed antennas on the substrate. The LPKF machine makes the contour lines on the substrate where the copper is to be removed and draws the shape of the antennas. Then, it removes the copper from unwanted areas. Photographs of the fabricated UWB antenna prototype is shown in figure 4.2.

4.1.1 Return Loss Measurement

KEYSIGHT PNA model N5224B [61] working in the frequency range from 10 MHz to 43.5 GHz, is used to verify the performance of the developed antennas. At first, the required frequency range (2.5-12.5 GHz) and transmitted power of 0 dBm are selected in the PNA. Then, The PNA is calibrated using the Smart Cal calibration tool provided with the PNA. After the calibration, the fabricated antenna is connected to port 1 of the PNA for S_{11} measurement. Figure 4.3 shows the final UWB antenna model in HFSS. A comparison of simulated and measured return loss (S_{11}) is shown in figure 4.4. The S_{11} of the fabricated antenna shows impedance BW of 7.1 GHz (3.9-11 GHz), whereas, from the simulation, it is 7.9 GHz (3.8-11.7 GHz). The slight mismatches might be the measurement performed in the normal lab environment rather than an anechocic chamber.

Figure 4.1. LPKF ProtoMat machine [60].

Top view
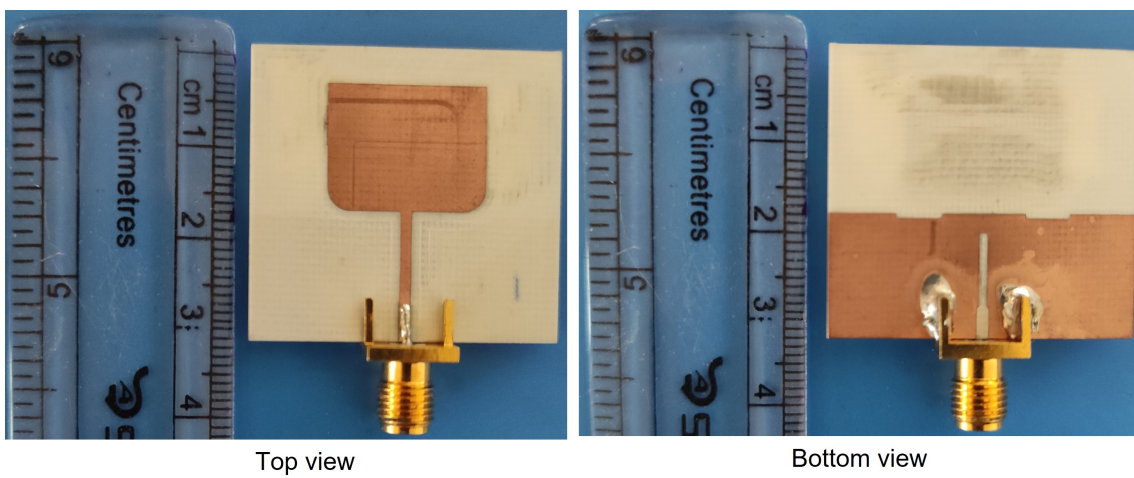
Bottom view

Figure 4.2. Fabricated UWB antenna left (Top view) right (Bottom view).
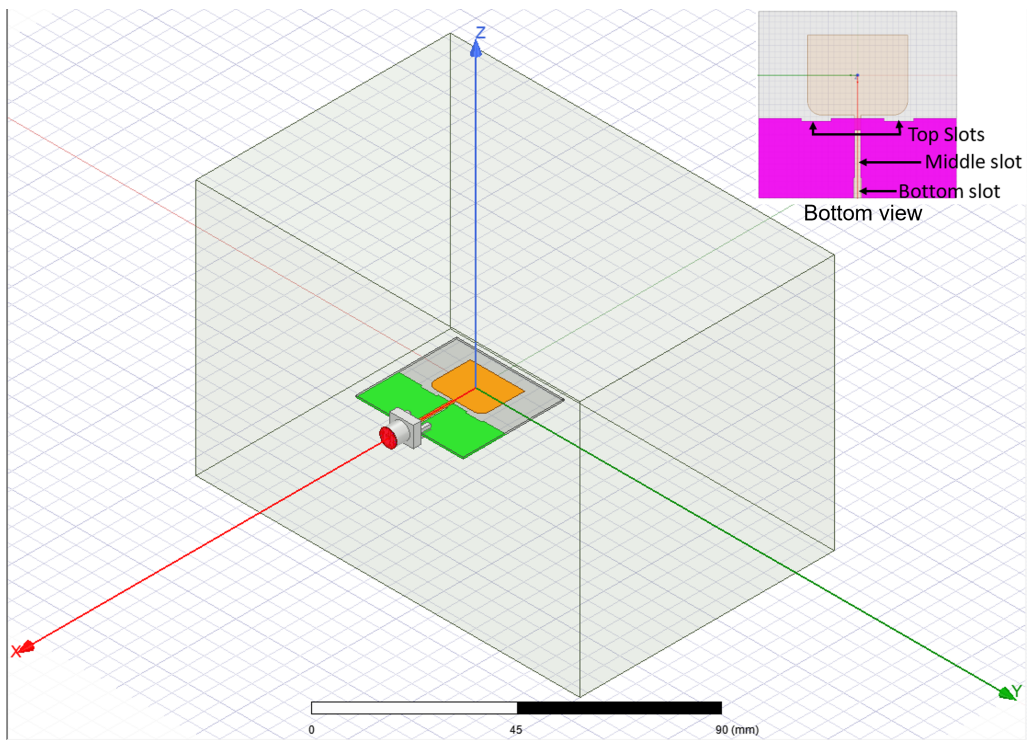
Figure 4.3. Final UWB antenna-4 model in HFSS.
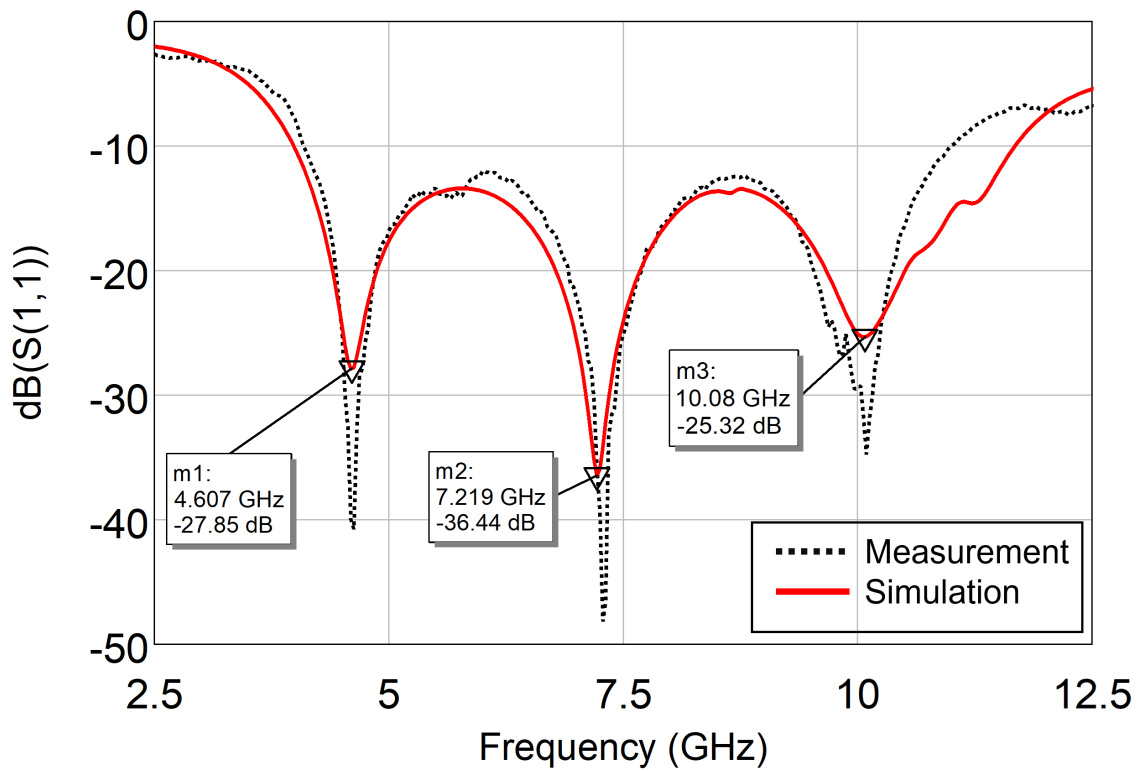
Figure 4.4. S_{11} of fabricated UWB antenna-4 (simulation vs measurement).

43

4.1.2   Gain Measurement

Diamond Automated Measurement System (DAMS) positioner is used for E, H plane and gain measurements. Figure 4.5 and figure 4.6 show the measurement procedure for DAMS positioner and GUI of the measurement software. The measurements were carried out in an anechoic chamber (under construction). After completing the calibration of the PNA using long coaxial cables, port 1 is connected to the DUT UWB antenna, and port 2 to the reference wideband horn antenna. The positioner rotates the DUT UWB antenna 180 degrees for the E-plane (due to hardware issue) and completes 360 degrees for the H-plane measurement. Figure 4.8 shows the radiation pattern of the structure simulated and measured for the E-plane (XZ direction) and H-plane (YZ direction) at 7.1, 8.75 and 10 GHz frequencies. The results exhibit omnidirectional behaviour in the wide frequency range. The mismatches between the results in certain angles are due to the open ceiling and uncovered areas of the chamber. Figure 4.7 shows the gain and radiation efficiency of the proposed UWB antenna. The UWB antenna has a gain of 2-6 dBi from 3.7-11.7 GHz. The radiation efficiency is above 90% in our desired frequency of operation.
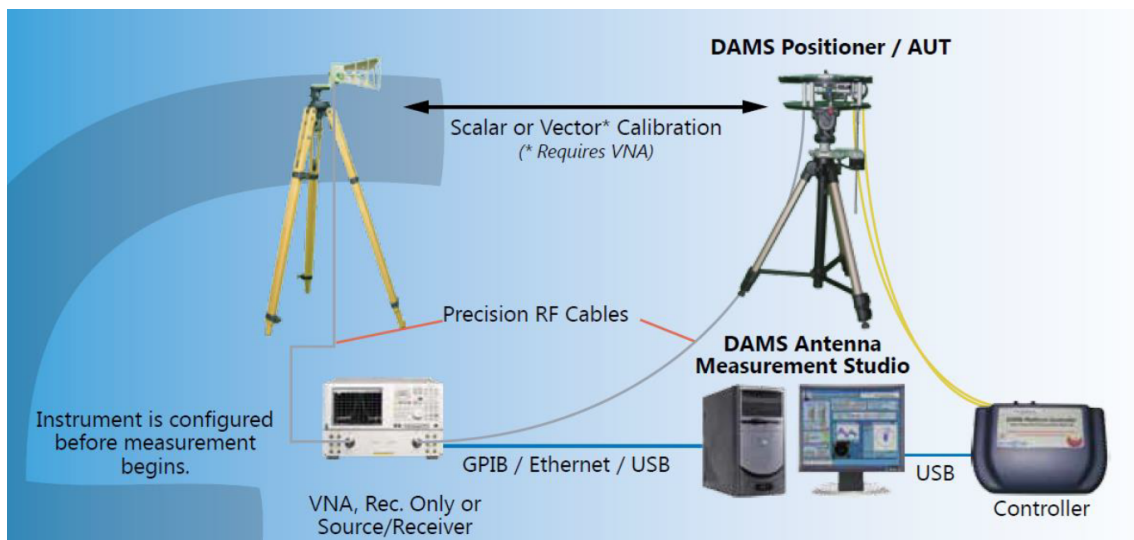
Figure 4.5. DAMS connection overview [62].
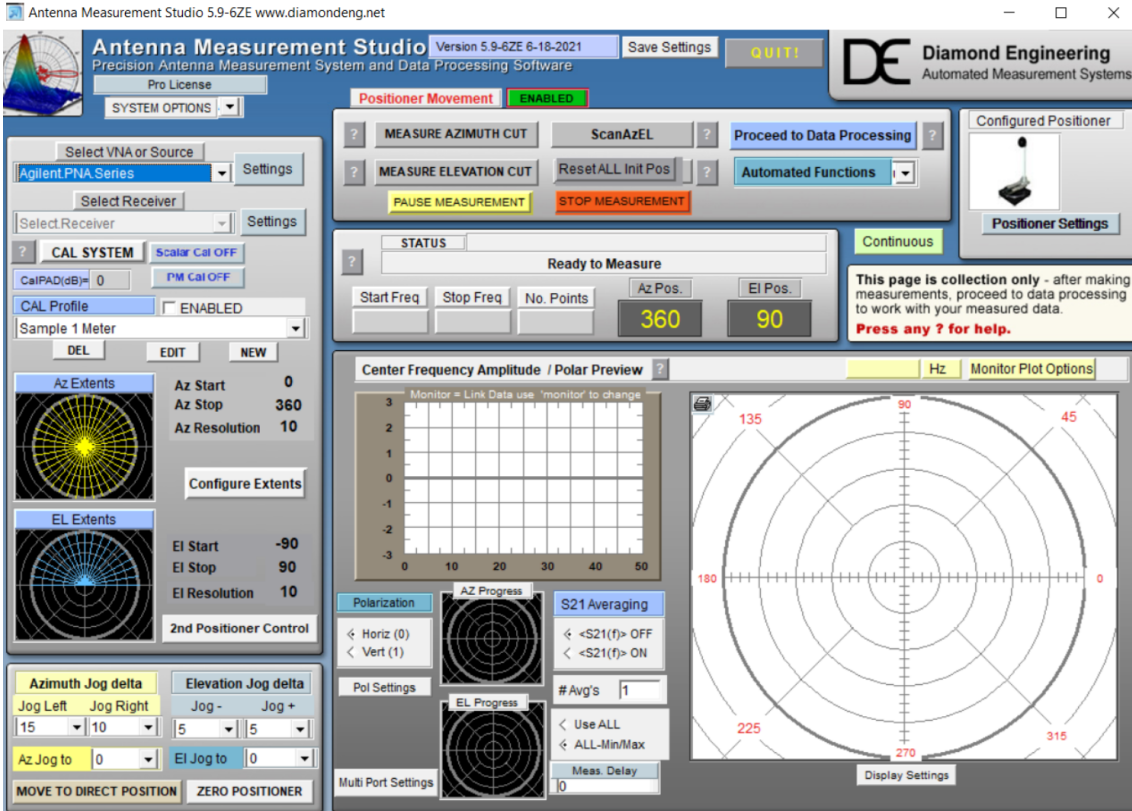
Figure 4.6. DAMS GUI.
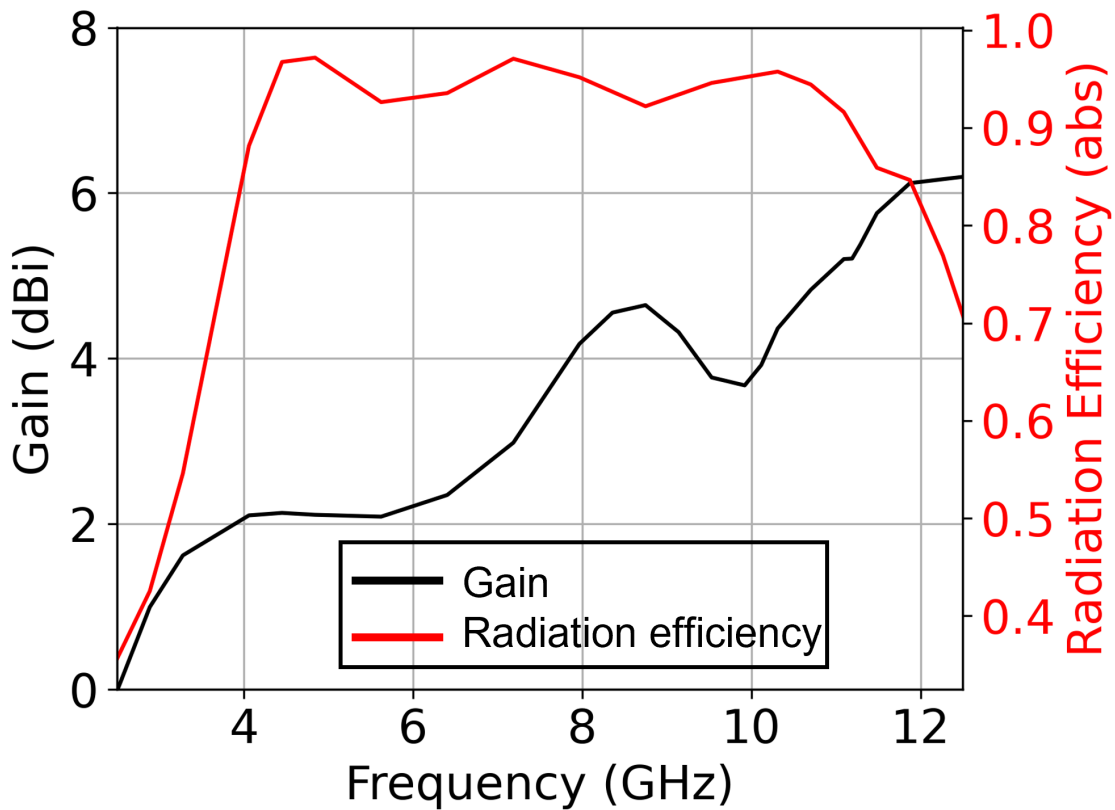
Figure 4.7. Simulated gain and radiation efficiency.
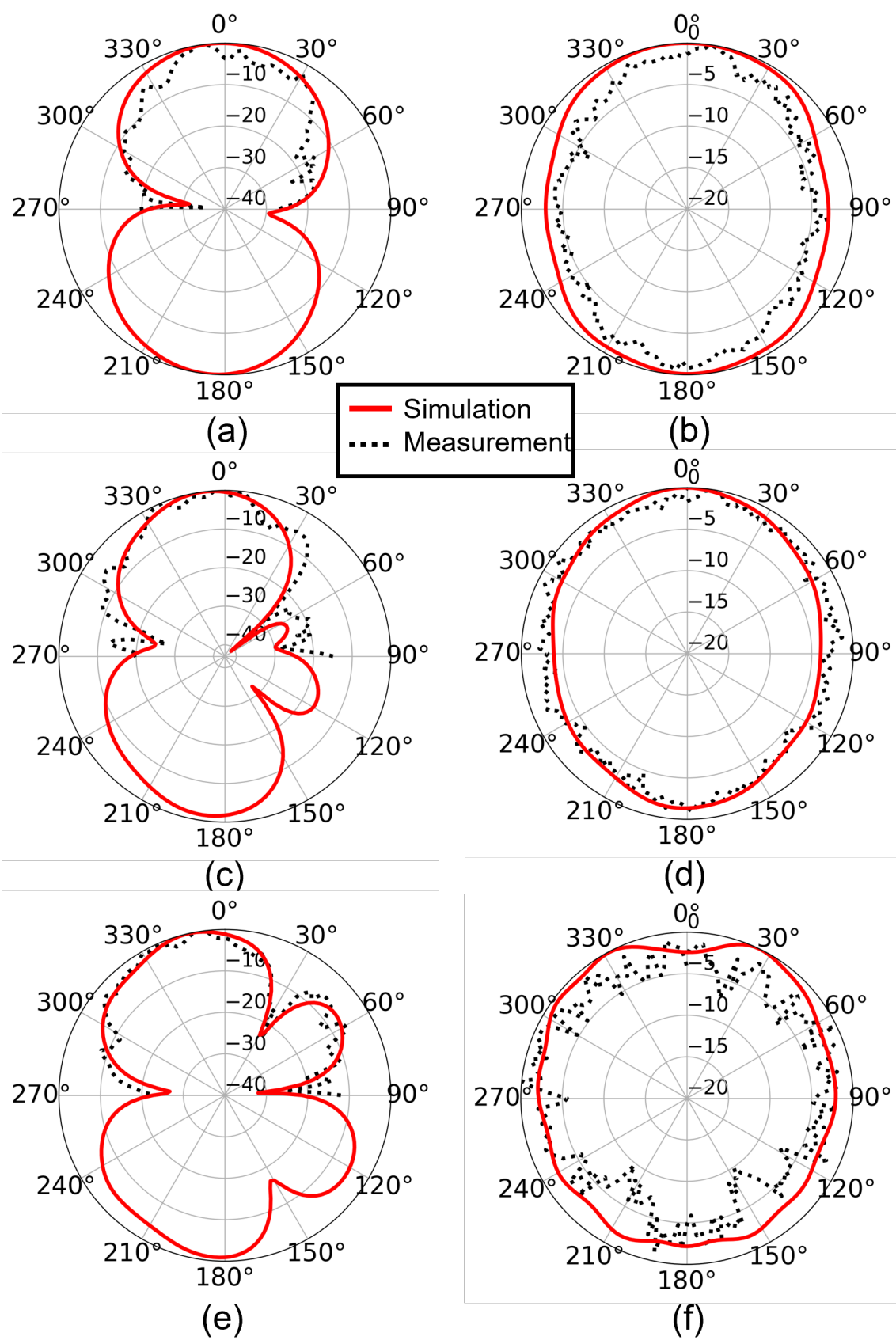
Figure 4.8. Normalized radiation pattern (simulation vs measurement) (a) E plane at 7.1 GHz (b) H plane 7.1 GHz (c) E plane at 8.75 GHz (d) H plane 8.75 GHz (e) E plane at 10 GHz (f) H plane 10 GHz.

4.1.3 Range Measurement

In order to perform sensing measurement of the fabricated UWB antenna, the distance between two UWB antennas (LoS) and distance measurement to the metal plate (NLoS) as an object is performed in this section. As mentioned in chapter 2, the power delay profile method is used here as a tool to measure the range, which is a popular technique for localization. The measurements were performed inside an anechoic chamber (under construction) at the Barkhausen Institut.

Measurement Setup (LoS Configuration):
The first measurement setup for measuring the distance between the two UWB antennas is shown in figure 4.9. In this setup, the fabricated UWB antennas are placed in the line of sight (LoS) configuration to measure the distance between the transmitter and receiver. The distance between them is set to 1 m, and height is maintained at 80 cm above the ground using tripods. Port 1 of the PNA is connected to one UWB antenna, and port 2 is connected to the other UWB antenna. The measured frequency range is set from 3.5
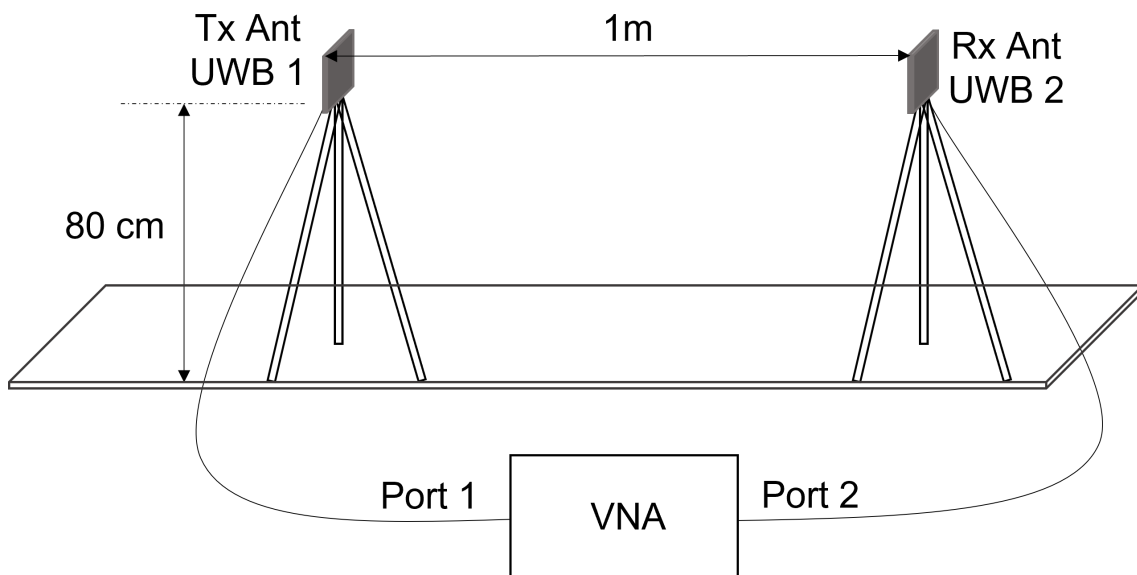
Figure 4.9. Line of Sight (LoS) measurement setup.

GHz to 12.5 GHz, corresponding to a delay resolution of 111 ps or 0.1 ns and power is set to 0 dBm. The spectrum is divided into 201 points. Therefore, the maximum excess delay or maximum measurable time-domain delay window is 2.22 ns. Usually, multiple measurements are performed at different locations for channel characterization or estimation. But, the experiment is performed only at one fixed distance as this work focuses on measuring the range between the transmitter and receiver using the power delay profile method. To compute the PDP, the channel impulse response in the time domain is obtained from the measured complex S_{21} data using the Inverse Fast Fourier Transform
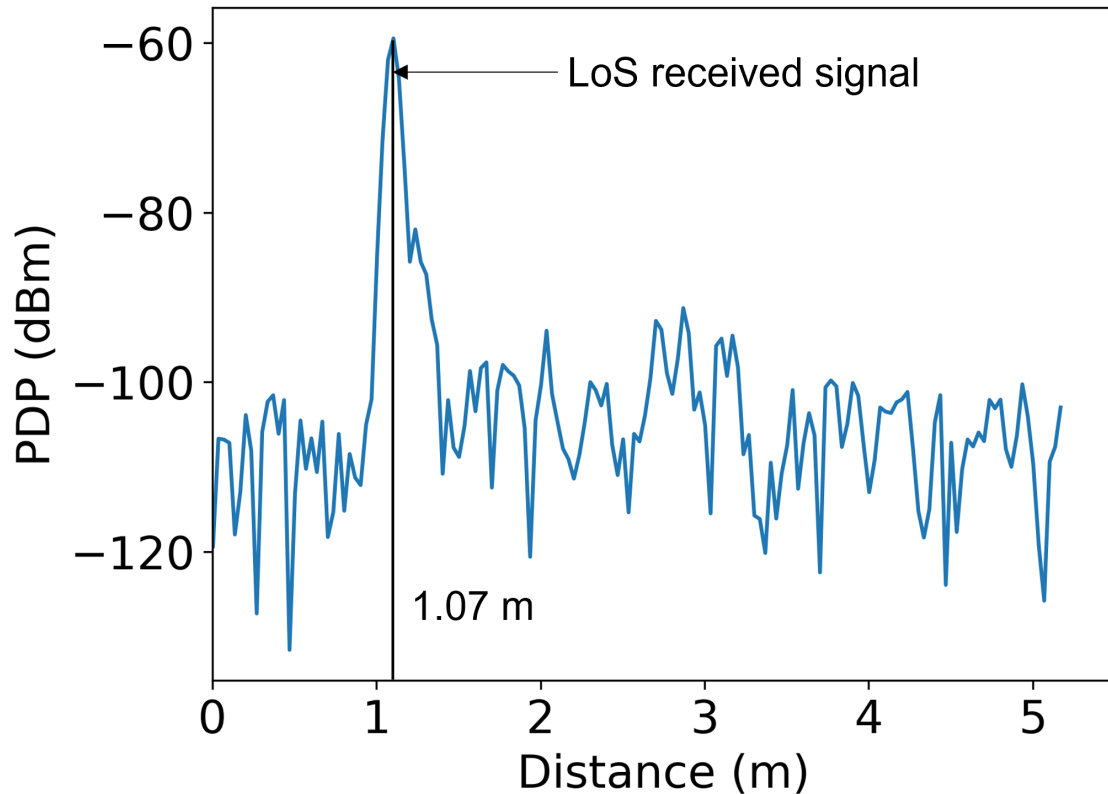
Figure 4.10. Line of Sight (LoS) range measurement between the transmitter and receiver.

(IFFT). After that, a Hamming window is applied at this stage to reduce the side lobe level in the delay domain. Finally, the horizontal delay axis is converted to the distance axis to show the range between the transmitter and receiver. Figure 4.10 shows that the peak received signal power is at 1.07 m, which is the distance between the antennas.

Metal Plate Distance Measurement Setup (NLoS Configuration):

Figure 4.11 shows the second measurement setup for measuring the distance of a metal plate (200 cm x 100 cm x 2 mm) where both UWB antennas are placed side by side in NLoS configuration. The distance between the antennas is 48 cm, and from the antenna's center point to the metal plate varies 1 m to 1.5 m during measurements 1 and 2. The antenna height is 80 cm above the ground using tripods and oriented towards the metal plate. Port 1 of the PNA is connected to one UWB antenna, and port 2 is connected to the other UWB antenna. To compute the PDP, similar procedures like LoS measurement were followed for this metal plate distance measurement. Figure 4.12 indicates that for each distance measurement, there is a common peak at 0.5 m which is the NLoS received signal from the Tx antenna due to the omnidirectional radiation behavior. The other peak is at 2.17 m and 3.17 m, which is the round trip distance reflected from the metal object presence in measurements 1 (1 m) and 2 (1.5 m), respectively, received by the receiver antenna. Therefore, any device equipped with a UWB antenna can provide information on the device's distance in a multipath environment.
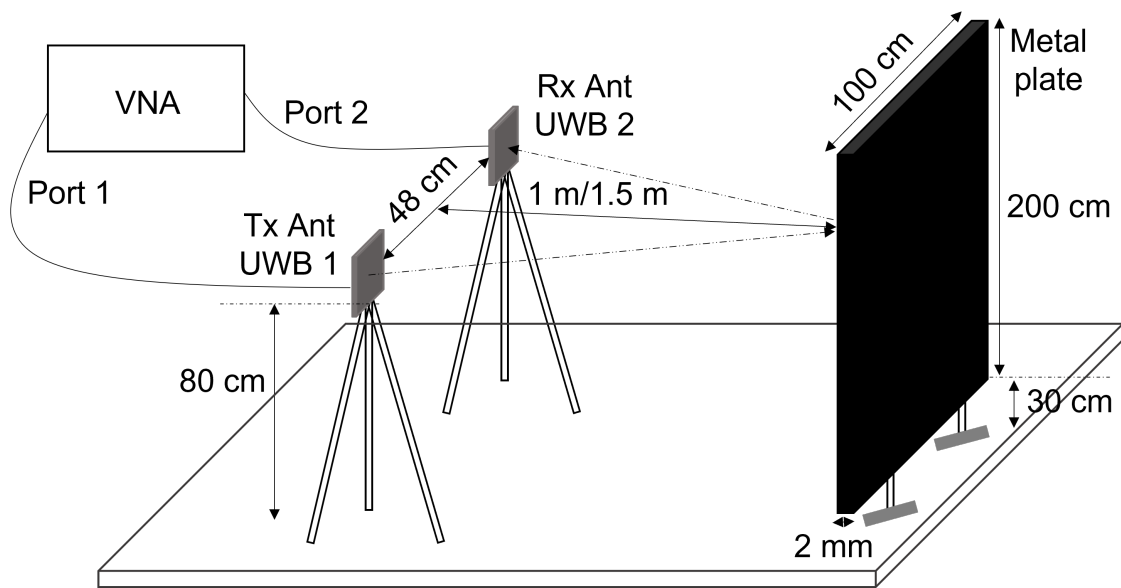
Figure 4.11. NLoS measurement setup for measuring the distance of metal plate.
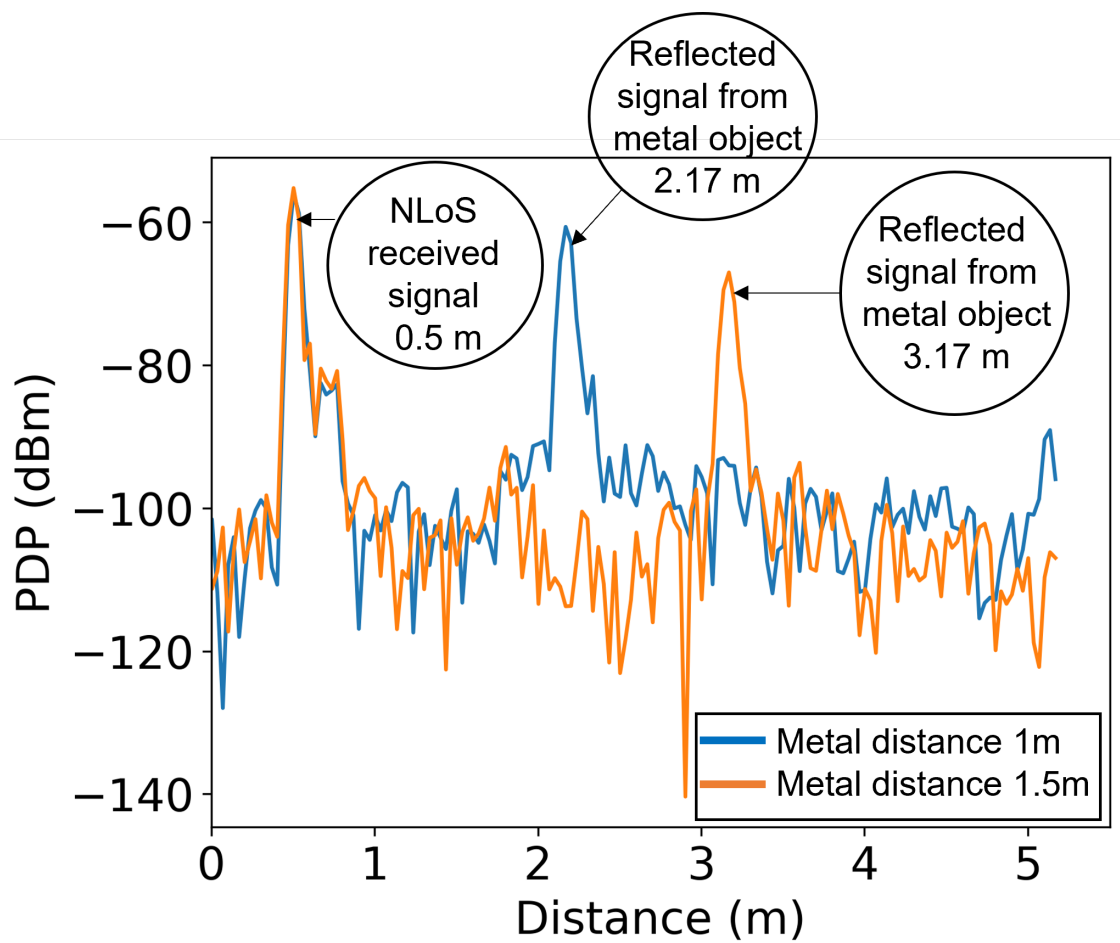
Figure 4.12. Metal object distance measurement using NLoS configuration.

4.1.4 Communication Experiment

In this section, a communication experiment is performed to validate the developed UWB antennas can successfully transmit the digitally modulated signal and receive them for demodulation and performance analysis across the 8+ GHz frequency range. The experiment is performed in a normal laboratory environment.

Measurement Setup:

To perform the experiment, Arbitrary Waveform Generator (AWG) is used to generate the modulated signal, and UXR0254AP 25 GHz 256 Gsa/s 10 bit Real-Time Oscilloscope perform the digital demodulation and performance analysis. QPSK and 16 QAM are chosen as digital modulation techniques for this communication experiment. Figure 4.13 shows the measurement setup. The Tx UWB antenna is connected with the AWG through
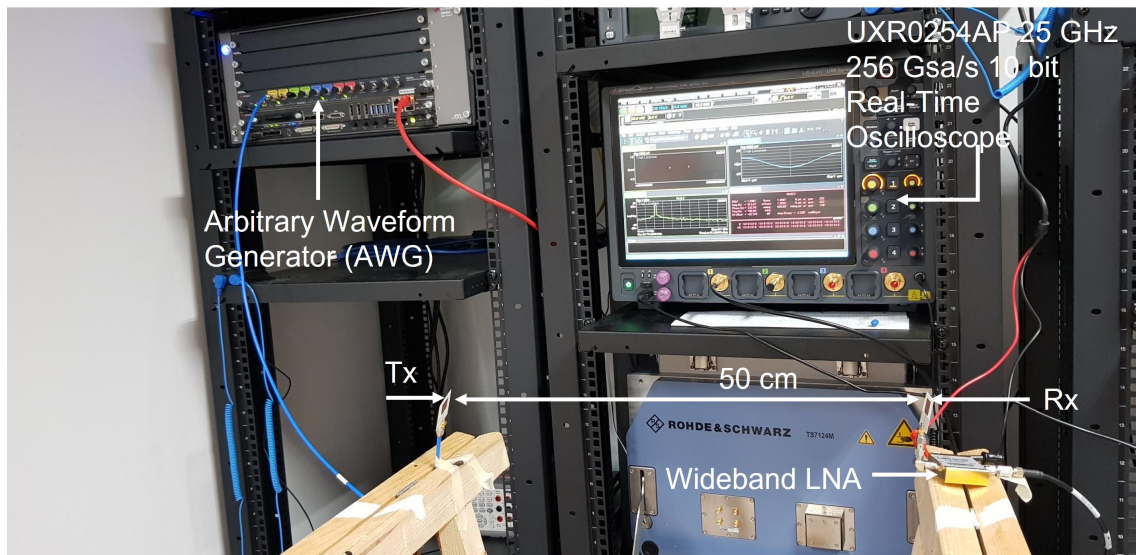
Figure 4.13. AWG-UXR communication measurement setup.

the coaxial cable, and the Rx UWB antenna is with channel 1 of the oscilloscope through the coaxial cable. The distance between the antennas is set to 50 cm. A wideband LNA is connected before the Rx antenna to facilitate the receiver measurement analysis, as the fabricated UWB antenna does not have a very high gain (4.6 dBi). The LNA has a gain of 26-33 dB for the frequency range of 2-20 GHz [63]. The transmitted power for the antenna is set to 0 dBm or 1 mW for this experiment. At first, the modulation techniques (QPSK and 16 QAM) are set up using the direct coaxial cables (directly connecting them) for the center frequency of 8 GHz and frequency span of 8.1 GHz, as shown in figure 4.14. In the next phase, over-the-air transmission is performed to compare the direct cable and over-the-air performance. The communication measurement results are validated by observing the constellation diagram, eye diagram, power spectral density and error vector magnitude (EVM) data.
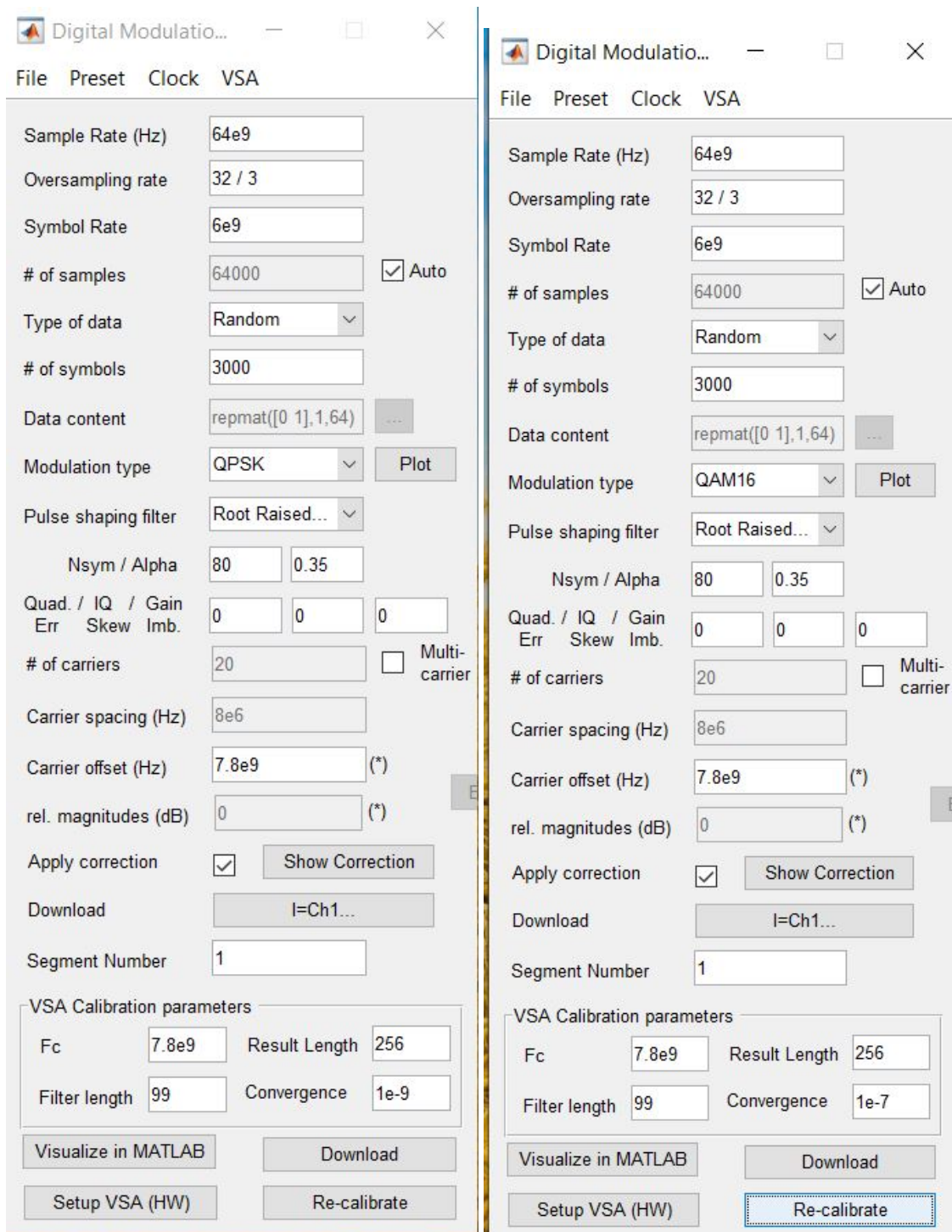
(a)   (b)

Figure 4.14. Modulation setup for direct cable transmission (a) QPSK (b) 16 QAM.

Measurement Results:

Figure 4.15a shows the QPSK for direct cable measurement and figure 4.15b for over-the-air measurement. The PSD plot in OTA measurement shows the received power by the
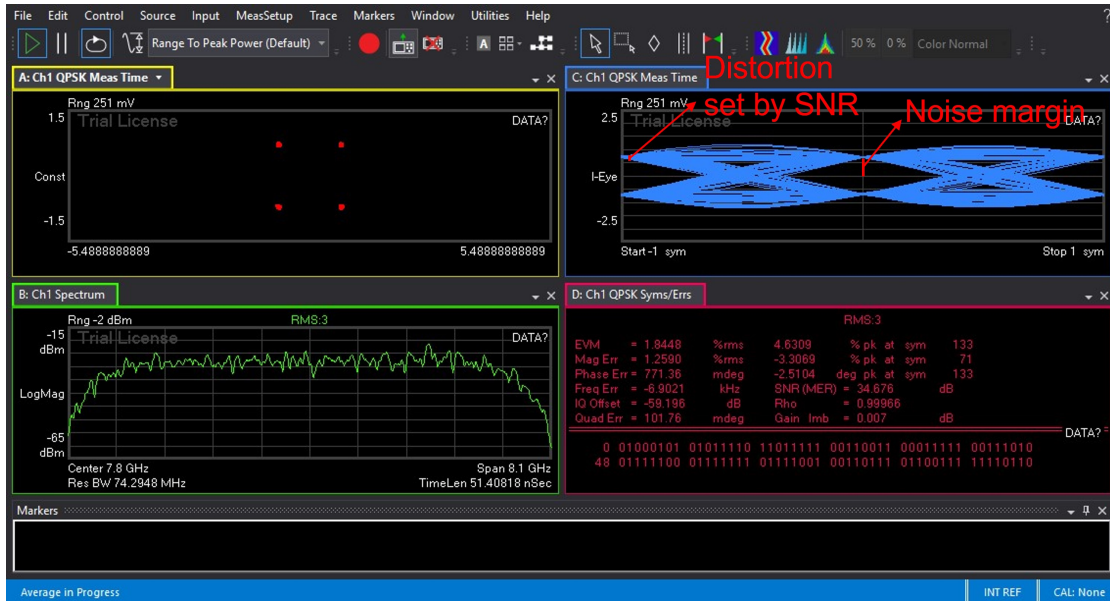
(a)
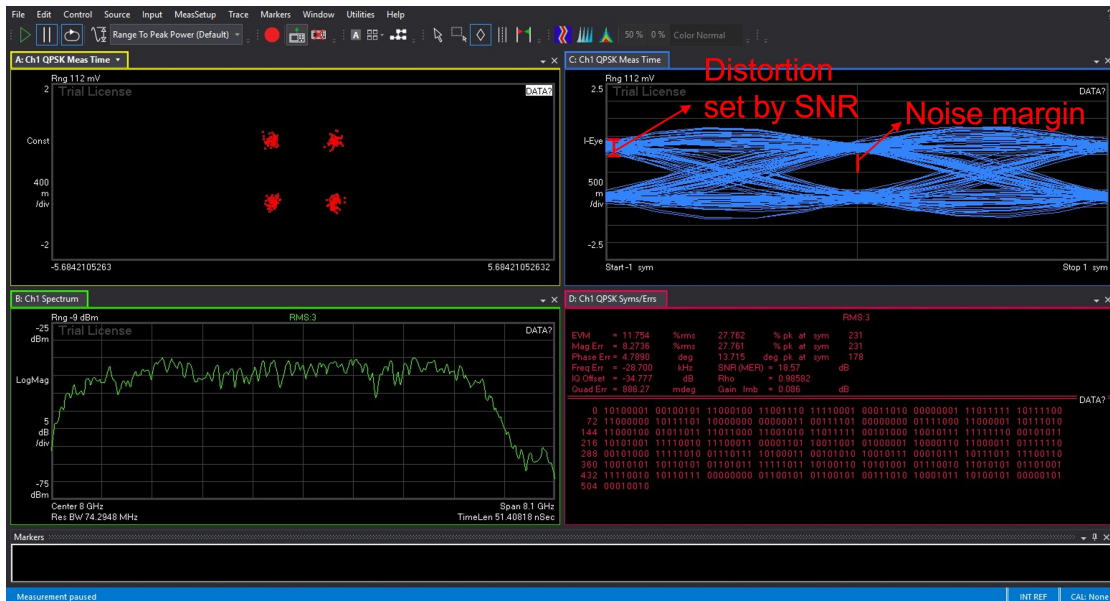
(b)

Figure 4.15. QPSK (a) Direct cable measurement (b) OTA measurement; Top left- Constellation diagram; Top right- Eye diagram; Bottom left- PSD; Bottom right- EVM data.

antenna is -35 dBm over the spectrum. It can be calculated approximately by modifying the Friis transmission equation in decibels as the measurement is performed in a laboratory where multipath propagation is unavoidable.

$$P_r = P_t + G_t + G_r - path\ loss + amplifier\ gain - cable\ loss \qquad (4.1)$$

Here, P_r: received power, P_t: transmitted power, G_t: transmitter antenna gain, G_r: receiver antenna gain, $path\ loss = 20\log(4\pi d/\lambda)$ [39].

The constellation diagram of figure 4.15b is more distorted than the figure 4.15a as the EVM > 2% RMS (11.75 % RMS). EVM is a measure of how far the received point or symbol is shifted from its ideal position due to various imperfections during transmission and reception. The difference in points can be due to magnitude error, meaning the received vector is too long or too short, and phase error, where the angle of the received vector is incorrect. But EVM often does not offer much insight into the nature of the error. On the other hand, a constellation diagram helps determine the cause(s) of deviations from the ideal point. By visualizing the constellation diagram of figure 4.15b, the received points are seen to be more spread out around the ideal points, which is due to the noise. It happens when the SNR value is low, and the SNR value of 18.57 dB compared to 34.6 dB of figure 4.15a confirms the statement. In addition to that, an eye diagram provides a useful analysis of the digital transmission system. It is a frozen display of the digital received signal, which is repetitively sampled. By visualizing the eye diagram of figure 4.15b, the noise margin is seen to be smaller than the figure 4.15a. It is the amount of noise that can be tolerated by the signal and tells us how far one can go before running into the decision error, and usually, the larger, the better it is. The distortion indicated in the eye diagrams of figure 4.15 also confirms the low SNR value for figure 4.15b.

Similarly, figure 4.16a shows the 16 QAM for direct cable measurement and figure 4.16b for over-the-air measurement. As the modulation order increases, the EVM value should increase also. But the EVM data in the bottom right corner of figure 4.16b shows that it is 9.6 % RMS, and the SNR is slightly better (17.84 dB) than the QPSK OTA measurement. This could be due to less external interference during the 16 QAM measurement. The constellation diagram of figure 4.16b is more distorted than figure 4.16a, and by zooming on each constellation point, it is summarised that due to noise and hence low SNR, the received points are spread out around the ideal point. From the eye diagram comparison between the measurements, the noise margin is smaller in figure 4.16b compared to figure 4.16a. Hence, the eye becomes much smaller in figure 4.16b. These OTA measurement results are acceptable for UWB communication as the frequency span here is very large, and the energy is distributed over this large spectrum. With these QPSK and 16 QAM measurements, the usability of this UWB antenna across the 8+ GHz frequency range is validated.
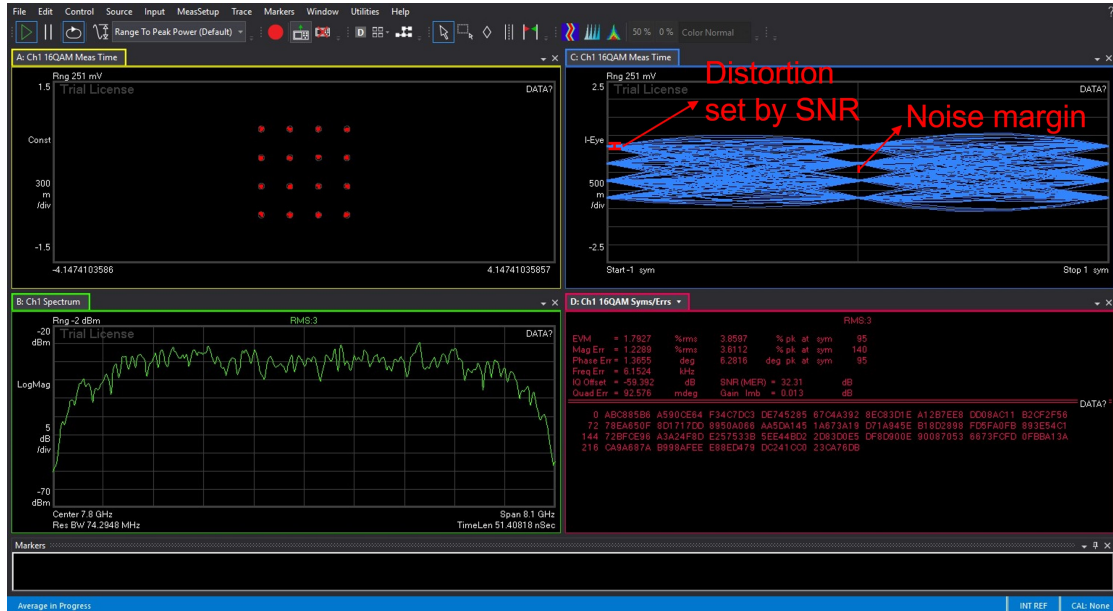
(a)
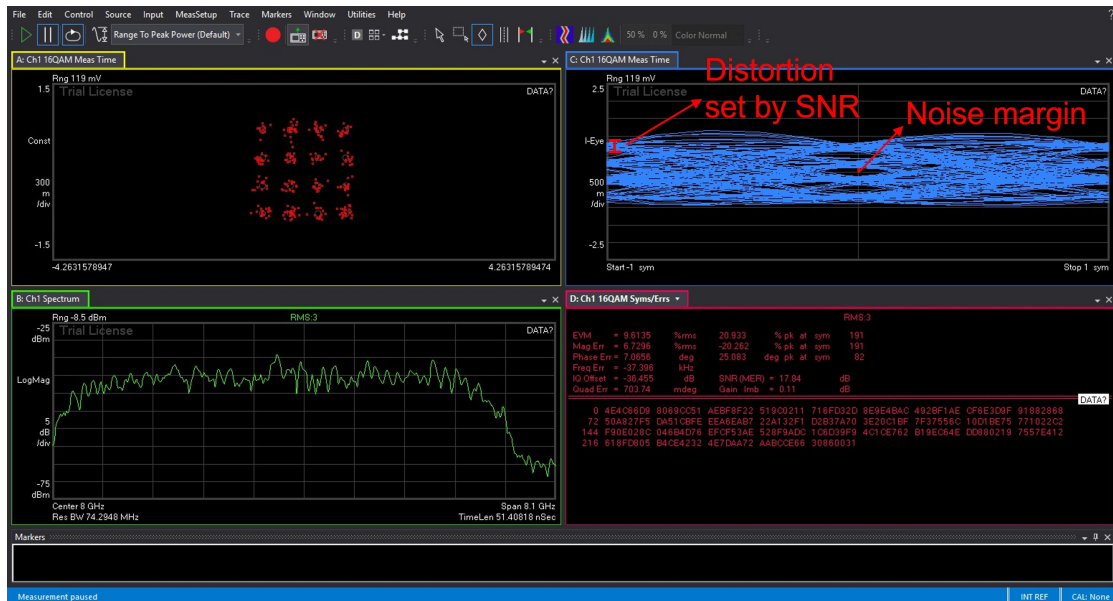
(b)

Figure 4.16. 16 QAM (a) Direct cable measurement (b) OTA measurement; Top left-Constellation diagram; Top right- Eye diagram; Bottom left- PSD; Bottom right- EVM data

4.2   Wideband Antenna (5.9-7.1 GHz)

The proposed wideband antenna-4 is fabricated using the LPKF ProtoMat machine avail-
able in Barkhausen Institut. The fabrication procedures are similar to the previous UWB
antenna fabrication. Photographs of the fabricated wideband antenna prototype is shown
in figure 4.18. The PNA and DAMS positioner are used for further measurements.
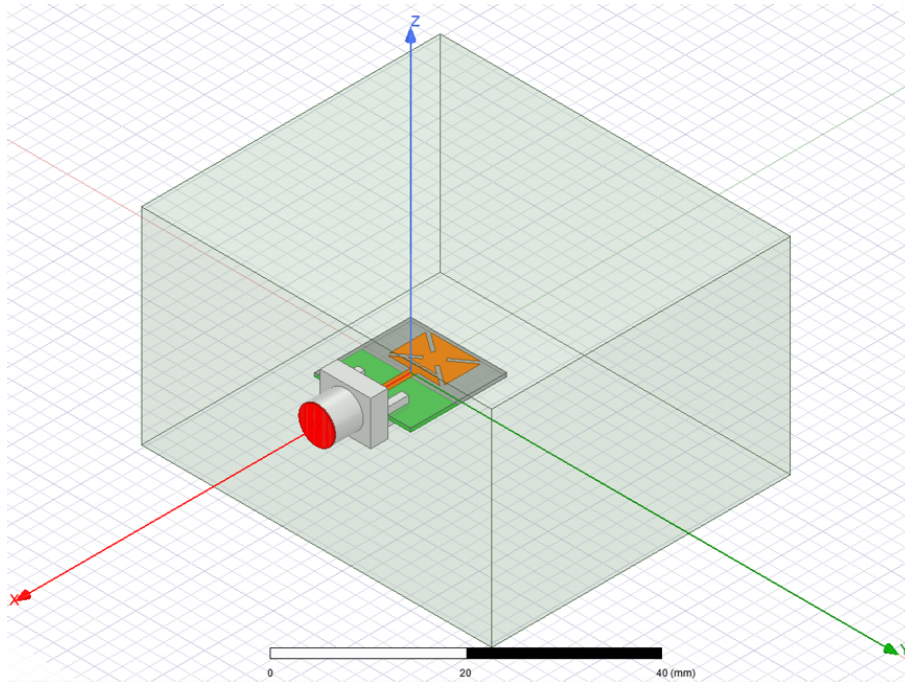
Figure 4.17. Final wideband antenna-4 model in HFSS.

Top view   Bottom view
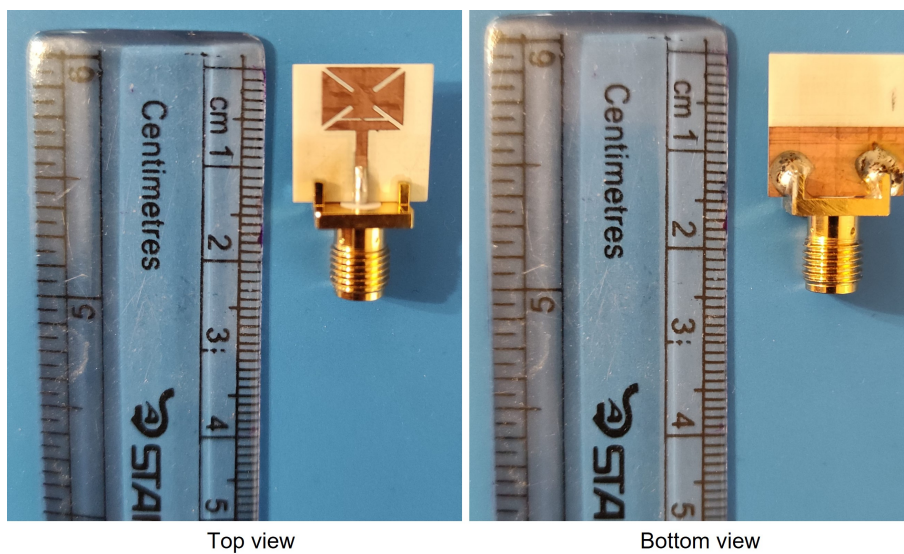
Figure 4.18. Fabricated wideband antenna-4 left (Top view) right (Bottom view).

4.2.1 Return Loss Measurement

At first, the required frequency range (5-8 GHz) and transmitted power of 0 dBm are selected in the PNA. Then, The PNA is calibrated using the Smart Cal calibration tool provided with the PNA. After the calibration, the fabricated wideband antenna-4 is connected to port 1 of the PNA for S_{11} measurement. The measurement is performed in a normal laboratory environment. Figure 4.19 shows the comparison of S_{11} between the simulated and fabricated antenna. The S_{11} of the fabricated wideband antenna shows impedance
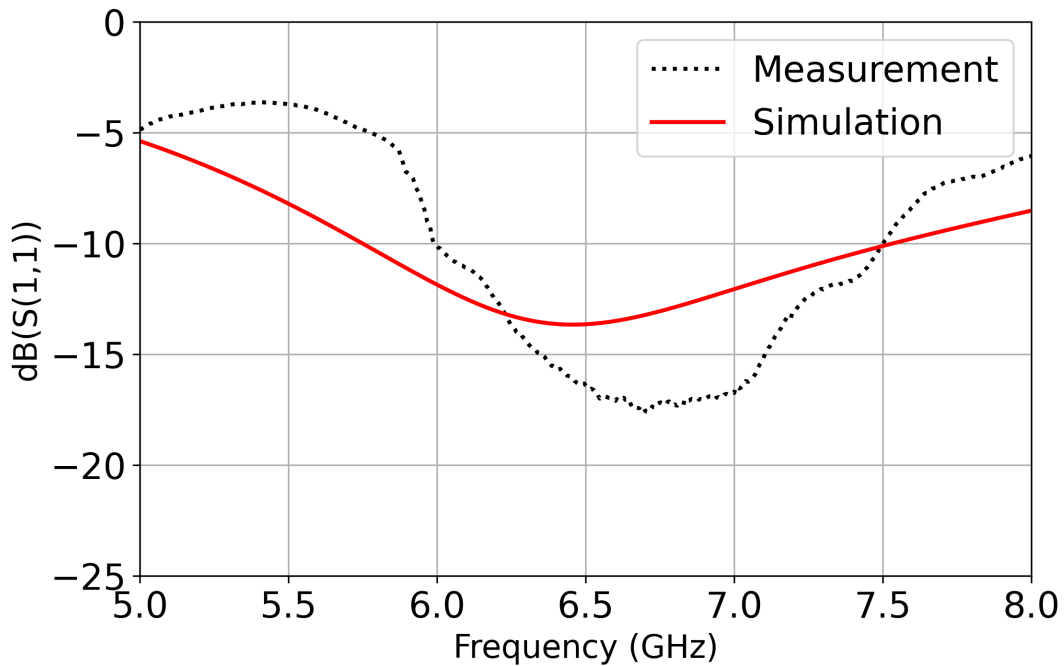
Figure 4.19. S_{11} of fabricated WB antenna-4 (simulation vs measurement).

BW of 1.52 GHz (5.98-7.5 GHz), whereas, from the simulation, it is 1.71 GHz (5.74-7.45 GHz). The factors contributing to mismatches are expected to be from:

- SMA connector.
- LPKF fabrication tolerance as the gap between two horizontal slots is very narrow (0.2 mm in the current model).

To validate the above first statement, the WB antenna is again simulated without the SMA connector to see the influence of the connector. A rectangular wave port (11.4 mm x 3 mm) is used to feed the antenna feed line directly, and the 50 Ω port size is calculate from the HFSS document [64]. Figure 4.20 compares the measured result with the simulation of the antenna with an SMA connector and without an SMA connector (direct wave port feeding). Here, the impedance matching for the simulation with the SMA connector is reduced, and the simulation with the wave port matches more with the measurement result.
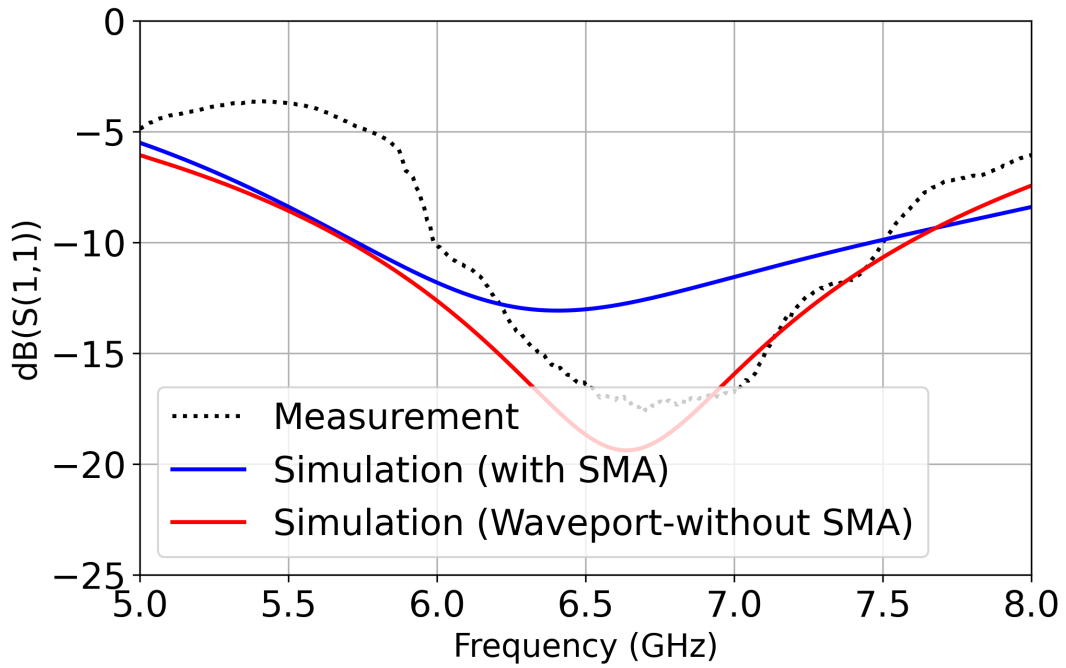
Figure 4.20. S_{11} comparison of the WB antenna-4 measurement result with simulation (with SMA and without SMA (direct wave port feeding).
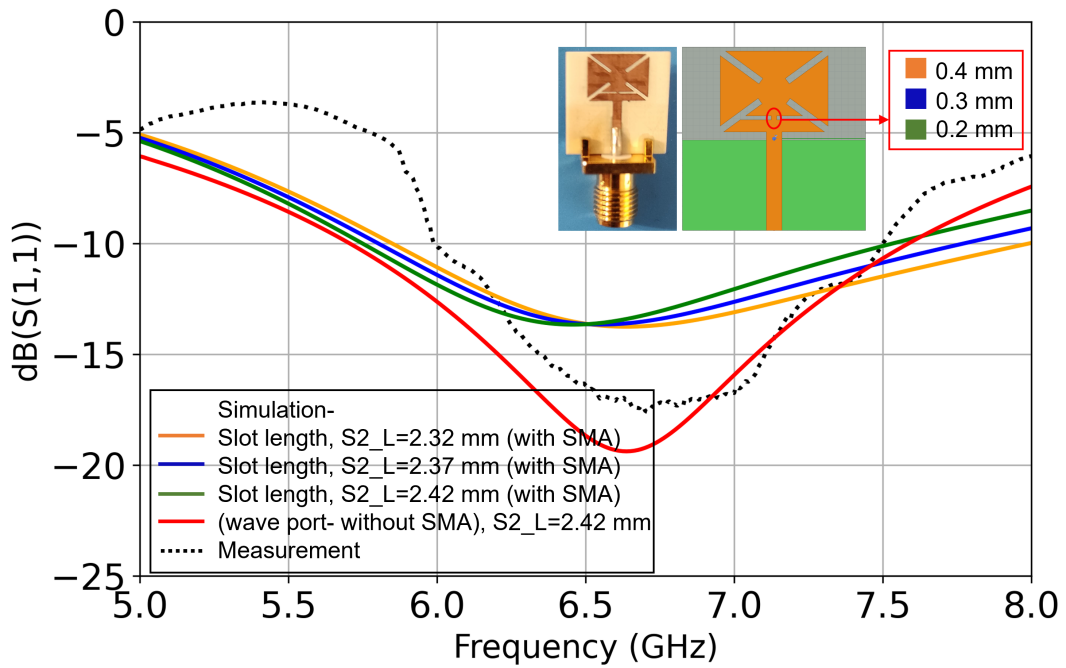
Figure 4.21. Horizontal slot length parametric analysis for understanding the LPKF fabrication tolerance.

For the second statement, the horizontal slot length of the WB antenna is varied by 0.05 mm. The current fabricated WB antenna has a gap of 0.2 mm between two horizontal slots, which is very close to the LPKF fabrication resolution. Figure 4.21 shows that with the reducing length of the horizontal slot, the gap increases between the slots and the resonant frequency shifts toward the measurement result. The S_{11} parameter for measurement is -17 dB at 6.7 GHz, which is in between the simulation with SMA and wave port simulation.

4.2.2 Gain Measurement

Similar to the previous UWB gain measurement experiment, the DAMS positioner is used for this WB antenna E-plane and H-plane. The measurements were conducted in an anechoic chamber (under construction) as shown in figure 4.22. After completing the calibration of the PNA using long coaxial cables, port 1 is connected to the DUT antenna, and port 2 to the reference horn antenna. The positioner rotates the DUT antenna 180 degrees for the E-plane (due to hardware issue) and completes 360 degrees for the H-plane measurement.
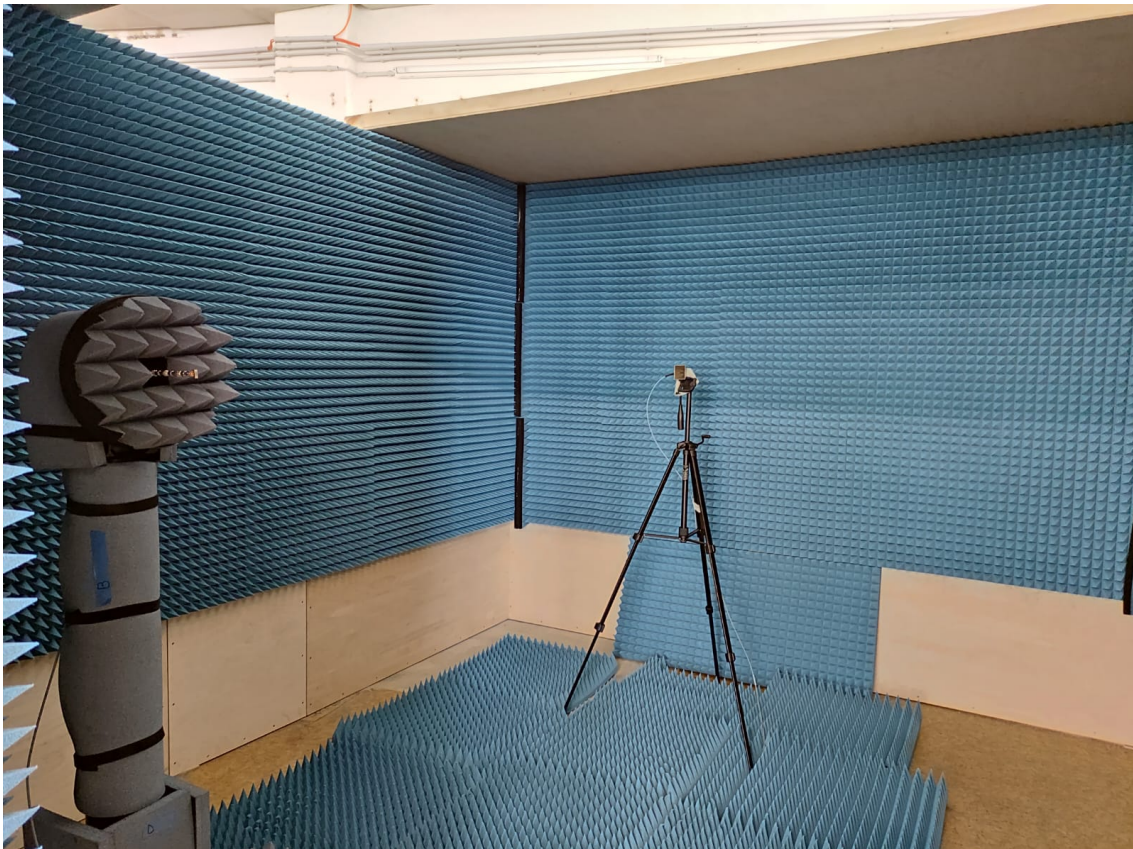
Figure 4.22. Proposed WB antenna radiation pattern measurement in an anechoic chamber (under construction).

Figure 4.23 presents the wideband antenna radiation pattern E-plane (XZ direction) and
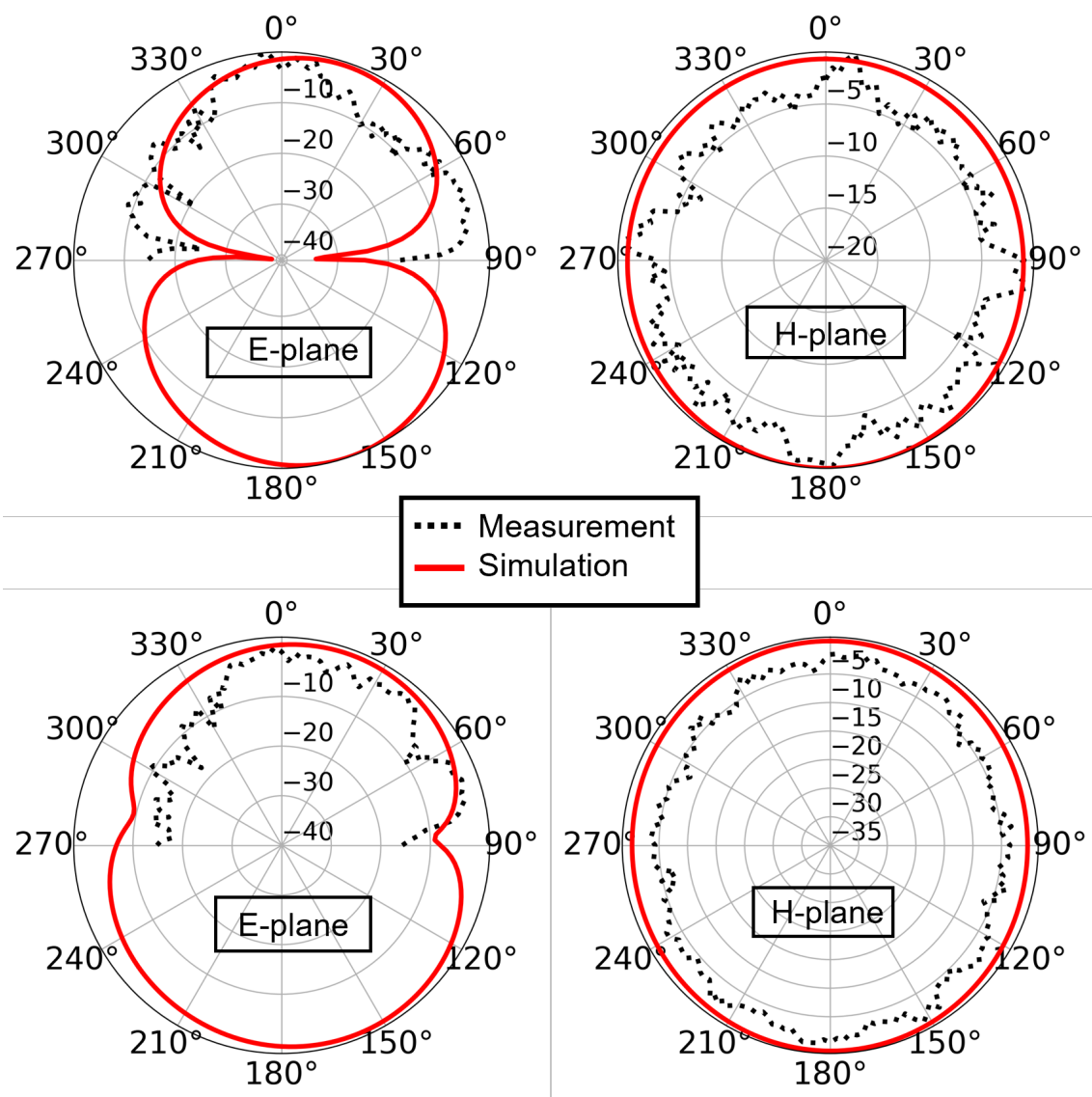
Figure 4.23. Wideband antenna-4 normalized radiation pattern (a) E-plane at 6.25 GHz (b) H-plane 6.25 GHz (c) E-plane at 7.5 GHz (d) H-plane 7.5 GHz.

H-plane (YZ direction) at 6.25 and 7.5 GHz. The results exhibit omnidirectional behaviour in the wide frequency range. The mismatches occurring at certain angles are from open ceiling and uncovered side walls (lower area) as there are no absorbers.

The gain and radiation efficiency of the proposed wideband antenna-4 are shown in figure 4.24. At 6.8 GHz, the fabricated antenna has a peak gain of 2.2 dBi, and with increasing frequency, the gain is also increasing. The gain is acceptable with this compact size as the antenna exhibits an omnidirectional pattern.
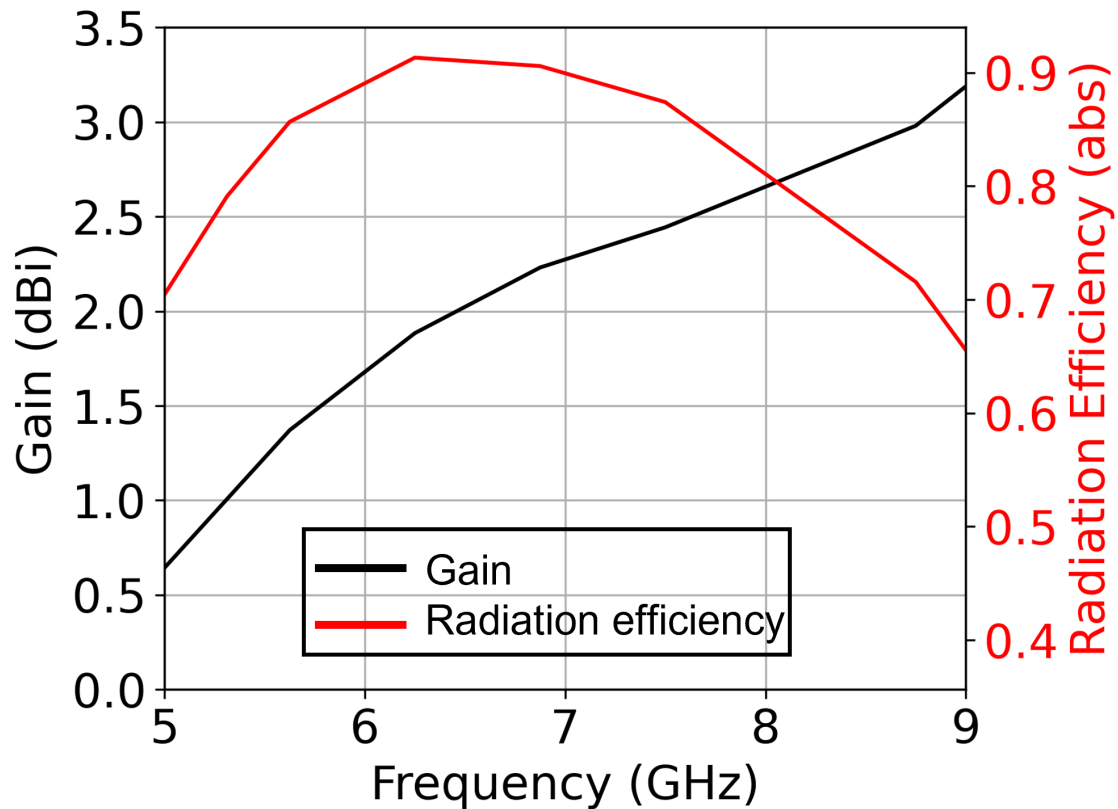
Figure 4.24. Simulated gain and radiation efficiency of the proposed wideband antenna-4.

The radiation efficiency is close to 90% at our desired frequency range (5.9-7.1 GHz) which is very high. While compacting, small antennas suffer from low radiation efficiency (around 50%) when slots are cut like meandered lines (normal to the current distribution) that completely bend the current in the patch [65, 66]. In this WB antenna design, meandered line-like slots are avoided to maintain high radiation efficiency while compacting the antenna.

Conclusion

This master thesis work studies the development of wideband compact antennas targeting two new futuristic trends in wireless technology: joint communication and sensing (JC&S) in 6G and IEEE 802.11 bf (Wi-Fi sensing). From the antenna design point of view, the wide bandwidth and compact physical structure with good gain and high radiation efficiency are the first steps toward achieving these new technologies.

Therefore, this thesis work designed and fabricated two wideband compact antennas based on their fractional bandwidth for communication and sensing applications. One UWB antenna focusing on UWB application and one wideband antenna focusing on Wi-Fi sensing application are designed and fabricated. Both fabricated antennas fulfil the compactness requirement of the thesis. The UWB antenna dimension is 31.5 mm x 33.5 mm (0.8 λ_0 x 0.85 λ_0), and the WB antenna is 14 mm x 14 mm (0.3 λ_0 x 0.3 λ_0). Defected ground structure technique is used to increase the impedance BW of the UWB antenna, whereas the slot-loading technique is followed for the WB antenna. Both methods use current distribution analysis and provide increased impedance BW and compactness. The UWB antenna shows an impedance BW of 7.9 GHz, and for the WB antenna, it is 1.9 GHz. The peak gain is 4.6 dBi and 2.2 dBi around the UWB and WB antenna's centre frequency, respectively. The gain measurement is conducted using a positioner in an under constructed anechoic chamber. Therefore, the simulation and measurement results have slight mismatches. The radiation efficiency in both developed antennas is close to 90%. The radiation efficiency for the WB antenna is achieved by avoiding the zigzag pattern slot (meandered line) in the patch, as cutting the slot in the patch worsens the radiation efficiency.

Additionally, an equivalent circuit model is provided for the UWB antenna. The Foster first canonical form is used to model the equivalent circuit using lumped elements. This equivalent circuit provides insight into the theoretical analysis of the designed UWB antenna.

Finally, the fabricated UWB antenna is used to perform sensing and communication experiments. For the sensing experiment, the range between the two UWB antennas (LoS configuration) and metal object distance measurement (NLoS configuration) is performed using the power delay profile as a tool.

For communication measurement using UWB antenna, AWG-UXR equipped measurement is performed where the modulated signal is generated using AWG, and digital demodulation

and performance analysis is done in the UXR oscilloscope. The RF signal's performance of the Rx UWB antenna is analysed by observing the constellation diagram, eye diagram, PSD and EVM data. Here, QPSK and 16 QAM are used for digital modulation. The usability of this UWB antenna across the 8+ GHz frequency range is validated with this measurement.

In addition to the conclusions, further research corresponding to this study can be continued by improving the gain and compactness using a metamaterial-based design. A comparison of enhanced gain can also be analysed between the array structure and metamaterial-based structure.

References

[1] Shannon CE. "Communication in the presence of noise". In: *Proceedings of the IRE* 37.1 (1949), pp. 10–21.

[2] Rao S. *Introduction to mmwave Sensing: FMCW Radars (Texas Instruments)*. `https://training.ti.com/sites/default/files/docs/mmwaveSensing-FMCW-offlineviewing_0.pdf`. Accessed: 2022-06-12.

[3] Federal Communications Commission. "First Report and Order: Revision of Part 15 of the Commission's Rule Regarding Ultra-Wideband Transmission System FCC 02-48." In: *ET Docket 98-153* (2002).

[4] Nikolaou S and Abbasi MA. "Design and development of a compact UWB monopole antenna with easily-controllable return loss". In: *IEEE Transactions on Antennas and Propagation* 65.4 (2017), pp. 2063–2067.

[5] Nikolaou S and Abbasi MA. "Miniaturization of UWB antennas on organic material". In: *International Journal of Antennas and Propagation* 2016 (2016).

[6] Shostko IS and Almakadma T. "Proposals to build a promising ultra-wideband wireless communications". In: *2010 5th International Confernce on Ultrawideband and Ultrashort Impulse Signals*. IEEE. 2010, pp. 162–164.

[7] Nikolaou S and Quddious A. "Antennas for UWB Applications". In: *UWB Technology-Circuits and Systems*. IntechOpen, 2019.

[8] Boopathi RR and Pandey SK. "Metamaterial-inspired printed UWB antenna for short range RADAR applications". In: *Microwave and Optical Technology Letters* 59.7 (2017), pp. 1600–1604.

[9] Jacob N and Kulkarni M. "An electronically switchable UWB to narrow band antenna for cognitive radio applications". In: *Microwave and Optical Technology Letters* 62.9 (2020), pp. 2989–3001.

[10] Gayatri T et al. "Design Analysis of a Luna Shaped UWB Antenna for Spectrum Sensing in 3.1-10.6 GHz". In: *2020 IEEE 17th India Council International Conference (INDICON)*. IEEE. 2020, pp. 1–5.

[11] Shao W et al. "A time-domain measurement system for UWB microwave imaging". In: *IEEE Transactions on Microwave Theory and Techniques* 66.5 (2018), pp. 2265–2275.

[12] Afyf A and Bellarbi L. "A novel miniaturized UWB antenna for microwave imaging". In: *2014 International Conference on Multimedia Computing and Systems (ICMCS)*. IEEE. 2014, pp. 1475–1478.

[13] Wild T, Braun V, and Viswanathan H. "Joint design of communication and sensing for beyond 5G and 6G systems". In: *IEEE Access* 9 (2021), pp. 30845–30857.

[14] *Digital Key Release 3.0 specification.* `https://carconnectivity.org/ press - release / car - connectivity - consortium - delivers - digital-key-release-3-0-specification/`. Accessed: 2022-06-01.

[15] *How UWB Expands Into the IoT - Where We Stand Today (Presence Detection and Follow-Me).* `https://www.nxp.com/company/blog/how-uwb- expands - into - the - iot - where - we - stand - today : BL - UWB - EXPANDS-INTO-IOT`. Accessed: 2022-06-01.

[16] Cordeiro C. *Next-generation Wi-Fi: Wi-Fi 7 and beyond.* `https://www.intel. com/content/dam/www/public/us/en/documents/pdf/wi-fi-7- and-beyond.pdf`. Accessed: 2022-06-01.

[17] Fettweis G et al. "Joint Communications & Sensing: Common Radio-Communications and sensor technology". In: *VDE ITG* (2021), p. 24.

[18] Restuccia F. "IEEE 802.11 bf: Toward ubiquitous Wi-Fi sensing". In: *arXiv preprint arXiv:2103.14918* (2021).

[19] Balanis CA. *Antenna theory: analysis and design.* John wiley & sons, 2015.

[20] Kumar G and Ray KP. *Broadband microstrip antennas.* Artech house, 2003.

[21] Carver K and Mink J. "Microstrip antenna technology". In: *IEEE transactions on antennas and propagation* 29.1 (1981), pp. 2–24.

[22] Richards W, Lo Y, and Harrison D. "An improved theory for microstrip antennas and applications". In: *IEEE Transactions on antennas and propagation* 29.1 (1981), pp. 38–46.

[23] Bailey M and Deshpande M. "Integral equation formulation of microstrip antennas". In: *IEEE Transactions on Antennas and Propagation* 30.4 (1982), pp. 651–656.

[24] Skolnik MI. "Radar handbook". In: (1970).

[25] Pozar DM and Schaubert DH. "The analysis and design of microstrip antennas and arrays". In: *A Selected Reprint Volume. IEEE Antennas and Propagation Society Sponsor. New York* (1995).

[26] Subrahmanya VL. "Pattern Analysis of "The Rectangular Microstrip Patch Antenna"". In: *University College of Boras* (2009).

[27] Bahl IJ. and Bhartia P. *Microstrip Antennas. Dedham, MA. Artech House.* 1980.

[28] Bahl IJ. "A designer's guide to microstrip line". In: *Microwaves* (1977), pp. 1–380.

[29] Pozar DM. "Microstrip antennas". In: *Proceedings of the IEEE* 80.1 (1992), pp. 79–91.

[30] Wood C. "Improved bandwidth of microstrip antennas using parasitic elements". In: *IEE Proceedings H-Microwaves, Optics and Antennas*. Vol. 127. 4. IET. 1980, pp. 231–234.

[31] Kumar G and Gupta KC. "Broad-band microstrip antennas using additional resonators gap-coupled to the radiating edges". In: *IEEE Transactions on Antennas and Propagation* 32.12 (1984), pp. 1375–1379.

[32] Kumar G and Gupta KC. "Directly coupled multiple resonator wide-band microstrip antennas". In: *IEEE Transactions on Antennas and Propagation* 33.6 (1985), pp. 588–593.

[33] Pedra AC et al. "Shorting pins application in wide-band E-shaped patch antenna". In: *2009 SBMO/IEEE MTT-S International Microwave and Optoelectronics Conference (IMOC)*. IEEE. 2009, pp. 229–234.

[34] *Planar Inverted F Antenna (PIFA)*. `https://www.antenna-theory.com/antennas/patches/pifa.php`. Accessed: 2022-05-14.

[35] Chattha HT et al. "Bandwidth enhancement techniques for planar inverted-F antenna". In: *IET microwaves, antennas & propagation* 5.15 (2011), pp. 1872–1879.

[36] Ollikainen J, Fischer M, and Vainikainen P. "Thin dual-resonant stacked shorted patch antenna for mobile communications". In: *Electronics letters* 35.6 (1999), pp. 437–438.

[37] Gomez-Villanueva R et al. "Ultra-wideband planar inverted-F antenna (PIFA) for mobile phone frequencies and ultra-wideband applications". In: *Progress In Electromagnetics Research C* 43 (2013), pp. 109–120.

[38] Chiou T and Wong K. "Designs of compact microstrip antennas with a slotted ground plane". In: *IEEE Antennas and Propagation Society International Symposium. 2001 Digest. Held in conjunction with: USNC/URSI National Radio Science Meeting (Cat. No. 01CH37229)*. Vol. 2. IEEE. 2001, pp. 732–735.

[39] Pozar DM. *Microwave engineering*. John wiley & sons, 2011.

[40] Garg R et al. *Microstrip antenna design handbook*. Artech house, 2001.

[41] Siakavara K. "Methods to design microstrip antennas for modern applications". In: *Microstrip antennas* (2011), pp. 173–236.

[42] Sayidmarie KH and Yahya LS. "Modeling of dual-band crescent-shape monopole antenna for WLAN applications". In: *International Journal of Electromagnetics and Applications* 4.2 (2014), pp. 31–39.

[43] Wang SB, Niknejad AM, and Brodersen RW. "Circuit modeling methodology for UWB omnidirectional small antennas". In: *IEEE Journal on Selected Areas in Communications* 24.4 (2006), pp. 871–877.

[44] Ansarizadeh M, Ghorbani A, and Abd-Alhameed RA. "An approach to equivalent circuit modeling of rectangular microstrip antennas". In: *Progress In Electromagnetics Research B* 8 (2008), pp. 77–86.

[45] Caratelli D et al. "Circuit model and near-field behavior of a novel patch antenna for WWLAN applications". In: *Microwave and Optical Technology Letters* 49.1 (2007), pp. 97–100.

[46] *Power Delay Profile*. `https://www.gaussianwaves.com/2014/07/power-delay-profile/`. Accessed: 2022-06-18.

[47] Bahl P and Padmanabhan VN. "RADAR: An in-building RF-based user location and tracking system". In: *Proceedings IEEE INFOCOM 2000. Conference on computer communications. Nineteenth annual joint conference of the IEEE computer and communications societies (Cat. No. 00CH37064)*. Vol. 2. Ieee. 2000, pp. 775–784.

[48] Wu K et al. "FILA: Fine-grained indoor localization". In: *2012 Proceedings IEEE INFOCOM*. IEEE. 2012, pp. 2210–2218.

[49] Sen S et al. "Avoiding multipath to revive inbuilding WiFi localization". In: *Proceeding of the 11th annual international conference on Mobile systems, applications, and services*. 2013, pp. 249–262.

[50] Rappaport TS. *Wireless communications: principles and practice*. Vol. 2. prentice hall PTR New Jersey, 1996.

[51] *3D Electromagnetic Field Simulator for RF and Wireless Design*. `https://www.ansys.com/products/electronics/ansys-hfss`. Accessed: 2022-06-01.

[52] Waghmare C and Kothari A. "Spanner shaped ultra wideband patch antenna". In: *2014 Students Conference on Engineering and Systems*. IEEE. 2014, pp. 1–4.

[53] Mohammadirad M, Komjani N, and Yazdi M. "Design and implementation of a new UWB microstrip antenna". In: *2010 14th International Symposium on Antenna Technology and Applied Electromagnetics & the American Electromagnetics Conference*. IEEE. 2010, pp. 1–4.

[54] Liu L, Cheung SW, and Yuk TI. "Bandwidth improvements using ground slots for compact UWB microstrip-fed antennas". In: *Progress in Electromagnetics Research Symposium*. Electromagnetics Academy. The Journal's web site is located at http://www . . . 2011.

[55] Weng LH et al. "An overview on defected ground structure". In: *Progress In Electromagnetics Research B* 7 (2008), pp. 173–189.

[56] *AWR Design Environment.* `https://www.cadence.com/en_US/home/tools/system-analysis/rf-microwave-design/awr-design-environment-platform.html`. Accessed: 2022-08-24.

[57] *TGbf Functional Requirements Document (FRD).* `https://mentor.ieee.org/802.11/dcn/20/11-20-1813-00-00bf-ieee-802-11bf-functional-requirements-document.docx`. Accessed: 2022-06-02.

[58] David López-Pérez et al. "IEEE 802.11 be extremely high throughput: The next generation of Wi-Fi technology beyond 802.11 ax". In: *IEEE Communications Magazine* 57.9 (2019), pp. 113–119.

[59] Coombs Jr CF. *Printed circuits handbook.* McGraw-Hill Education, 2008.

[60] *LPKF ProtoMat®.* `https://www.lpkfusa.com/pcb/`. Accessed: 2022-06-12.

[61] *Keysight 2-Port and 4-Port PNA Network Analyzer.* `https://www.keysight.com/us/en/assets/9018-04179/technical-specifications/9018-04179.pdf`. Accessed: 2022-06-13.

[62] *DAMS Antenna Measurement Systems Guide.* `https://www.diamondeng.net/PDF/brochurelr.pdf`. Accessed: 2022-06-13.

[63] *Mini-Circuits Coaxial Wideband Amplifier ZVA-203GX+.* `https://www.minicircuits.com/pdfs/ZVA-203GX+.pdf`. Accessed: 2022-06-14.

[64] *Lecture 3: HFSS ports.* `https://www.ansys.com/training-center/course-catalog/electromagnetics/ansys-hfss-3d-components-boundary-conditions-ports-and-mesh`. Accessed: 2022-06-20.

[65] Nassar IT and Weller TM. "An electrically small meandered line antenna with truncated ground plane". In: *2011 IEEE Radio and Wireless Symposium.* IEEE. 2011, pp. 94–97.

[66] *Small Antenna-Radiation Resistance.* `https://www.w8ji.com/radiation_resistance.htm`. Accessed: 2022-06-19.